Chapter 2
Nanostructured Lead Sulfide PbS

Lead sulfide is a representative of the abundant family of semiconducting chalcogenides. Lead sulfide PbS is a single compound existing in the Pb–S system (Fig. 2.1). Metallic lead Pb has the face-centered cubic (space group $Fm\bar{3}m$) structure of $A1$ type with a lattice constant 0.4948 nm. Lead sulfide contains $\sim$50 at.% S, has the melting temperature 1391 K, and possesses narrow region of homogeneity [1]. Indeed, the detailed analysis of phase diagram of the Pb–S system near $\sim$50 at.% S (Fig. 2.2) shows that the maximum melting temperature of lead sulfide corresponds to nonstoichiometric composition $PbS_{0.9998}$ [2]. It follows from data [2] that lead sulfide has very narrow homogeneity region from 49.9905 to 50.003 at.% S at a temperature of 1300 K.

In normal conditions, bulk and coarse-grained PbS is a direct narrow-gap semiconductor with a $B1$ cubic crystal structure. At the temperature 300 K, the band gap of PbS single crystals and polycrystalline coarse-grained PbS films is equal to 0.41–0.42 eV [3–5]. Lead sulfide PbS is one of the most demanded narrow-gap semiconductors. It is used in a number of devices such as photodetectors operating in a broad [from infrared (IR) to ultraviolet (UV)] wavelength range, high efficiency solar cells, thermoelectric transducers and optical switches. Transition from coarse-grained to nanostructured PbS has considerably extended the scope of its application, especially in those cases where the particle size is comparable with (or less than) the lead sulfide exciton radius, which is 18 nm.

The latest achievements in the synthesis of colloidal nanocrystals of lead chalcogenides (PbS and PbSe) and nanocrystals for solar cells can be regarded as a claim for the design of photoelectric and infrared devices based on nanostructured lead chalcogenides. The most efficient process resulting in the formation of nanocrystals with well controllable size and low size dispersion is the chemical synthesis of colloid chalcogenide solutions.

Large Bohr exciton radius (18 nm) and small masses for electrons and holes promote effective charge delocalization in PbS thin films and therefore high charge

S.I. Sadovnikov et al., *Nanostructured Lead, Cadmium, and Silver Sulfides*,
Springer Series in Materials Science 256, DOI 10.1007/978-3-319-56387-9_2

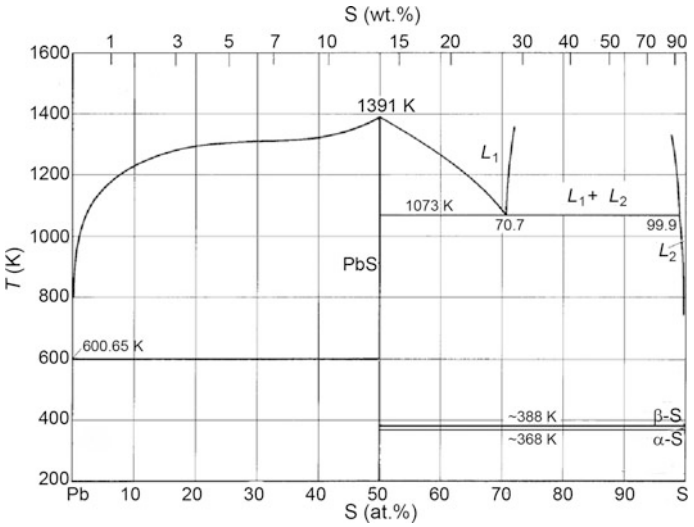

Fig. 2.1 Phase diagram of the Pb–S system [1]

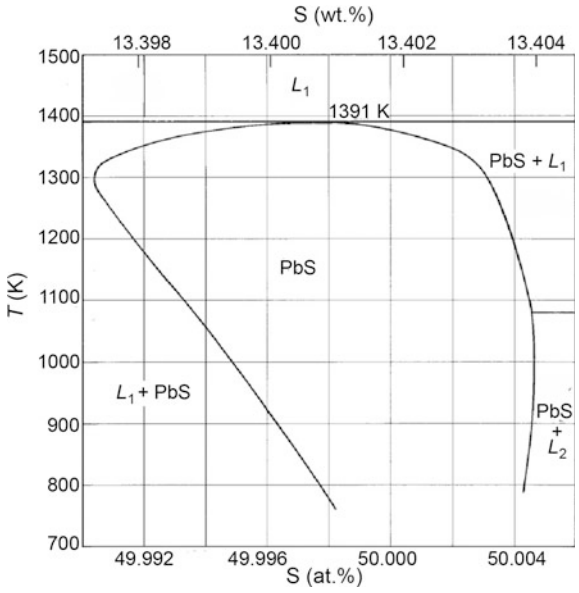

Fig. 2.2 Phase diagram of the Pb–S system near 50 at.% S [2]

carrier mobilities can be anticipated. The formation of multiple electron–hole pairs per absorbed photon has the potential to significantly improve the power conversion efficiencies in photovoltaic devices based on nanostructured lead sulfide.

Lead, silver, cadmium and zinc sulfides are of most interest among chalcogenides. Out of these nanostructured sulfides, lead sulfide is especially demanded owing to the extensive application.

It is shown in Sect. 1.1 that such concept as the "nanostructured material" covers a broad range of objects from colloidal solutions and isolated nanoparticles to heteronanostructures of different dimensionality, nanofilms and nanopowders. In line with this, we discuss in this chapter the preparation methods, structures and properties of lead sulfide colloidal solutions, single nanoparticles, nanofilms and nanopowders. Until recently, there were no generalizing works on nanostructured lead sulfide in the scientific literature. Mention only may be made of a small chapter in the monograph [6] devoted to chemical deposition of PbS films. The first fundamental review of structure and properties of nanostructured lead sulfide [7] was published in 2016.

The principal methods of synthesis described in this chapter are general and applicable to the synthesis of any chalcogenide, and the key properties of nanostructured lead sulfide are also typical of other chalcogenides.

2.1 Methods for the Preparation of Nanostructured Lead Sulfide: From Colloidal Solutions to Thin Films

The most important factors that have to be taken into account in the synthesis of nanoparticles are the following:

(1) non-equilibrium nature of systems; virtually all nanosystems are thermodynamically unstable; they are prepared under conditions far from equilibrium; this provides active nucleation and, owing to the enormous number of nuclei which accumulate the major part of material, the possible growth of the formed nanoparticles can be appreciably restricted;
(2) high chemical homogeneity; the nanomaterial homogeneity is achieved if no component separation, either within a single nanoparticle or between the particles, takes place during the synthesis;
(3) monodispersity; the properties of nanoparticles strongly depend on the particle size; therefore, for the manufacture of materials with good performance characteristics, it is necessary to synthesize particles with rather narrow size distribution.

The preparation processes of nanostructured materials can be classified into two groups according to the way the nanostructure is formed [8], namely, the bottom-up approach implies the assembly of nanoparticles from atoms and molecules, i.e, the initial species are enlarged to give nanoparticles; the top-down processes are based on disintegration of larger particles or powders to the nanosize.

2.1.1 Colloidal Solutions of Lead Sulfide Nanoparticles

The usual method for the preparation of colloidal solutions of sulfides consists in the chemical reaction between solution components (water-soluble metal salt, sulfidizer and complexing agent) and termination of the reaction at a definite time point. For certain conditions of synthesis, the dispersion system thus formed can be preserved in the liquid state, i.e, as a colloidal solution. By transferring the liquid colloidal dispersion system to the solid dispersed state, it is possible to precipitate nanosized (or larger) particles from the solution. In the general case, the preparation of a chalcogenide colloidal solution can be conventionally divided into four stages [9]: (1) formation of an equilibrium homogeneous complexing agent – water system; (2) formation and dissociation of the metal complex $[ML_i]^{n+ik}$ (L is ligand, n is the oxidation state of metal M, i is the number of ligands, k is the ligand charge); (3) hydrolysis of the chalcogenizing agent; and (4) formation of metal chalcogenide. At the final stage, the dispersed chalcogenide solid phase precipitates or is deposited on the substrate as a film.

A colloidal solution should be considered as stable if during a long period of storage (more than 100 h), no nanopowder precipitation occurs and the size of nanoparticles present in the solution remains invariable or varies within the error of measurements.

In the vast majority of publications devoted to the synthesis of chalcogenide nanoparticles by chemical bath deposition, the issue of stability of colloidal solutions is not addressed, although only stable colloidal solutions can serve as sources of the smallest-size nanoparticles. An exception is a paper of Deng et al. [10] who consider solubilization, that is, transformation of oil-soluble PbS quantum dots into water- soluble quantum dots, and mention the stability of aqueous colloidal solutions.

Currently, most of colloidal solutions of lead sulfide are synthesized using organometallic compounds [11–14]. Soluble metal complexes are sulfided with hydrogen sulfide gas or hydrosulfuric acid H_2S, sodium thiosulfate $Na_2S_2O_3$, sodium sulfide Na_2S, amide (thioacetamide) $CH_3C(S)NH_2$ or diamide N_2H_4CS of thiocarbonic acid and their derivatives – thiocarbazide $(NH_2)_2(NH)_2CS$, acetylthiocarbamide $C_3H_6N_2OS$ and so on. In some cases (usually in the case of solvothermal synthesis), elemental sulfur is used for sulfiding [15]. The particle size is controlled by changing the number of sulfide phase nuclei as they are formed. The use of toxic organometallic lead compounds and organic ligands (thioglycerol, heptane, trioctylphosphine) to prevent agglomeration and growth of PbS particles results in toxicity of the obtained colloidal solutions and restricts the scope of their applicability by ruling out the biological and medical applications.

From the standpoint of a potential biomedical application, hydrochemical synthesis using aqueous solutions of reactants is more acceptable [16–19]. However, in most cases, stability of aqueous colloidal solutions, including lead sulfide solutions, is moderate, ranging from several minutes to 1–2 h.

The conditions of synthesis of stable non-toxic aqueous PbS colloidal solutions were elucidated by Sadovnikov et al. [19]. Lead acetate $Pb(CH_3COO)_2 \equiv Pb(AcO)_2$ and sodium sulfide Na_2S served as the sources of Pb^{2+} and S^{2-} ions, while disodium ethylenediaminetetraacetate Na_2H_2-EDTA$\equiv C_{10}H_{18}N_2Na_2O_{10}$ (Trilon B) or sodium cit-rate $Na_3C_6H_5O_7 \equiv Na_3Cit$ functioned as the complexing agents. The initial solutions of $Pb(AcO)_2$, Na_2S, Na_3Cit, and Trilon B had the same concentration 50 mmol l^{-1}. The initial concentrations of $Pb(OAc)_2$, Na_2S, sodium citrate and Trilon B in the reaction mixtures varied from 0.25 to 25 mmol l^{-1}. The molar concentration ratio for the reactants in the mixtures was stoichiometric: $[Pb^{2+}]:[S^{2-}]:[TrB, Cit^{3-}] = 1:1:1$, where $[Pb^{2+}]$, $[S^{2-}]$, [TrB], and $[Cit^{3-}]$ are the concentrations of lead ions, sulfide ions, and the complexing agents, respectively. The colloidal solutions were prepared at room temperature and pH from 4.75 to 6.25. Synthesis comprised the following sequence of steps: to lead acetate was added with constant stirring a complexing agent. Next, the volume of the mixture was brought to 100 mL, and the resultant solution was mixed with 100 mL of a Na_2S solution. According to Sadovnikov and Gusev [20], the order of addition of the complexing agent to lead acetate or sodium sulfide solution does not affect the solution stability or nanoparticle size but can give rise to impurity phases. Indeed, in an aqueous solution containing hydrated Pb^{2+}, AcO^- and S^{2-} ions, two dozens of products can appear upon hydrolysis, apart from the colloidal PbS particles [21].

Synthesis conditions of all colloidal solutions and particle size are given in Table 2.1.

The colloidal solution of lead sulfide nanoparticles is formed upon the following reaction:

$$Pb(OAc)_2 + Na_2S \xrightarrow{Na_3Cit \text{ or } Na_2H_2 - EDTA} PbS + 2NaOAc. \quad (2.1)$$

Table 2.1 Concentration of reactants in the reaction mixtures, stability time t of colloidal solutions, and the size D_{DLS} of PbS nanoparticles [19]

Concentration of reactants in the reaction mixtures (mmol l^{-1})				t (day)	D_{DLS} (nm)
$Pb(CH_3COO)_2$	Na_2S	$Na_3C_6H_5O_7$	Trilon B		
25	25	0	0	[a]	7–20[b]
0.8	0.8	0	0	[a]	5[b]
1.25	1.25	0	1.25	4	120
0.8	0.8	0	0.8	4	15
0.5	0.5	0	0.5	4	18
0.25	0.25	0	0.25	>6	15
1.25	1.25	1.25	0	30	13
0.8	0.8	0.8	0	30	13
0.5	0.5	0.5	0	5	11
0.25	0.25	0.25	0	5	10

[a]Stability of these colloidal solutions less than 1 h
[b]Particle size in deposited powders was determined by XRD method

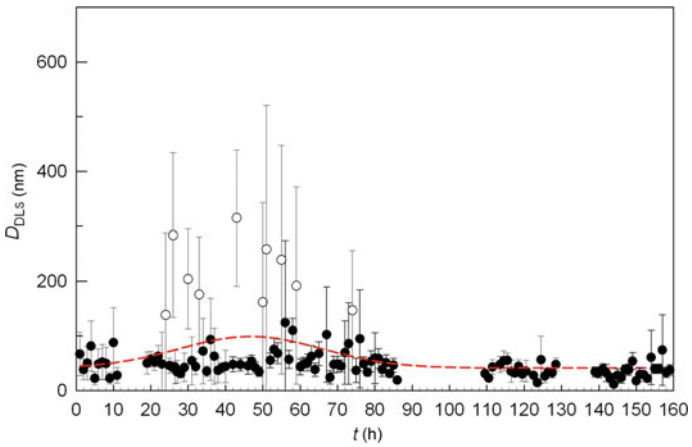

Fig. 2.3 Ranges of $D_{DLS\ (nm)}$ values for PbS agglomerates (1) and nanoparticles (2) in a colloid solution as functions of solution storage time at room temperature [19]. The enveloping curve shows the particle size distribution depending on the storage time

In order to estimate the effect of complexing agents on the stability of colloidal solutions, similar solutions were prepared without addition of sodium citrate or Trilon B. In particular, PbS nanoparticles precipitated from reaction mixtures with equal concentrations $[Pb(AcO)_2]=[Na_2S]$, either 0.8 or 25 mmol l^{-1}, within 10 and 60 min after the synthesis, respectively. No stable colloidal solution formed.

The stability of colloidal solutions was evaluated in study [19] by considering the change in the colloidal nanoparticle size (hydrodynamic diameter D_{DLS}) depending on the time (t) of solution storage. The D_{DLS} value of PbS nanoparticles directly in the colloidal solution was determined by dynamic light scattering.

When Trilon B was added to the reaction mixture, stability of the colloidal solutions increased to 4 days, and by using sodium citrate, it was possible to prepare colloidal solutions that were stable for more than 30 days (they did not change their properties during this period) (Fig. 2.3). The PbS particle size in colloidal solutions depends on the initial concentrations of lead acetate and sodium sulfide and on the type of complexing agent. By varying these parameters, it is possible to obtain stable colloidal solutions with a specified particle size ranging from 10 to 20 nm [19].

This process for preparation of colloidal solutions of PbS is protected by the patent [22].

2.1.2 Analysis of the Formation Conditions of Lead Sulfide in Aqueous Solutions

It was noted above that, along with colloidal PbS particles, numerous products of hydrolysis are formed in an aqueous solution containing hydrated Pb^{2+}, AcO^- and

S^{2-} ions. The important role of metal hydroxide during chemical deposition was discussed in numerous publications (see, for example [15, 23, 24]. For example, upon chemical deposition from aqueous solutions of thiourea N_2H_4CS, metal sulfides are formed as thin films [15, 23, 25, 26] on non-metallic surfaces only in the thermodynamic stability region of metal hydroxide in the solution (hydroxide region). The microstructure of chemically deposited sulfide films depends on the pH value and on the presence of metal hydroxide in the reaction mixture [27]. Metal hydroxide is significant for the assembly of core-shell type sulfide heteronanostructures [28]. Therefore, calculation of the concentration region of formation of metal hydroxide, which makes it possible to predict the possibility for its appearance in the solution before the sulfide synthesis, is an important task faced by a researcher who performs chemical deposition from aqueous solutions. This calculation is based on comparison of the ionic product with the solubility product of metal hydroxide, $K_{sp} = [M^{m+}]\cdot[OH^-]^m$, where $[M^{m+}]$ and $[OH^-]$ are the equilibrium concentrations of free metal ions and hydroxide ions, respectively.

The data on the conditions of formation of lead hydroxide in the Pb^{2+}–H_2O system taking account of the existence of multinuclear hydroxo complexes are scarce. Therefore, a calculation method was proposed in studies [29, 30] and a distribution diagram for complexes in the Pb^{2+}–H_2O system taking account of all polynuclear hydroxo complexes for which the formation constants are known was presented [31].

In aqueous solution the metal ions together with an insoluble hydroxide form soluble hydroxo complexes, the compounds in which hydroxy ions are the substituting ligands. Many metals (e.g., lead, iron, nickel, bismuth, tin, beryllium, etc.) form with the OH^- ions not only mononuclear hydroxocomplexes $M(OH)_n$, but also polynuclear neutral or charged hydroxo complexes $M_p(OH)_n$ ($n \geq 1, p \geq 2$, both are integers). The studies [24, 32–34] on the determination of conditions for the formation of the hydroxide in the process of chemical deposition of sulfides and selenides take into account the mononuclear hydroxo complexes of metals, or only some of the polynuclear complexes. In the polynuclear complexes the number of ligands associated with the metal atom depends both on the concentrations of ligand and metal. For this reason, the equations describing the equilibrium conditions are not linear with respect to the analytical concentration of the metal ions M^{m+} that greatly complicates or even makes it impossible to solve the equations analytically. Apparently, this is a reason for taking into account only mononuclear hydroxo complexes in the calculations of the concentration regions of formation [24, 32, 34], although in recent years the software have appeared for the calculations and simulation of ionic equilibrium in aqueous solutions. Another reason for considering only the mononuclear hydroxo complexes lies in the fact that in the systems with ligands that form more stable complexes than hydroxo complexes, the impact of polynuclear hydroxo complexes on the equilibrium is rather weak. However, the exclusion from the calculation of polynuclear hydroxo complexes leads, as shown below, to a significant shift of the boundaries of the concentration regions.

There is only limited published information on the formation of lead hydroxide in the system of Pb^{2+}–H_2O which accounts for the existence of polynuclear

hydroxo complexes. The data are controversial due to discrepancy in the numerical values of the constants of formation of polynuclear complexes.

The equilibrium state in a saturated solution of lead hydroxide is described as

$$K_{sp} = \left[Pb^{2+}\right] \cdot [OH^-]^2, \tag{2.2}$$

where $K_{sp} = (1.0–1.2) \times 10^{-15}$ [35, 36] is the solubility product of lead hydroxide at the normal conditions. In accordance with (2.2) the equilibrium concentration $[Pb^{2+}]$ of free ions of lead is

$$\left[Pb^{2+}\right] = K_{sp}/[OH^-]^2 \equiv K_{sp}[H^+]^2/K_w^2, \tag{2.3}$$

where $K_w = [H^+] \cdot [OH^-] = 10^{-14}$ is the ion product of water at 298 K.

Many studies of hydrolysis suggest that the distribution of lead(II) between its individual hydroxo complexes depends on three most important variables: the concentration of the lead salts, the medium pH, and the temperature. For example, according to [37, 38], in very dilute solutions with a total concentration of Pb(II) which equals 1×10^{-9} M, the hydrolysis is detected at pH > 4, and increase in pH to 9 leads to the formation of $PbOH^+$ only. With further increase in pH the $PbOH^+$ fraction in solution decreases, while the accumulation occurs of di- and trihydroxo complexes $Pb(OH)_2$ and $Pb(OH)_3^-$. At pH up to ~10.5 both complexes are formed in comparable amounts, and in more alkaline environment the fraction of trihydroxo complex rapidly increases, so at pH > 12 it becomes the only form of the Pb(II) existence. With the increase in the total concentration of lead, the polynuclear hydroxo complexes form in solution [31, 37, 38]. At the Pb(II) concentration equal to 5×10^{-5} M the solution contains complexes $Pb_3(OH)_4^{2+}$, and at a higher concentration, of 1×10^{-3} M, the solution contains the complexes $Pb_4(OH)_4^{4+}$ and $Pb_6(OH)_8^{4+}$. When the concentration of Pb(II) is above 0.5 M the hydroxo complex $Pb_2(OH)^{3+}$ appears [37]. The complexes $Pb_3(OH)_3^{3+}$ [37] and $Pb_3(OH)_5^{+}$ [38, 39] were detected also, but, according to [40], the experimental evidence of their existence is not reliable enough.

Let us calculate the ionic composition of the "Pb^{2+}–Cit^{3-}–OH^-–H_2O" system taking into account not only mononuclear, but also the polynuclear Pb(II) hydroxo complexes in aqueous solution. In describing the equilibria in solutions of complex lead ions we use the equilibrium constant β_{ij} recommended in [31, 41, 42] (Table 2.2). Note that in alkaline solution the ion OH^- competes with such a stable in an alkaline environment ligand as citrate ion $C_6H_5O_7^{3-}$ (Cit^{3-}) forming enough stable complexes with the lead ions [42].

For the citrate system "Pb^{2+}–Cit^{3-}–OH^-–H_2O" the condition of material equilibrium in all eleven soluble forms of lead Pb^{2+}, $Pb(OH)^+$, $Pb(OH)_2$, $Pb(OH)_3^-$, $Pb_3(OH)_4^{2+}$, $Pb_4(OH)_4^{4+}$, $Pb_6(OH)_8^{4+}$, Pb_2OH^{3+}, $PbCit^-$, $Pb(Cit)_2^{4-}$, $Pb(OH)Cit^{2-}$ can be written as

Table 2.2 The conditions of equilibrium and equilibrium constants in the systems "Pb^{2+}–OH^-–H_2O" [31, 41] and "Pb^{2+}–OH^-–Cit^{3-}–H_2O" [41, 42]

Equilibrium conditions	Equilibrium constant at 298.15 K, 10^5 Pa, and ionic strength $I_m = 0$ mol·kg^{-1}
$Pb^{2+} + H_2O \leftrightarrow Pb(OH)^+ + H^+$	$\beta_{11} = [Pb(OH)^+][H^+]\ /[Pb^{2+}] = 3.47 \times 10^{-8}$
$Pb^{2+} + 2H_2O \leftrightarrow Pb(OH)_2 + 2H^+$	$\beta_{12} = [Pb(OH)_2][H^+]^2/[Pb^{2+}] = 1.15 \times 10^{-17}$
$Pb^{2+} + 3H_2O \leftrightarrow Pb(OH)_3^- + 3H^+$	$\beta_{13} = [Pb(OH)_3^-][H^+]^3/[Pb^{2+}] = 9.33 \times 10^{-29}$
$3Pb^{2+} + 4H_2O \leftrightarrow Pb_3(OH)_4^{2+} + 4H^+$	$\beta_{34} = [Pb_3(OH)_4^{2+}][H^+]^4/[Pb^{2+}]^3 = 9.77 \times 10^{-24}$
$4Pb^{2+} + 4H_2O \leftrightarrow Pb_4(OH)_4^{4+} + 4H^+$	$\beta_{44} = [Pb_4(OH)_4^{4+}][H^+]^4/[Pb^{2+}]^4 = 2.69 \times 10^{-21}$
$6Pb^{2+} + 8H_2O \leftrightarrow Pb_6(OH)_8^{4+} + 8H^+$	$\beta_{68} = [Pb_6(OH)_8^{4+}][H^+]^8/[Pb^{2+}]^6 = 1.29 \times 10^{-43}$
$2Pb^{2+} + H_2O \leftrightarrow Pb_2OH^{3+} + H^+$	$\beta_{21} = [Pb_2OH^{3+}][H^+]/[Pb^{2+}]^2 = 5.25 \times 10^{-8}$
$Pb^{2+} + Cit^{3-} \leftrightarrow PbCit^-$	$\beta_1 = [PbCit^-]/[Pb^{2+}][Cit^{3-}] = 3.07 \times 10^6$
$Pb^{2+} + 2Cit^{3-} \leftrightarrow Pb(Cit)_2^{4-}$	$\beta_{12cit} = [Pb(Cit)_2^{4-}]/[Pb^{2+}][Cit^{3-}]^2 = 3.03 \times 10^8$
$Pb^{2+} + OH^- + Cit^{3-} \leftrightarrow Pb(OH)Cit^{2-}$	$\beta_1' = [Pb(OH)Cit^{2-}]/[Pb^{2+}][OH^-][Cit^{3-}] = 5.25 \times 10^{13}$

$$C_{\mathrm{Pb},\Sigma}^{\mathrm{cit}} = [\mathrm{Pb}^{2+}]\left\{1 + \frac{[\mathrm{Pb(OH)}^{+}]}{[\mathrm{Pb}^{2+}]} + \frac{[\mathrm{Pb(OH)_2}]}{[\mathrm{Pb}^{2+}]} + \frac{[\mathrm{Pb(OH)_3^-}]}{[\mathrm{Pb}^{2+}]} + \frac{3[\mathrm{Pb_3(OH)_4^{2+}}]}{[\mathrm{Pb}^{2+}]} + \frac{4[\mathrm{Pb_4(OH)_4^{4+}}]}{[\mathrm{Pb}^{2+}]} + \frac{6[\mathrm{Pb_6(OH)_8^{4+}}]}{[\mathrm{Pb}^{2+}]} + \frac{2[\mathrm{Pb_2OH^{3+}}]}{[\mathrm{Pb}^{2+}]} + \frac{[\mathrm{PbCit^-}]}{[\mathrm{Pb}^{2+}]} + \frac{[\mathrm{Pb(Cit)_2^{4-}}]}{[\mathrm{Pb}^{2+}]} + \frac{[\mathrm{Pb(OH)Cit^{2-}}]}{[\mathrm{Pb}^{2+}]}\right\} \tag{2.4}$$

Let us represent the ratio of the concentrations of complexes to the concentration $[Pb^{2+}]$ in (2.4) through the equilibrium constant (see Table 2.2) and transform it into a form more convenient for further analysis:

$$C_{\mathrm{Pb},\Sigma}^{\mathrm{cit}} = [\mathrm{Pb}^{2+}]\left\{1 + \frac{\beta_{11}}{[\mathrm{H}^+]} + \frac{\beta_{12}}{[\mathrm{H}^+]^2} + \frac{\beta_{13}}{[\mathrm{H}^+]^3} + \frac{3\beta_{34}[\mathrm{Pb}^{2+}]^2}{[\mathrm{H}^+]^4} + \frac{4\beta_{44}[\mathrm{Pb}^{2+}]^3}{[\mathrm{H}^+]^4} + \frac{6\beta_{68}[\mathrm{Pb}^{2+}]^5}{[\mathrm{H}^+]^8} + \frac{2\beta_{21}[\mathrm{Pb}^{2+}]}{[\mathrm{H}^+]} + \beta_1[\mathrm{Cit}^{3-}] + \beta_{1,2}[\mathrm{Cit}^{3-}]^2 + \beta_1^* \frac{K_w[\mathrm{Cit}^{3-}]}{[\mathrm{H}^+]}\right\} \tag{2.5}$$

If the citrate ion concentration $[Cit^{3-}] = 0$, then (2.5) is converted to a particular form, which describes the condition of the material balance of the lead soluble forms in a citrate-free "Pb^{2+}–OH^-–H_2O"system:

$$C_{\mathrm{Pb},\Sigma} = [\mathrm{Pb}^{2+}]\left\{1 + \frac{\beta_{11}}{[\mathrm{H}^+]} + \frac{\beta_{12}}{[\mathrm{H}^+]^2} + \frac{\beta_{13}}{[\mathrm{H}^+]^3} + \frac{3\beta_{34}[\mathrm{Pb}^{2+}]^2}{[\mathrm{H}^+]^4} + \frac{4\beta_{44}[\mathrm{Pb}^{2+}]^3}{[\mathrm{H}^+]^4} + \frac{6\beta_{68}[\mathrm{Pb}^{2+}]^5}{[\mathrm{H}^+]^8} + \frac{2\beta_{21}[\mathrm{Pb}^{2+}]}{[\mathrm{H}^+]}\right\} \tag{2.6}$$

In accordance with (2.6) the fractional concentration of free Pb^{2+} ions in the "Pb^{2+}–OH^-–H_2O" system is

$$\alpha_{\mathrm{Pb}^{2+}} = \frac{[\mathrm{Pb}^{2+}]}{C_{\mathrm{Pb},\Sigma}} = \left\{1 + \frac{\beta_{11}}{[\mathrm{H}^+]} + \frac{\beta_{12}}{[\mathrm{H}^+]^2} + \frac{\beta_{13}}{[\mathrm{H}^+]^3} + \frac{3\beta_{34}[\mathrm{Pb}^{2+}]^2}{[\mathrm{H}^+]^4} + \frac{4\beta_{44}[\mathrm{Pb}^{2+}]^3}{[\mathrm{H}^+]^4} + \frac{6\beta_{68}[\mathrm{Pb}^{2+}]^5}{[\mathrm{H}^+]^8} + \frac{2\beta_{21}[\mathrm{Pb}^{2+}]}{[\mathrm{H}^+]}\right\}^{-1} \tag{2.7}$$

Using (2.7), the fractional concentrations $\alpha_i = C_i / C_{\mathrm{Pb},\Sigma}$ of all Pb(II) hydroxo complexes in the "Pb^{2+}–OH^-–H_2O" system can be written as the functions of $\alpha_{\mathrm{Pb}^{2+}}$ and the concentrations of H^+ and Pb^{2+} ions:

$$\alpha_{Pb(OH)^+} = \beta_{11}\alpha_{Pb^{2+}}/[H^+], \tag{2.8a}$$

$$\alpha_{Pb(OH)_2} = \beta_{12}\alpha_{Pb^{2+}}/[H^+]^2, \tag{2.8b}$$

$$\alpha_{Pb(OH)_3^-} = \beta_{13}\alpha_{Pb^{2+}}/[H^+]^3, \tag{2.8c}$$

$$\alpha_{Pb_3(OH)_4^{2+}} = 3\beta_{34}\alpha_{Pb^{2+}}[Pb^{2+}]^2/[H^+]^4, \tag{2.8d}$$

$$\alpha_{Pb_4(OH)_4^{4+}} = 4\beta_{44}\alpha_{Pb^{2+}}[Pb^{2+}]^3/[H^+]^4, \tag{2.8e}$$

$$\alpha_{Pb_6(OH)_8^{4+}} = 6\beta_{68}\alpha_{Pb^{2+}}[Pb^{2+}]^5/[H^+]^8, \tag{2.8f}$$

$$\alpha_{Pb_2(OH)^{3+}} = 2\beta_{21}\alpha_{Pb^{2+}}[Pb^{2+}]/[H^+] \tag{2.8g}$$

Equations (2.6) and (2.7) are of 6th degree with respect to the concentration of Pb^{2+} ions and do not have analytical solutions of a general form. Still, the problem of hydrolysis of the Pb^{2+} ion described by a set of (2.7), (2.8a, b, c, d, e, f, g) can be solved numerically.

Indeed, at a known total concentration $C_{Pb,\Sigma}$ of the soluble forms of lead the dependence of $[Pb^{2+}]$ on the concentration of protons H^+ (that is, the solution pH) can be found by means of self-consistent numerical solution of (2.7) by the successive approximation procedure. In other words, at a given concentrations $C_{Pb,\Sigma}$ we can calculate the dependence of the fraction of uncomplexed lead ions on the pH. For this purpose, using a software package SigmaPlot 2001 for Windows [43] a special program was written. With the numerical relationship $[Pb^{2+}] = f([H^+])|_{C_{Pb,\Sigma}=const}$ found from (2.7) it is easy to obtain fractional concentrations α_i of free ions and all the Pb(II) hydroxo complexes at different pH values.

Figure 2.4 shows the fractional concentrations of free ions and the Pb(II) hydroxo complexes in solution for the system "Pb^{2+}–OH^-–H_2O" depending on the pH value, calculated with the (2.7), (2.8a, b, c, d, e, f, g) for three values of $C_{Pb,\Sigma}$ 0.001, 0.01, and 0.1 M. As seen, the hydrolysis of lead ions begins at pH $\geq$ 6. The increase in the analytical concentration of lead ion shifts the Pb^{2+} hydrolysis in the region of lower pH values (Fig. 2.4a). When $C_{Pb,\Sigma}$ = 0.001 M, at pH = 8–10 lead exists mainly in the form of complex ions, $Pb_3(OH)_4^{2+}$ and $Pb_6(OH)_8^{4+}$, at pH $\geq$ 11 sharply increased the fraction of $Pb(OH)_2$ and $Pb(OH)_3^-$ (Fig. 2.4c, d). When $C_{Pb,\Sigma}$ = 0.1 M, at pH from 7 to 12 lead forms in solution the ion $Pb_6(OH)_8^{4+}$ (Fig. 2.4h). Thus, an increase in $C_{Pb,\Sigma}$ expands the pH range of existence of complexes $Pb_3(OH)_4^{2+}$ and $Pb_6(OH)_8^{4+}$, and the fraction of the complex $Pb_6(OH)_8^{4+}$ in solution increases. The only polynuclear complex, the relative content of which is negligible, is Pb_2OH^{3+} (this is consistent with the results [33]). It exists in a narrow range 3 < pH < 8 (Fig. 2.4g). At pH $\geq$ 12 for all concentrations used in the calculations of $C_{Pb,\Sigma}$ the main form of existence of lead in

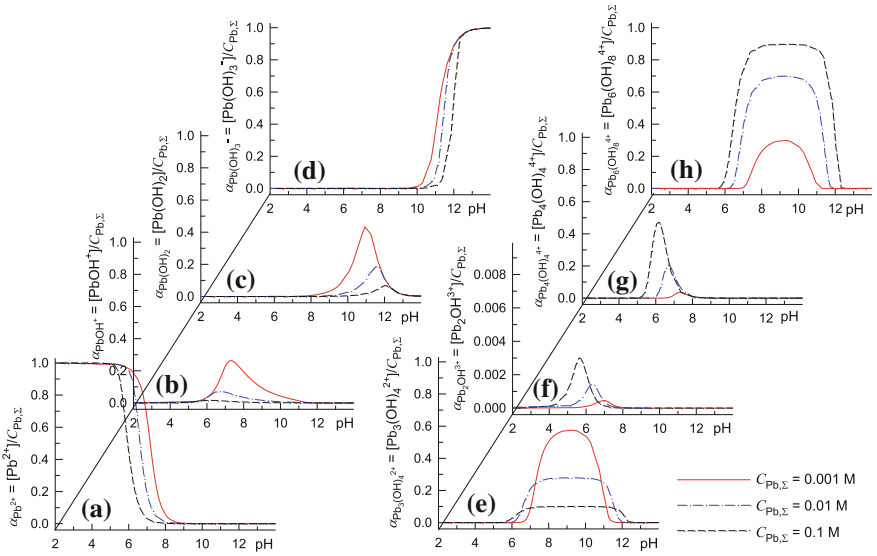

Fig. 2.4 Dependence of partial concentration α_i of **a** the free ions Pb^{2+}, mononuclear **b** $Pb(OH)^+$, **c** $Pb(OH)_2$, **d** $Pb(OH)_3^-$, and polynuclear **e** $Pb_3(OH)_4^{2+}$, **f** $Pb_2(OH)^{3+}$, **g** $Pb_4(OH)_4^{4+}$, and **h** $Pb_6(OH)_8^{4+}$ hydroxo complexes of lead on the pH in the solution of the "Pb^{2+}–OH^-–H_2O" system at T = 298.15 K for three values of the total analytical concentration of lead in solution $C_{Pb,\Sigma}$: 0.001, 0.01 and 0.1 M

solution is a mononuclear complex $Pb(OH)_3^-$ (Fig. 2.4d). Thus, for the precise analysis of ionic equilibria in aqueous solutions of lead salts the polynuclear hydroxo complexes should be taken into account, which are the main form of existence of lead in solution in the pH range from 7 to 12.

Note that all dependences (2.7) and (2.8a, b, c, d, e, f, g) of the fractional concentrations α_i are power functions of $[H^+]$ (or pH), that is, smooth functions with no break point or discontinuity. However, in [31] (see Fig. 2.4a) the break points were observed in the calculated dependences of the fractional concentrations of $Pb_3(OH)_4^{2+}$ and $Pb_6(OH)_8^{4+}$ on the pH in the "Pb^{2+}–OH^-" system with $C_{Pb,\Sigma}$ = 0.00048 M at pH ~ 9.25. This is due to the fact that in work [31] the fractional concentrations were calculated taking into account the abrupt change in the total concentration of lead in solution due to precipitation of lead oxide at pH > 9.3.

Let us now determine the stability region of lead hydroxide $Pb(OH)_2$ in the citrate-free system "Pb^{2+}–OH^-–H_2O". The conditions of formation of solid phase $Pb(OH)_2$ in water solution can be found from the following relation

$$K_{sp} < \left[Pb^{2+}\right][OH^-]^2. \tag{2.9}$$

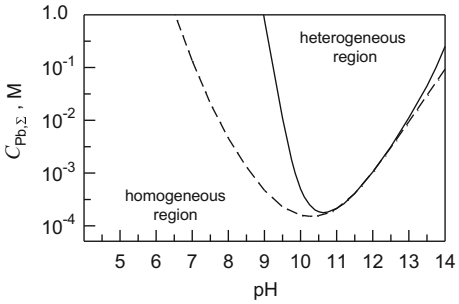

Fig. 2.5 Effect of accounting for the polynuclear hydroxo complexes of lead on the position of the boundary of the lead hydroxide $Pb(OH)_2$ formation in the system "Pb^{2+}–OH^-–H_2O" at the different pH values at 298.15 K: *solid line* corresponds to considering all mono- and polynuclear hydroxo complexes, dashed line corresponds to considering only the mononuclear hydroxo complexes. The total concentration of lead, $C_{Pb,\Sigma}$, in the solution is shown in a logarithmic scale

Substituting the expression (2.3) in (2.6) for the concentration $[Pb^{2+}]$, we obtain the relation, which is the equation of the boundary of the $Pb(OH)_2$ solid phase deposition

$$C_{Pb,\Sigma} = \frac{K_{sp}[H^+]^2}{K_w^2}\left\{1 + \frac{\beta_{11}}{[H^+]} + \frac{\beta_{12}}{[H^+]^2} + \frac{\beta_{13}}{[H^+]^3} + \frac{3\beta_{34}K_{sp}^2}{K_w^4} + \frac{4\beta_{44}K_{sp}^3[H^+]^2}{K_w^6} + \frac{6\beta_{68}K_{sp}^5[H^+]^2}{K_w^{10}} + \frac{2\beta_{21}K_{sp}[H^+]}{K_w^2}\right\} \quad (2.10)$$

The positions of the $Pb(OH)_2$ formation boundary in the "Pb^{2+}–HO^-–H_2O" system determined considering only mononuclear complexes or considering both mono- and polynuclear lead hydroxo complexes are shown in Fig. 2.5. The calculation is made according to (2.10).

As can be seen, the effect of polynuclear complexes on the equilibrium position of the heterogenic equilibrium "$Pb(OH)_2$ hydroxide–Pb(II) ions" is especially pronounced in the region of pH < 10.5. In the alkaline region due to amphoteric nature of lead hydroxide $Pb(OH)_2$ the deposition begins and occurs at pH $\leq$ 13, which agrees well with the reference and experimental data. Sulfide formation in the form of thin films on nonmetallic substrates by chemical deposition from aqueous solutions of thiocarbamide occurs only in the region of stability of the metal hydroxide [16, 23]. Figure 2.5 clearly shows that at accounting for all mononuclear and polynuclear hydroxo complexes the PbS films can be obtained in alkaline solutions with 9 < pH < 13, which fully agrees with the experimental data, for example, [16, 23, 25, 26]. If the polynuclear complexes are neglected, the left boundary of the region of formation of lead hydroxide is displaced to the acidic region, where the hydroxide $Pb(OH)_2$ is not really formed. Thus, the consideration of polynuclear hydroxo complexes is important not only theoretically, but also practically, for the synthesis of the films.

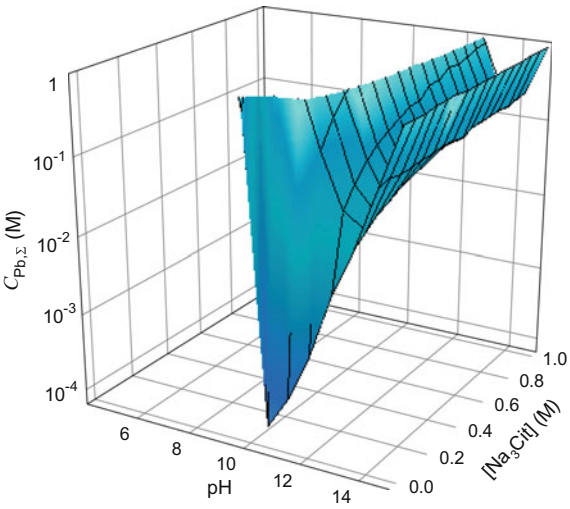

Fig. 2.6 Solubility of $Pb(OH)_2$ as a function of pH of the medium and of citrate ion concentration in the "Pb^{2+}–Cit^{3-}–OH^-–H_2O" system [30] [solubility was calculated on the (2.11)]. The three-dimensional surface is the boundary of the heterogeneous "$Pb(OH)_2$–Pb^{2+}" equilibrium. Below this surface, there is the homogeneous region in which lead exists only in the dissolved form, while above the surface lies the heterogeneous region in which $Pb(OH)_2$ is also formed and, upon the introduction of sulfide ions, PbS deposition as a film is possible. The lead concentration $C_{Pb,\Sigma}$ in the solution is presented on the logarithmic scale

We now define the stability domain of lead hydroxide $Pb(OH)_2$ in the solution, where, in addition to hydroxo complexes the citrate complexes are present. In this case, the condition of the material balance is described by (2.5), and the equation of the deposition boundary, taking into account (2.3) and (2.5), has the form

$$C_{Pb,\Sigma}^{cit} = \frac{K_{sp}[H^+]^2}{K_w^2}\left\{1 + \frac{\beta_{11}}{[H^+]} + \frac{\beta_{12}}{[H^+]^2} + \frac{\beta_{13}}{[H^+]^3} + \frac{3\beta_{34}K_{sp}^2}{K_w^4} + \frac{4\beta_{44}K_{sp}^3[H^+]^2}{K_w^6} + \frac{6\beta_{68}K_{sp}^5[H^+]^2}{K_w^{10}} + \frac{2\beta_{21}K_{sp}[H^+]}{K_w^2} + \beta_1[Cit^{3-}] + \beta_{12cit}[Cit^{3-}]^2 + \beta_1'\frac{K_w[Cit^{3-}]}{[H^+]}\right\} \quad (2.11)$$

The dependence of the solubility of lead hydroxide on the medium pH in the presence of sodium citrate, as Fig. 2.6 shows, defines the boundary conditions of existence of homogeneous and heterogeneous systems. Homogeneous region is the region of the lead existence only in the dissolved form, that is, free form and the complex ions. This region is located below the boundary surface of the heterogeneous equilibrium "$Pb(OH)_2$ hydroxide–Pb(II) ions". Above this surface is a heterogeneous region where lead hydroxide $Pb(OH)_2$ is also formed. As can be seen, the solubility of lead hydroxide decreases with increasing pH, and at [Na_3Cit] = 0 (that is, in the system "Pb^{2+}–OH^-–H_2O") reaches its minimum value

$\sim 2 \times 10^{-4}$ M at pH ≈ 10.5. In the region of pH > 10.5 lead hydroxo complexes are formed, so that the total concentration of lead in solution increases.

Increasing concentrations of citrate leads to an increase in the absolute values of the $Pb(OH)_2$ solubility and the solubility minimum is shifted to the region of higher pH values. For example, for the concentration $[Na_3Cit] = 0.05$ M the lead hydroxide solubility in the "Pb^{2+}–Cit^{3-}–OH^-–H_2O" system reaches its minimum value of 3.6×10^{-2} M при at pH ≈ 13, and for the concentration $[Na_3Cit] = 1.0$ M the minimum solubility equal to 0.146 M corresponds to pH ≈ 14 (see Fig. 2.6).

Thus, the calculation with (2.10) and (2.11) allowed us constructing a dependence of the total equilibrium concentration of lead ions in solution on the pH value and find the stability region of lead hydroxide for the system "Pb^{2+}–Cit^{3-}–OH^-–H_2O" (see Fig. 2.6) and its specific section "Pb^{2+}–OH^-–H_2O" (see Fig. 2.5). From the calculation it follows that introduction of citrate ion to the solution increases the equilibrium concentration of lead and solubility of $Pb(OH)_2$ due to the formation of citrate and hydroxo-citrate complexes.

In aqueous solution at 298 K a three-stage dissociation of citric acid occurs with the equilibria:

$$H_3Cit \leftrightarrow H^+ + H_2Cit^-, K_1 = [H^+][H_2Cit^-]/[H_3Cit] = 7.4 \times 10^{-4}, \quad (2.12a)$$

$$H_2Cit^- \leftrightarrow H^+ + HCit^{2-}, K_2 = [H^+]\left[HCit^{2-}\right][H_2Cit^-] = 1.8 \times 10^{-5}, \quad (2.12b)$$

$$HCit^{2-} \leftrightarrow H^+ + Cit^{3-}, K_3 = [H^+][Cit^{3-}][HCit^{2-}] = 4.0 \times 10^{-7}. \quad (2.12c)$$

In accordance with (2.12), the total analytical concentration of citric acid in solution can be calculated as

$$C_{H_3Cit,\Sigma} = [H_3Cit] + [H_2Cit^-] + \left[HCit^{2-}\right] + [Cit^{3-}]. \quad (2.13)$$

With (2.12) and (2.13), the fractional concentrations of molecular and ionized form of citric acid are equal

$$\alpha_{H_3Cit} = [H_3Cit]/C_{H_3Cit,\Sigma} = [H^+]^3/\{[H^+]^3 + K_1[H^+]^2 + K_1K_2[H^+] + K_1K_2K_3\}, \quad (2.14a)$$

$$\alpha_{H_2Cit^-} = [H_2Cit^-]/C_{H_3Cit,\Sigma} = K_1[H^+]^2/\{[H^+]^3 + K_1[H^+]^2 + K_1K_2[H^+] + K_1K_2K_3\}, \quad (2.14b)$$

$$\alpha_{HCit^{2-}} = [HCit^{2-}]/C_{H_3Cit,\Sigma} = K_1K_2[H^+]/\{[H^+]^3 + K_1[H^+]^2 + K_1K_2[H^+] + K_1K_2K_3\}, \quad (2.14c)$$

$$\alpha_{Cit^{3-}} = [Cit^{3-}]/C_{H_3Cit,\Sigma} = K_1K_2K_3/\{[H^+]^3 + K_1[H^+]^2 + K_1K_2[H^+] + K_1K_2K_3\}. \quad (2.14d)$$

Calculations based on (2.14) show that at pH < 2 the citric acid exists in solution in molecular form. In the pH range from 2 to 8 in addition to the molecular form the ions H_2Cit^- and $HCit^{2-}$ appear, and at pH > 8 the solution contains only Cit^{3-} ions. Hence, it is clear that Cit^{3-} ion is involved in complex formation only at pH > 8.

As a final step, we consider the ionic equilibrium in the "Pb^{2+}–Cit^{3-}–OH^-–N_2H_4CS–H_2O" system and taking into account the polynuclear hydroxo complexes refine the field of formation of lead sulfide in an aqueous solution of such sulfidizer as thiocarbamide N_2H_4CS. A spontaneous formation of metal sulfide is possible when the ion product IP_{MS} of considered sulfide MS is higher than the solubility product $K_{sp,MS}$. In the considered case the lead sulfide formation will occur if ion product $IP_{PbS} = [Pb^{2+}]\cdot[S^{2-}]$ is higher than the lead sulfide solubility product, $K_{sp,PbS} = [Pb^{2+}]_{eq}\cdot[S^{2-}]_{eq}$, that is, $IP_{PbS} > K_{sp,PbS}$, where $[Pb^{2+}]$, $[S^{2-}]$, $[Pb^{2+}]_{eq}$ and $[S^{2-}]_{eq}$ are arbitrary (e.g., initial) and equilibrium concentration of ions Pb^{2+} and S^2, respectively. Thus, to discuss the possible formation of metal sulfide it is necessary to know the initial concentration of the ions Pb^{2+} and S^{2-}. The initial concentration of free lead ions was calculated according to (2.5) or (2.7).

The basis for the calculation of the sulfide ion concentration is the concept of the reversible decomposition of thiocarbamide in the aqueous alkaline solution by the reaction

$$N_2H_4CS \leftrightarrow H_2S + H_2NCN, \quad (2.15)$$

which was first developed in detail and justified in study [16]. According to [16], the initial concentration of the S^{2-} ions is equal to

$$[S^{2-}] = \frac{K_{H_2S}}{[H^+]^2}\left\{\frac{K_c[N_2H_4CS]\beta_c}{\beta_s}\right\}^{1/2}, \quad (2.16)$$

where $K_c = 1.6 \times 10^{-23}$ is the N_2H_4CS hydrolysis constant [16]; $\beta_s = [H^+]^2 + K_1[H^+] + K_{H_2S}$ [16]; $\beta_c = [H^+]^2 + K_1'[H^+] + K_{H_2NCN}$ [16]; $K_{H_2S} = 1.1 \times 10^{-20}$ [44] and $K_{H_2NCN} = 7.95 \times 10^{-23}$ [45], $K_1 = 8.9 \times 10^{-8}$ [44] and $K_1^* = 5.25 \times 10^{-11}$ [45] are the complete dissociation constants and the first stage dissociation constants of hydrosulfuric acid and cyanamide, respectively.

Next, from the found initial concentration of ions Pb^{2+} and S^{2-} we determine the value of the ion product and compare it with the solubility product $K_{sp,PbS} = 2.5 \times 10^{-27}$ of lead sulfide PbS [44].

Replacing in (2.5) the concentration $[Pb^{2+}]$ by its value expressed through a solubility product and concentration of sulfide ions $[Pb^{2+}] = K_{sp,PbS}/[S^{2-}]$, we obtain the expression

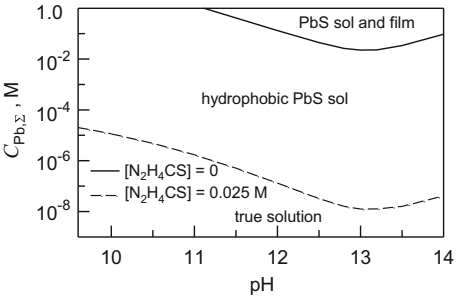

Fig. 2.7 Regions of formation of PbS as a sol and a film upon deposition from aqueous solutions of N_2H_4CS with different concentration of 0 and 0.025 mol l^{-1} [30]. The total concentration of lead, $C_{Pb,\Sigma}$, in the solutionы is shown in a logarithmic scale

$$C_{Pb,\Sigma}^{cit} = \frac{K_{sp,PbS}}{[S^{2-}]}\left\{1 + \frac{\beta_{11}}{[H^+]} + \frac{\beta_{12}}{[H^+]^2} + \frac{\beta_{13}}{[H^+]^3} + \frac{3\beta_{34}K_{sp,PbS}^2}{[H^+]^4[S^{2-}]^2} + \frac{4\beta_{44}K_{sp,PbS}^3}{[H^+]^4[S^{2-}]^3} + \frac{6\beta_{68}K_{sp,PbS}^5}{[H^+]^8[S^{2-}]^5} + \frac{2\beta_{21}K_{sp,PbS}}{[H^+][S^{2-}]} + \beta_1[Cit^{3-}] + \beta_{1,2}[Cit^{3-}]^2 + \beta_1'\frac{K_w[Cit^{3-}]}{[H^+]}\right\} \quad (2.17)$$

Thus, based on (2.5) and (2.16) we obtain the necessary data to construct the dependence $C_{Pb,\Sigma} = f(pH)$, which characterizes the equilibrium in the system between the PbS deposit and dissolved thiocarbamide and the lead complex compounds.

Figure 2.7 shows the boundaries of lead sulfide deposition at different concentrations of N_2H_4CS calculated with (2.17). From a comparison of the boundaries of the lead hydroxide formation (solid line at [N_2H_4CS] = 0 in Fig. 2.7) and the boundaries of the lead sulfide formation follows that the lead hydroxide formed at pH $\geq$ 11.1 should transform inevitably into the sulfide PbS, as the equilibrium concentration of lead above the $Pb(OH)_2$ deposit is much higher than that of the sulfide. For example, at pH = 12 the lead concentrations above the deposit of $Pb(OH)_2$ hydroxide is equal to 0.132 M, and above the sulfide PbS deposit is just 1.3×10^{-7} M (at [N_2H_4CS] = 0.025 M).

Generally, the calculation procedure proposed in studies [29, 30] is suitable for predicting the formation of solid lead hydroxide and sulfide phases in the solution, as well as reliable choosing the compositions of reaction mixtures required for PbS deposition as a sol (outside of the hydroxide region), quantum dots, core@shell heterostructures and films.

2.1.3 Deposition of Lead Sulfide Nanopowders

The chemical deposition from aqueous solutions is the most popular method used for the synthesis of lead sulfide nanopowders. The size of the obtained nanoparticles depends on the chosen reactants and their concentrations and the temperature

of synthesis. Detailed investigations of the conditions of hydrochemical deposition of stable PbS nano-particles using various reagents are reported in studies [20, 21, 46, 47].

Stable nanoparticles of the PbS powder were prepared by deposition from aqueous solutions of $Pb(OAc)_2$ [20, 21, 46, 47] or $Pb(NO_3)_2$ [47]. An aqueous solution of Na_2S served as the source of sulfur ions.

In study [21], lead acetate $Pb(AcO)_2$, sodium sulfide Na_2S and water were used for the one-pot synthesis of PbS nanoparticles in an aqueous solution. The synthesis was carried out under the ambient conditions (298 K, 1 atm). The initial concentrations of aqueous solutions of $Pb(AcO)_2$ and Na_2S salts were varied in the range of 0.0025–0.25 M. The solutions of $Pb(AcO)_2$ and Na_2S were taken in stoichiometric amounts for the each reaction and mixed with vigorous stirring. All PbS nanopowders prepared in work [21] possess a cubic *B*1 type crystal structure. The nanoparticle size *D* in synthesized PbS powders is equal to 15–20 nm. According to [21], the main drawback of synthesis without complexing agent is that the direct interaction of lead Pb^{2+} and sulfide S^{2-} ions in an aqueous solution is always accompanied by hydrolysis processes, which leads to the formation of poorly soluble impurity phases.

As complexing agents, Na_3Cit or Trilon B were used in studies [20, 46, 47].

In study [20], the $Pb(OAc)_2$ and Na_2S concentrations in the reaction mixtures were varied from 1.25 to 100 mmol l^{-1}, and those of sodium citrate and Trilon B were in the ranges of 0–100 and 0–75 mmol l^{-1}, respectively (Table 2.3). PbS nanoparticles were synthesized at a temperature of 298 K and pH of the solutions during synthesis ranged between 5.5 and 6.5. In study [47], the initial $Pb(NO_3)_2$ and Na_2S (or $Pb(AcO)_2$ and Na_2S) concentrations in all the reaction mixtures were 50 mmol l^{-1}. The concentrations of the complexing agents (sodium citrate and Trilon B) in the reaction mixtures were varied in the ranges from 12.5 to 50 mmol l^{-1}, and from 15 to 65 mmol l^{-1}, respectively (Table 2.4). Synthesis with the use of Trilon B was carried out with the addition of acetic acid CH_3COOH or sodium hydroxide NaOH and without them.

The concentration ratio of lead and sulfur ions was stoichiometric, $[Pb^{2+}]:[S^{2-}] = 1:1$, in all cases.

The solubility product of lead sulfide is low (at 298 K, the K_{sp} value is 2.5×10^{-27} [44] or 8.0×10^{-28} [36]); therefore, at a relatively high content of Na_2S in the reaction mixture, lead sulfide is formed almost immedi-ately, during 1–2 s. As a result, the reaction mixture first turns black and then, in several minutes, PbS particles settle down and the solution becomes transparent. The standard duration of synthesis providing deposition of lead sulfide powder is equal 5 min. The formation of lead sulfide nanoparticles proceeded according to reaction (2.1), while with lead nitrate the reaction was as follows:

$$Pb(NO_3)_2 + Na_2S \longrightarrow Na_3Cit \text{ or } Na_2H_2 - EDTAPbS \downarrow + 2NaNO_3. \quad (2.18)$$

Table 2.3 Condition of chemical deposition and the size of PbS particles synthesized by reaction scheme (2.1) from aqueous solutions of $Pb(OAc)_2$ with Na_3Cit or Trrilon B [20]

Concentration of reactants in the reaction mixture (mol l^{-1})[a]				t (hour)[b]	D (nm)	Lattice constant a_{B1} (nm)
Pb $(CH_3COO)_2$	Na_2S	$Na_3C_6H_5O_7$	Trilon B			
0.025	0.025	0	0	0	20–27[c]	0.5933(4)
0.005	0.005	0	0.005	0	24 ± 3	0.5933(1)
0.0125	0.0125	0	0.0125	0	30 ± 3	0.5933(1)
0.050	0.050	0	0.050	0	35 ± 3	0.59337
0.050	0.050	0	0.0125	0	8 ± 1[c]	0.5934(3)
0.050	0.050	0	0.0250	0	10 ± 1	0.5941(3)
0.050	0.050	0	0.0333	0	14 ± 2	0.5936(1)
0.050	0.050	0	0.0375	0	20 ± 3	0.5934(1)
0.050	0.050	0	0.050	0	35 ± 3	0.59337
0.050	0.050	0	0.075	0	50 ± 5[c]	0.59335
0.050	0.050	0	0.050	0	35 ± 3	0.59337
0.050	0.050	0	0.050	120	55 ± 6	0.59335
0.050	0.050	0	0.050	260	55 ± 6	0.59357
0.050	0.050	0	0.050	460	55 ± 6	0.59326
0.050	0.050	0	0.050	770	55 ± 6	0.59340
0.00125	0.00125	0.00125	0	0	No deposition	–
0.00125	0.00125	0.00125	0	1440	No deposition	–
0.0025	0.0025	0.0025	0	0	4.5–5.0[c]	0.5949(7)
0.005	0.005	0.005	0	0	4.5–5.0	0.594(3)
0.005	0.005	0.005	0	70	7–8	0.593(2)
0.0125	0.0125	0.0125	0	0	4.5–5.0	0.594(3)
0.025	0.025	0.025	0	0	4.5–5.0	0.5926(3)
0.050	0.050	0.050	0	0	7–8	0.591(1)
0.100	0.100	0.100	0	0	7–8	0.590(1)
0.025	0.025	0.025	0	0	4.5–5.0	0.5926(3)
0.025	0.025	0.025	0	70	5 ± 1	0.592(2)
0.025	0.025	0.025	0	240	5 ± 1	0.592(3)
0.025	0.025	0.025	0	360	5 ± 1	0.594(3)
0.025	0.025	0.025	0	500	5 ± 1	0.594(1)
0.025	0.025	0.025	0	720	5 ± 1	0.593(3)
0.025	0.025	0.00625	0	0	5 ± 1[c]	0.593(8)
0.025	0.025	0.0125	0	0	5 ± 1	0.593(7)

[a]The deposition time in all the experiments was 5 min
[b]The exposure time of already deposited PbS particles in the matrix solution
[c]The deposit contained impurity phases

The contents of lead, sulfur and oxygen in the annealed single-phase PbS nanopowders determined by Energy Dis-persive X-ray (EDX) analysis were 86 ± 2, 13 ± 1, and 1 ± 0.5 wt%, respectively. According to EDX data (Fig. 2.8), the impurity oxygen present in PbS nano-powders is distributed over the particle surface, the major part being present as adsorbed water and the rest oxygen being in the chemisorbed state.

All the synthesized PbS nanoparticles with any particle size had a cubic $B1$ type lattice with the lattice constant a_{B1} = 0.5902–0.5949 nm, which is in line with the results [48, 49].

The XRD pattern of a PbS sample synthesized from a reaction mixture of Pb $(AcO)_2$ and Na_2S with concentrations 25 mmol l^{-1} without adding a complexing agent is presented in Fig. 2.9. According to X-ray phase analysis, the sample contains ~45 wt% of impurity of orthorhombic (space group *Pnma*) lead sulfate $PbSO_4$. The average size D of PbS particles ranges from 20 to 27 nm and could not be determined more accurately because of the presence of impurities. A similar result was obtained during synthesis of PbS from a reaction mixture of $Pb(NO_3)_2$ and Na_2S without adding a complexing agent. Thus, synthesis in the absence of a complexing agent fails to yield pure lead sulfide. This is consistent with the data [21].

The XRD patterns of PbS powders synthesized from the reaction mixtures with equal concentrations $[Pb(AcO)_2] = [Na_2S] = [TrB]$ of lead acetate, sodium sulfide, and Trilon B are demonstrated in Fig. 2.10. The inset in Fig. 2.10 shows the dependences between the reduced diffraction reflection broadening $\beta^*(2\theta)$ of the synthesized PbS powders and the scattering vector s. The lead sulfide nanoparticle size $\langle D \rangle$ is calculated to be 24 nm when the concentrations of each reactant are equal to 5 mmol l^{-1}. If the concentrations of these components in the reaction mixture are increased to 12.5 and 50 5 mmol l^{-1}, deposited PbS nanoparticles grow to 30 and 35 nm, respectively (see Table 2.3).

Figure 2.11 displays the SEM images of the nanocrystalline PbS powder with the average particle size D = 24 nm as an example. The powder was deposited from a solution of lead acetate, sodium sulfide, and Trilon B having equal concentrations, 5 mmol l^{-1}. According to SEM data, this nanopowder consists of large irregular agglomerates (Fig. 2.11a) ranging in size from 6 to 10 μm. At a magnification of 30000 times, it is seen that these agglomerates have a loose microstructure and are formed by particles smaller than 1 μm (Fig. 2.11b). At a magnification of 100000 times, it is clear that these particles, in turn, consist of nanoparticle with apparent size from 30 to 50 nm (Fig. 2.11c). The same microstructure is typical of other synthesized nanopowders. The results of scanning electron microscopy (SEM) together with the data on coherent scattering region dimensions obtained by the X-ray method are indicative of strong agglomeration of the lead sulfide powders. The agglomeration is likely to be due to water repellence of the surface of the synthesized PbS nanoparticles.

Table 2.4 Conditions of chemical deposition and the size of PbS particles synthesized by reaction scheme (2.18) from aqueous solutions of $Pb(NO_3)_2$ with Na_3Cit or Trilon B [47]

Concentration of reactants in the reaction mixture (mol l^{-1})							t^c	D (nm)
$Pb(NO_3)_2$	$Pb(AcO)^a{}_2$	Na_2S	Trilon B	Na_3Cit^b	CH_3COOH	NaOH	(hour)	
0.05	0	0.05	0	0	0	0	0	~10–15[d]
0.05	0	0.05	0	0.025	0	0	0	6 ± 1
0.05	0	0.05	0	0.0125	0	0	0	5 ± 1
0.05	0	0.05	0	0.02	0	0	120	6 ± 1
0.05	0	0.05	0	0.05	0	0	0	6 ± 1
0.05	0	0.05	0.015	0	0	0	24	11 ± 1
0.05	0	0.05	0.015	0	0	0	72	11 ± 1
0.05	0	0.05	0.025	0	0	0	24	11 ± 1
0.05	0	0.05	0.025	0	0	0	72	11 ± 1
0.05	0	0.05	0.035	0	0	0	24	11 ± 1
0.05	0	0.05	0.035	0	0	0	72	12 ± 2
0.05	0	0.05	0.05	0	0	0	0	21 ± 3
0.05	0	0.05	0.065	0	0	0	120	78 ± 3
0.05	0	0.05	0.065	0	0	0	0	69 ± 3
0	0.05	0.05	0.035	0	0	0	24	38 ± 3
0	0.05	0.05	0.05	0	0	0	0	45 ± 3
0	0.05	0.05	0.05	0	0.05	0	0	56 ± 4
0	0.05	0.05	0.05	0	0.10	0	0	48 ± 3
0	0.05	0.05	0.05	0	0.10	0	24	55 ± 2
0	0.05	0.05	0.05	0	0.10	0	48	56 ± 2
0	0.05	0.05	0.05	0	0.25	0	0	40 ± 2
0	0.05	0.05	0.05	0	0.25	0	24	48 ± 2
0	0.05	0.05	0.05	0	0.25	0	48	49 ± 3
0	0.05	0.05	0.05	0	0.05	0	120	70 ± 5
0	0.05	0.05	0.065	0	0	0	120	86 ± 12
0	0.05	0.05	0.065	0	0.05	0	0	64 ± 3
0	0.05	0.05	0.065	0	0.05	0	72	59 ± 4
0	0.05	0.05	0.065	0	0.05	0	120	88 ± 2
0	0.05	0.05	0.10	0	0.05	0	120	95 ± 10
0	0.05	0.05	0.10	0	0.15	0	120	95 ± 10
0	0.05	0.05	0.05	0	0	0.05	0	27 ± 1
0	0.05	0.05	0.05	0	0	0.10	0	35 ± 3
0	0.05	0.05	0.05	0	0	0.15	0	32 ± 2
0	0.05	0.05	0.05	0	0	0.25	0	33 ± 2

[a] $Pb(AcO)_2 \equiv Pb(CH_3COO)_2$
[b] $Na_3Cit \equiv Na_3C_6H_5O_7$
[c] The exposure time of already deposited PbS nanopowder in the matrix solution
[d] Deposited PbS powder contains sulfate impurity phase $PbSO_4$, so the particle size of PbS was evaluated only roughly

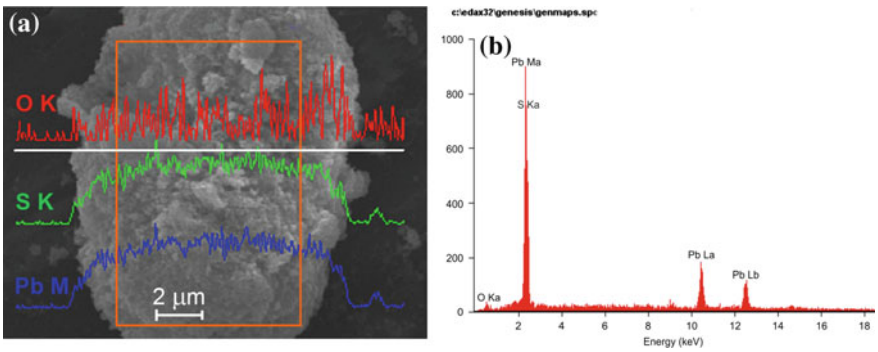

Fig. 2.8 EDX analysis of Pb, S, and O distributions in PbS nanopowders. **a** the EDX distributions of Pb, S, and O and scanning direction (*white horizontal line*) of the agglomerated PbS particle during X-ray energy dispersion analysis. *Red rectangle* shows a part of the agglomerate from which its cumulative EDX pattern **b** is collected. Reprinted from [20] with permission from Elsevier

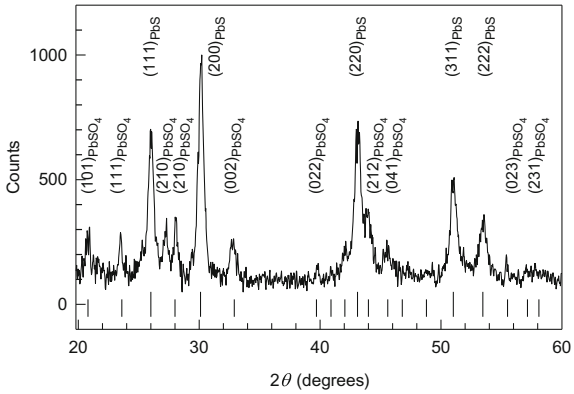

Fig. 2.9 XRD pattern of PbS nanopowder synthesized without a complexing agent from a reaction mixture of lead acetate and sodium sulfide having equal concentrations, 25 mmol l^{-3}. The long and short ticks correspond to diffraction reflections of lead sulfide PbS and lead sulfate $PbSO_4$. The XRD pattern is recorded in Cu$K\alpha_{1,2}$ radiation. Reprinted from [20] with permission from Elsevier

The concentration of Trilon B influences both the phase composition of the deposited powders and the nanoparticle size. A powder precipitates from a mixture with the minimum Trilon B concentration of 12.5 mmol l^{-1} contained ~15 wt% of lead sulfate impurity (Fig. 2.12). The lead sulfate and sulfur impurity phases in amounts of ~10 and ~8 wt%, respectively, were found in the precipitates obtained from the reaction mixture with the maximum Trilon B concentration of 75 mmol l^{-1}. Generally, upon the deposition of PbS powder with Trilon B, the

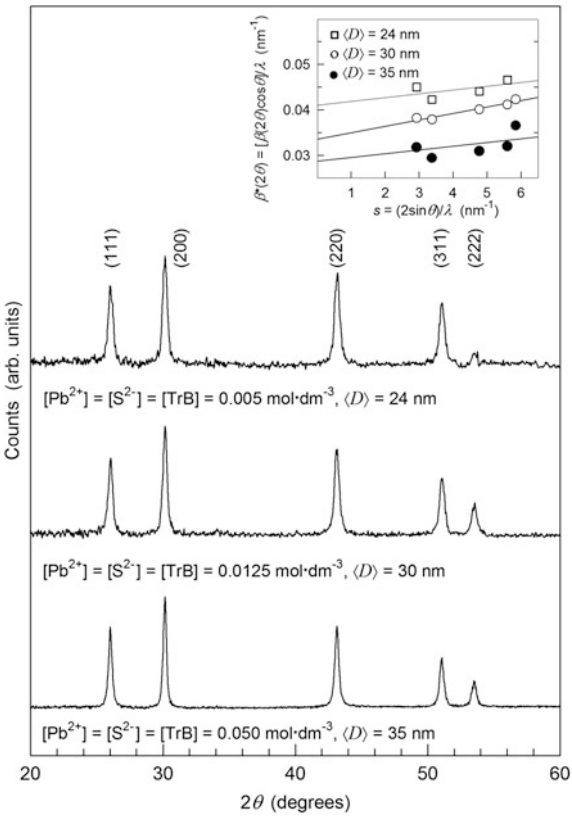

Fig. 2.10 XRD patterns of nanocrystalline PbS powders synthesized in a reaction mixtures with equal concentrations of lead acetate, sodium sulfide, and Trilon B. The *inset* shows the dependences of reduced diffraction reflection broadening $\beta^*(2\theta)$ of synthesized PbS powders on the scattering vector s: *Open square* synthesis from the reaction mixture with reactant concentrations 5 mmol l^{-1}; *Open circle* 12.5 mmol l^{-1}; and *Filled circle* 50 mmol l^{-1}. The *solid lines* denote approximating of $\beta^*(s)$ dependences. All the XRD patterns are recorded in Cu$K\alpha_{1,2}$ radiation. Reprinted from [20] with permission from Elsevier

impurity phases are absent only if the $[Pb^{2+}]$:$[S^{2-}]$:[TrB] concentration ratio is from 1:1:1 to 1:1:(1/2).

As the Trilon B concentration increases from 12.5 to 75 mmol l^{-1}, nanoparticles measuring 8–50 nm are formed (Fig. 2.13). The increase in the exposure time of the synthesized PbS particles in the matrix solution also induces growth of the nanoparticles.

When sodium citrate is used in a reaction mixture with low (1.25 mmol l^{-1}) concentrations of $Pb(OAc)_2$, Na_2S and Na_3Cit, no lead sulfide precipitate is formed. The deposition of PbS was observed from reaction mixtures containing lead acetate, sodium sulfide and sodium citrate in equal concentrations ranging from 2.5 to 100 mmol l^{-1}. During deposition from a citrate-containing reaction mixture with reactant concentrations of 2.5 mmol l^{-1}, an impurity phase $PbSO_4$ was present in the nanopowder along with lead sulfide. The deposits from the mixtures with large concentrations of reactants did not contain any impurity phases. The XRD patterns of the powders synthesized from citrate-containing mixtures have very broad diffraction reflections (Fig. 2.14). The particle size estimated from diffraction

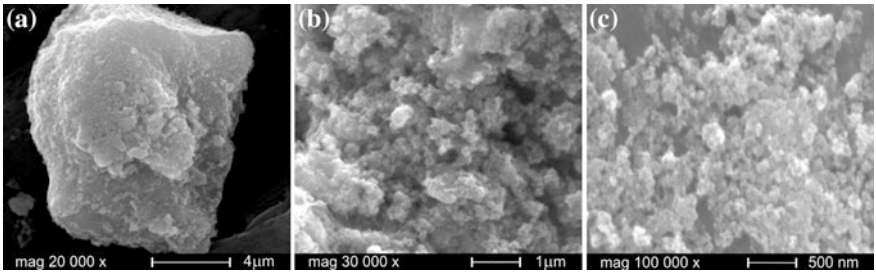

Fig. 2.11 The microstructure of PbS nanopowder synthesized from a mixture of lead acetate, sodium sulfide, and Trilon B having equal initial concentrations, 5 mmol l^{-1}: **a** at a magnification of 20000 times large agglomerates of size to 10 μm are visible, **b** loose microstructure of the agglomerate at a magnification of 30000 times; **c** magnification of 100000 times. Reprinted from [20] with permission from Elsevier

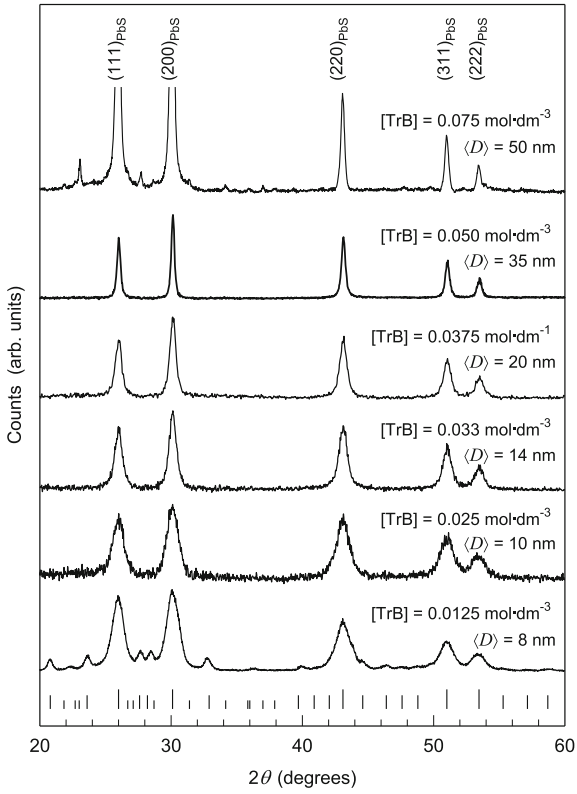

Fig. 2.12 XRD patterns of nanocrystalline PbS powders synthesized from a mixture of lead acetate and sodium sulfide with initial concentrations 0.050 mol dm^{-3} and Trilon B with initial concentration [TrB] ranging from 12.5 to 75 mmol l^{-1} [20]. The long, medium, and short ticks correspond respectively to diffraction reflections of lead sulfide PbS, lead sulfate $PbSO_4$, and sulfur S. The XRD pattern is recorded in Cu$K\alpha_{1,2}$ radiation. Reprinted from [20] with permission from Elsevier

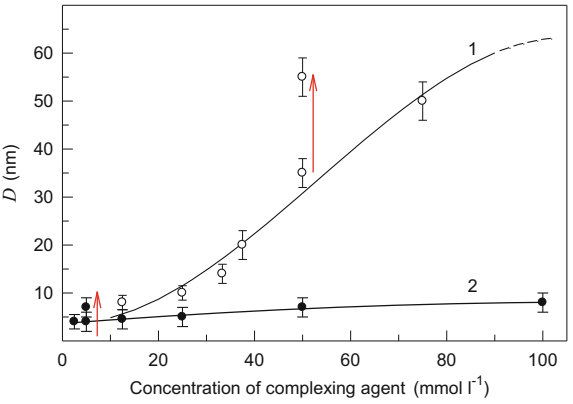

Fig. 2.13 Effect of the concentration of complexing agents Trilon B (1) and sodium citrate (2) on the lead sulfide nanoparticle size *D* upon deposition from the reaction mixture of lead acetate and sodium sulfide having equal reactant concentrations [20, 47]. The *arrows* indicate the increase in the PbS particle size upon 70 h (for citrate solution) and 120 h (for Trilon B solution) exposure in the matrix solution

reflection broadening is from 4–5 to 7–8 nm (see Table 2.3) and increases slightly with increasing concen-tration of Na_3Cit (see Fig. 2.13).

Lead sulfide nanopowders consisting of small particles with average size of 5–15 nm were prepared from reaction mixtures containing $Pb(NO_3)_2$ and Na_2S using sodium citrate as the complexing agent. A change in the Na_3Cit concentration from 12.5 to 50 mmol l^{-1} does not affect the average PbS particle size to within the error of measure-ments. When Na_3Cit is replaced by Trilon B, nanopowders with larger particles with size up to 20 nm are formed in reaction mixtures containing $Pb(NO_3)_2$ and Na_2S.

Thus, according to studies [20, 46, 47], the size of lead sulfide particles obtained by deposition from aqueous solutions depends on the reactant concentrations and the type of complexing agent. By varying these parameters, the PbS particle size can be controlled in the range from 5 to 55 nm at 298 K. For the targeted synthesis of PbS nanoparticles of <10 nm size, it is reasonable to use sodium citrate, while for the preparation of larger particles (up to 50 nm), Trilon B should better be used. Even coarser PbS particles can be obtained by deposition in the temperature range of 330–340 K or using thiourea N_2H_4CS instead of Na_2S [50].

A method for preparing nanocrystalline PbS powder using aqueous solutions of lead nitrate $Pb(NO_3)_2$ is protected by the patent [51].

Uniform cube-shaped PbS nanoparticles with an edge length of 22 nm were obtained by hydrochemical deposition from solutions of lead acetate and sodium thiosulfate in the presence of $C_{17}H_{33}COOK$ as a surfactant [52].

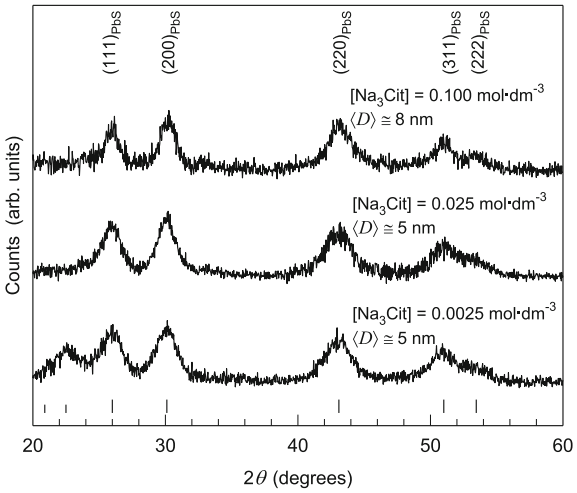

Fig. 2.14 XRD patterns of the nanocrystalline PbS powders synthesized from reaction mixtures of lead acetate, sodium sulfide, and sodium citrate. The XRD pattern of the powder deposited from a mixture with the initial concentrations 5 mmol l^{-1} contains diffraction reflections of impurity $PbSO_4$. The long and short ticks correspond to the diffraction reflections of lead sulfide PbS and lead sulfate $PbSO_4$, respectively. The XRD pattern is recorded in Cu$K\alpha_{1,2}$ radiation. Reprinted from [20] with permission from Elsevier

A sort of bath deposition of nanoparticles is electrochemical deposition. In this case, particles are formed as electrical current is passed [53, 54]. Nanocrystalline PbS is synthesized in an aqueous solution of Na_2S with metallic lead as the sacrificial anode and polyvinyl alcohol as the stabilizer [55]. Upon application of an electrical potential to the electrodes, PbS nanoparticles of 8–10 nm size are formed in the solution. According to Yang et al. [53], by varying the potential value and scan rate, it is possible to synthesize PbS nanoparticles with a size in a specified narrow range from 3 to 7 nm. An advantage of electrochemical deposition is the possibility of more accurate control over the nanoparticle size. Also, in the case of long deposition time, it is possible to eliminate unstable compounds from the list of reactants.

Lead sulfide nanoparticles can also be synthesized by a sol-gel process [56]; however, this does not ensure the formation of monodisperse particles.

Lead sulfide nanoparticles and nanostructures are synthesized in spatially confined colloidal systems—colloidal nanoreactors. Most often, these are reverse micelles, liquid crystals, adsorption layers, Langmuir-Blodgett films [57] and microemulsions. The confinement of the reaction zone in which the nanophase is formed provides a high degree of monodispersity for the resulting particles. The molecules that confine the reaction zone should be amphiphilic, i.e, they should have a nonpolar tail soluble in nonpolar solvents, or a hydrophobic tail and a polar hydrophilic head. The amphiphilic properties are inherent in surfactant molecules and ions. When they get in water, surfactant molecules cover the water surface by

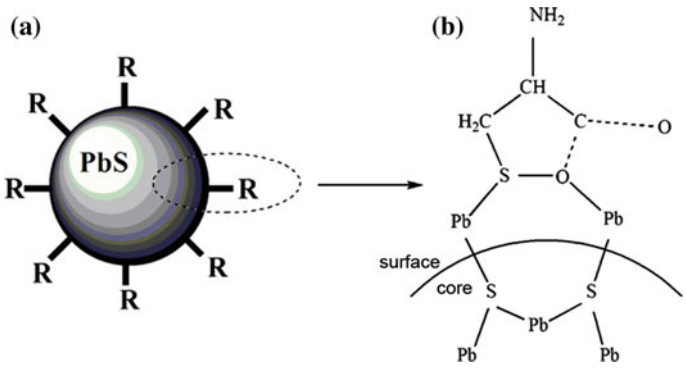

Fig. 2.15 Schematic structure of a **a** PbS nanoparticle with the surface coated by the *L*-cysteine capping agent and **b** a PbS nanoparticle-cysteine coating complex [58]. The radical (substituent) R is a part of *L*-cysteine molecule

forming a monomolecular film. In the film, the polar part of the molecule is immersed in water, while the nonpolar hydrophobic substituent is located in air, and the water surface tension is thus decreased. After the surface has been covered, new surfactant molecules and ions pass to the bulk of water.

In non-polar solvents, colloidal structures are formed in which the hydrocarbon tails are arranged at the outward normal to the surface – reverse micelles and water-in-oil microemulsions. In reverse micelles, hydrophilic groups form a polar core, while the hydrophobic tails point outwards. For the chemical synthesis of nanoparticles, reverse micelles are used most often. In order to stabilize the nanoparticles, compounds that modify and coordinate the surface atoms of the particles are added to the micellar solution [58]. As an example, Fig. 2.15 shows the schematic structure of a PbS nanoparticle with the surface coated by *L*-cysteine $C_3H_7NO_2S$, which serves as the capping agent [58].

Organometallic synthesis of colloid chalcogenide nanoparticles in organic solvents in the presence of trioctylphosphine oxide (TOPO) has been reported by Gerion, Alivisatos et al. [59]. A drawback of this method is that the nanoparticles are soluble only in organic solvents. For using these nanoparticles in biological media, it is necessary to endow them with water solubility by forming hydrophilic groups on the surface. The process of particle stabilization and transfer to the aqueous phase is called solubilization. One solubilization method implies the formation of a polymer layer around the nanoparticle [60]. In this case, the hydrophobicity of the TOPO molecules located on the nanoparticle surface is used for binding the hydrophobic groups of solubilizing polymers (block copolymers, polyethylene glycol (PEG) and so on) (Fig. 2.16). The hydrophilic groups of these polymers point towards the surrounding aqueous solution and form an insulating polar shell. This shell contains active groups for attachment of biological molecules (antibodies, peptides, DNA molecules).

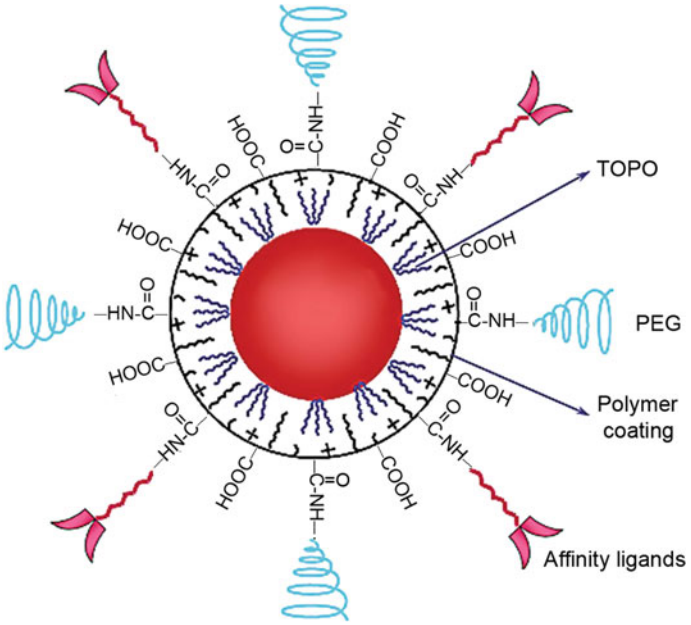

Fig. 2.16 Scheme of the formation of a hydrophilic polymer layer on a quantum dot [60]. The quantum dot includes a TOPO-coated core and a polymeric shell with attached amphiphilic PEG layer and biocompatible ligands

2.1.4 Deposition of Lead Sulfide Particles with Different Morphology

The hydro- and solvothermal synthesis at a temperature of >300 K can be considered as a sort of chemical bath deposition. Note that in some publications, chemical bath deposition followed by heat treatment of the resulting lead sulfide powder is erroneously described as hydro- or solvothermal synthesis.

Lead sulfide nanorods ~80 nm in diameter and ~400 nm in length and dendrite nanostructures were obtained by chemical deposition from aqueous solutions of lead acetate and thioacetamide without using ligands or templates [61]. A distinctive feature of this method is the use of solutions of reactants with concentrations differing 5–40 fold. The synthesis was carried out under ambient conditions by adding a highly concentrated solution of one reactant to a solution of the second reactant with a low concentration.

Hydrothermal deposition was used to obtain nanowires and star-shaped PbS crystals [62], and also well-faceted cubic nanostructures [63]. By using non-aqueous solvents (ethyl alcohol, ethylene glycol, ethylenediamine, triethylene glycol, propylene glycol and so on), one can deposit lead sulfide with various particle morphology – dendrite [64–66] and many-arm star-shaped structures [15, 67],

separate nanospheres [68], nanotubes with different cross-section shapes [69–71], and flower-like structures [72, 73]. For example, Sun et al. [72] prepared flower-like lead sulfide nanoparticles by thermal decomposition of lead diethyldithiocarbamate dissolved in ethylenediamine (the solution was heated by microwave radiation). The reported micrographs [72] indicate that the flower petals are composed of well-faceted cubic or rectangular PbS particles. Shakouri-Arani and Salavati-Niasari [74] prepared 11 different morphological forms of lead sulfide by solvothermal synthesis from $PbNO_3$ and $C_{13}H_{11}NS$. Propylene glycol served as the solvent; the synthesis was carried out at 433 K; and the duration of the synthesis ranged from 8 to 24 h for the preparation of PbS with different morphology.

The micrographs of lead sulfide nanoparticles with different morphology obtained by hydro- and solvothermal synthesis – nanowires and star-shaped crystals [62], nanotubes [71], many-arm structures [72] and "flowers" [73] – are presented in Fig. 2.17. By ultrasonic treatment of a solution of lead sulfide, it is possible to obtain PbS as separate nanospheres [67], dendrite structures [65] and nanotubes with a square cross-section [71].

It was shown [75] that thermal radiolysis (electron beam irradiation) of a solution containing precursors for the synthesis of nanocrystalline PbS gives rise to particles of equal size, i.e, the final material becomes more uniform. As the reactants, the reseachers [75] used solutions of lead acetate and thioacetamide in polyvinyl alcohol.

An interesting method for the preparation of hollow spherical PbS nanoparticles has been proposed [76]. Aqueous solutions of lead nitrate and sodium thiosulfate

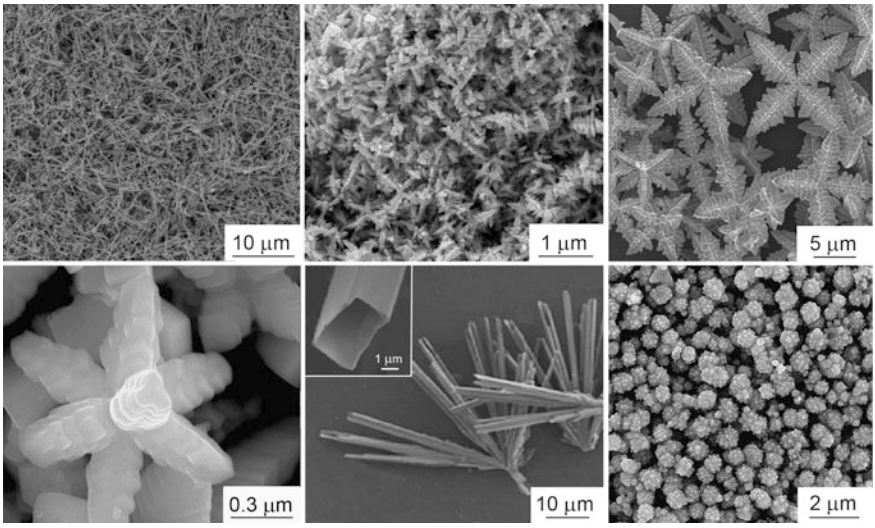

Fig. 2.17 Micrographs of nanoparticles of nanostructured lead sulfide with different morphology obtained by hydro- and solvothermal synthesis. **a** Nanowires [62], **b** dendrites [66], **c** stars [62], **d** many-arm crystals [72], **e** nanotubes with a square cross-section [71], **f** "flowers" [73]

were used, thiosulfate solution being slowly added dropwise to a $PbNO_3$ solution. Then the reaction mixture was maintained for 2 h at a temperature of 403 K. First, the lead thiosulfate complex was formed in the solution

$$Pb^{2+} + 2S_2O_3^{2-} \rightarrow \left[Pb(S_2O_3)_2\right]^{2-}, \tag{2.19}$$

and on heating, this complex decomposed to give lead sulfide, sulfur and gaseous sulfur dioxide

$$\left[Pb(S_2O_3)_2\right]^{2-} \rightarrow PbS + S + SO_2 \uparrow + SO_4^{2-}. \tag{2.20}$$

During the synthesis [76], PbS nanoparticles of up to 10 nm size were located on the surface of SO_2 gas bubbles and gradually these structures were transformed into hollow spheres 2–40 nm in diameter. In other words, SO_2 gas functioned as a template and played the key role in the growth of hollow nanospheres from PbS nanoparticles (Fig. 2.18).

Thus, hydro- and solvothermal synthesis can produce a variety of morphological types of lead sulfide. The reasons for the formation of PbS particles of different shapes are not entirely clear, as there are very few experimental or theoretical results on this subject in the literature. Probably, the formation of nanoparticles of different morphology is related to their nucleation and growth kinetics. The nanoparticle nucleation and growth are the subjects of only two comprehensive studies [77, 78] carried out for cadmium sulfide nanoparticles by ultrafast small angle X-ray scattering (SAXS). Data on nucleation and growth of PbS nanoparticle are lacking. The use of elevated temperature for the synthesis promotes the growth of PbS particles; therefore, the characteristic particle size is often beyond the conventional upper boundary (40–60 nm [8, 79–82]) of the range defined for nanocrystalline substances.

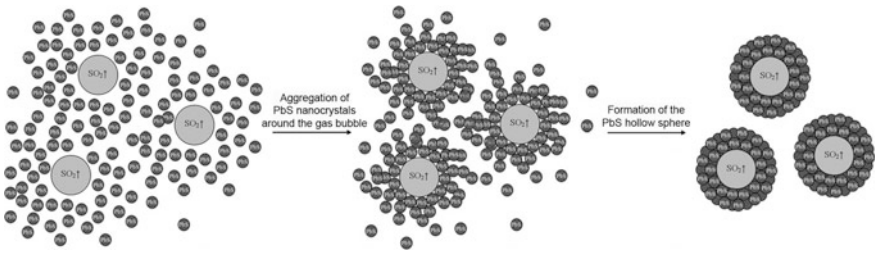

Fig. 2.18 Scheme of formation of hollow spheres from PbS nanoparticles [76]

2.1.5 Lead Sulfide Quantum Dots

The use of semiconductor quantum dots implies the presence of a matrix. Most often, glass, porous ceramics, or substrates are used as QD matrices; therefore, the syntheses of QDs and the matrix are often combined.

Lead sulfide quantum dots are prepared in various media (in glasses [83–86], porous ceramics [87], sol-gel films [88] or polymers [89, 90]) and are deposited on various substrates, for example, GaAs [91].

Okuno et al. [83] obtained PbS quantum dots in a low- melting phosphate glass. A mixture of glass powder and PbS was melted at ~1300 K. Then the resulting glass was annealed at ~670 K for a period from several minutes to an hour. After annealing, the glass acquired a brown or black color as a result of formation of PbS with an average radius of 2–3 nm, which is much smaller than the lead sulfide exciton radius (18 nm). The PbS quantum dots with a radius of 1.3 nm were also synthesized by passing hydroen sulfide through an aqueous solution of polyvinyl alcohol and lead acetate.

Del Monte et al. [87] grew PbS quantum dots in a hybrid porous organo-inorganic ceramic prepared using 3-mercaptopropyltrimethoxysilane $(MeO)_3Si(CH_2)_3SH$. The growth of the quantum dots is presented schematically in Fig. 2.19. The quantum dots are formed in the pores of the ceramic saturated with a lead acetate solution in acetic acid with diffusion of gaseous hydrogen sulfide through the ceramic.

The growth of lead sulfide QDs is terminated owing to the interaction of the formed PbS particles with 3-mercaptopropyl group giving a 3-mercaptopropyl shell

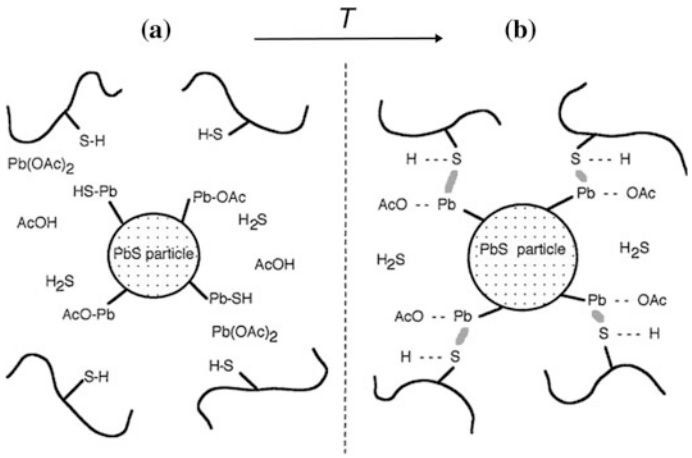

Fig. 2.19 Scheme of PbS nanoparticle growth in the pores of hybrid organo-inorganic ceramics [87]. **a** The formation and growth of PbS particles occur *via* the reaction of lead acetate with gaseous hydrogen sulfide; **b** interaction of PbS particles with 3-mercaptopropyl to give a 3-mercaptopropyl shell on the PbS particle surface and termination of the particle growth

on the particle surface. Sulfidation was carried out at a temperature of 398–418 K for 16–32 h. The size of quantum dots obtained under different conditions was in the range from 11 to 14 nm.

An organically modified SiO_2 gel was used [88] as the matrix for PbS quantum dots. A colloidal dispersion of lead sulfide was prepared by a sol-gel process using complexing agents such as Trilon B and 3-mercaptopropyltrimethoxysilane. Lead sulfide quantum dots with average diameters of 2 and 11 nm, respectively, distributed in a polyvinyl alcohol film, have been studied [89, 90]. The chemical deposition of PbS quantum dots from aqueous solutions of lead acetate and sodium sulfide in the presence of *L*-cysteine as a complexing and stabilizing agent has been considered [58, 92]. The size of the resulting lead sulfide QDs was 10–20 nm (Fig. 2.20).

The photoluminescence of PbS quantum dots was studied in quite a number of publications [10, 12–14, 58, 70, 83, 91, 92].

Deng et al. [10] proposed a method for solubilization of oleic acid-coated lead sulfide QDs, which provides their transfer into the water-soluble form with high fluorescence. The main idea of the method is that various hydrophilic thiol ligands, including glutathione $C_{10}H_{17}N_3O_6S$ and *L*-cysteine, are used as capping agents. Glutathione proved to be especially efficient.

The initial oil-soluble PbS quantum dots were synthesized in two stages. First, lead oleate was prepared from solutions of lead acetate, oleic acid and *n*-decane at 403 K. Then an aqueous solution of sodium sulfide was added dropwise to this solution; as a result, PbS quantum dots coated by oleic acid were formed and grew at the interface between two liquid phases (water and *n*-decane). In order to switch to water-soluble QDs, oleic acid molecules were replaced by thiol ligands. The

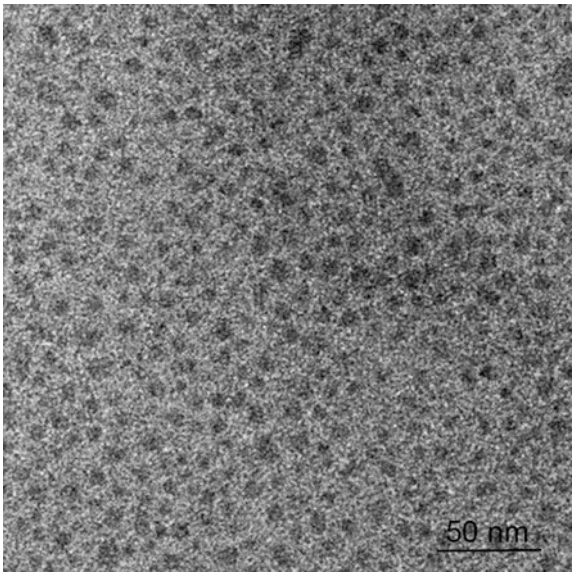

Fig. 2.20 HRTEM image of PbS quantum dots obtained in an aqueous solution of lead acetate, sodium sulfide and *L*-cysteine [58]

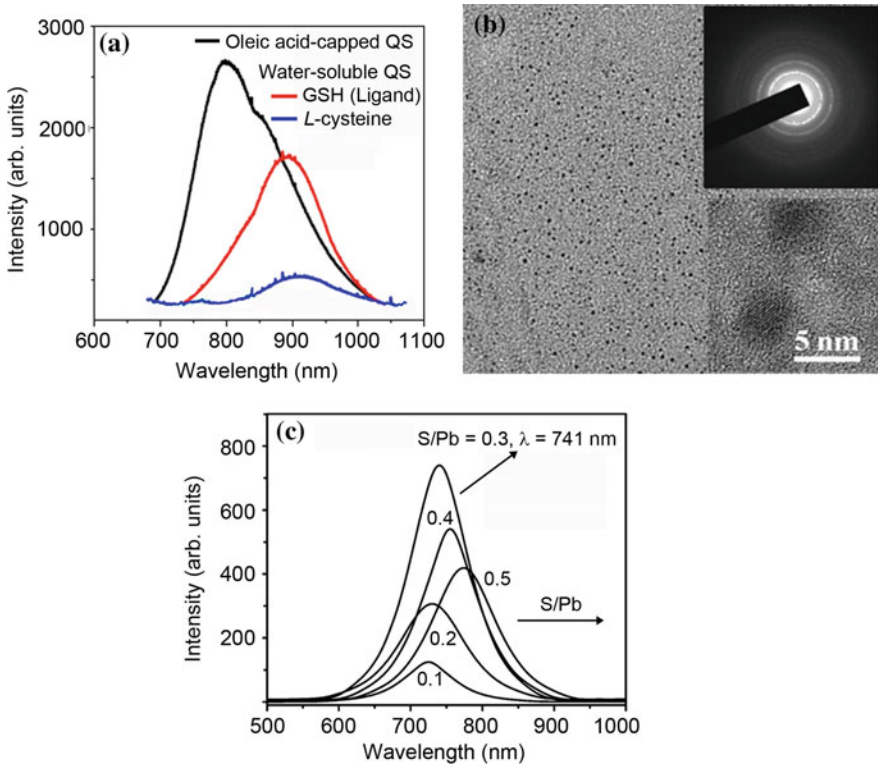

Fig. 2.21 Lead sulfide quantum dots and their properties. **a** Influence of the ligand nature on photoluminescence spectra [10]; **b** uniform distribution of monodisperse PbS QDs with a glutathione shell in an aqueous solution (the *upper* and *lower insets* show the HRTEM image and the electron-diffraction pattern of QDs) [10]; **c** change in intensity and red shift of the luminescence maximum of the *L*-cysteine-coated PbS QDs depending on the sulfur and lead concentration ratio S/Pb in the solutions [58]

intensity of photoluminescence of the synthesized monodisperse water-soluble PbS quantum dots depended on the sort of the ligand. The highest radiation intensity, which amounted to ~70% of the luminescence intensity of organic QDs, was achieved by using glutathione (Fig. 2.21a). The radiation intensity of PbS quantum dots with an *L*-cysteine shell amounted to 20% of the initial intensity. Transition from the initial QDs to water-soluble ones is accompanied by a red shift of the luminescence maximum from 800 to 890 and 920 nm in the case of glutathione and *L*-cysteine, respectively (see Fig. 2.21a). In the opinion of Deng et al. [10], the observed effect is due to the change in the electron density and confinement as a result of formation of Pb-thiol bonds. The formation of these bonds induces also a minor increase in the size of inorganic core of a quantum dot compared with the core of the initial oleic-acid coated PbS quantum dot. Figure 2.21b shows a TEM image of water-soluble glutathione-coated lead sulfide QDs with an emission max

imum at 800 nm. The 4–5 nm PbS quantum dots are uniformly distributed in the solution and, according to electron diffraction data (see the lower inset in Fig. 2.21b), they have a cubic structure.

Yu et al. [58] studied the photoluminescence of lead sulfide QDs with a cysteine shell. The 7–8 nm quantum dots were synthesized from aqueous solutions of lead acetate, *L*-cysteine and sodium sulfide. The highest photoluminescence intensity was found for the QDs synthesized from a solution with the Pb:cysteine:S concentration ratio of 1:2.2:0.3; the intensity maximum was observed at a 741 nm wavelength (Fig. 2.21c). It was demonstrated that photoluminescence of the QDs with cysteine shell depends on the pH of the medium and S:Pb and cysteine/ Pb concentration ratios in the solution (see Fig. 2.21c). An increase in the S/Pb ratio induced a red shift of the emission maximum from 725 to 780 nm. A similar shift of the photoluminescence peak was observed in another study [10].

Lead sulfide QDs on semiconductor substrates (like GaAs) are grown by molecular-beam epitaxy method but in this case, a heteronanostructure is formed.

2.1.6 Nanostructured Lead Sulfide Films

The methods used to obtain nanostructured chalcogenide films can be classified into chemical and physical ones.

The key chemical methods for the fabrication of nanostructured lead sulfide films include deposition from colloidal solutions, chemical vapour deposition, electrochemical deposition, spray pyrolysis, photocatalytic chemical deposition and successive ionic layer adsorption and reaction (SILAR). Among the physical methods for the preparation of PbS films, the major ones are various alternatives of gas phase deposition (vacuum evaporation, molecular-beam epitaxy, glow discharge ion sputtering, ion beam sputtering, ion deposition, reactive ion sputtering, magnetron ion sputtering and high-frequency ion sputtering). Often, combined physical and chemical methods are used to prepare lead sulfide films [93].

Chemical bath deposition of films is distinguished by simplicity and the possibility to deposit a film on a surface of any size and any configuration; there is no need to heat the substrates to high temperature, and the use of toxic or explosive chemicals is avoided.

Three mechanisms of chemical bath deposition of films can be conventionally distinguished: ionic, cluster (hydroxide or colloid) and ionic cluster mechanisms [6, 23, 26, 94]. In the ionic mechanism, the sulfide nucleation occurs upon the reaction between Pb^{2+} and S^{2-} ions directly on the substrate. According to the cluster (colloid) mechanism, it is assumed that the solid phase nucleation and cluster formation take place in a homogeneous solution, while the growth, coagulation and adsorption occur on the substrate [6, 32]. It is more likely that sulfide films are deposited by a mixed mechanism. In this case, the sulfide is formed both upon the direct reaction between the metal and sulfide ions and upon adsorption of the

sulfidizer on the surface of hydroxide particles to give intermediate complexes, which decompose to give the sulfide.

The chemical deposition of PbS films on a glass sub-strate has been studied in detail in work [95–100]. Three synthetic procedures were used. According to the first procedure, the PbS-1 film was deposited from aqueous solutions of $Pb(OAc)_2$ and N_2H_4CS in the presence of Na_3Cit and NaOH without stirring of the solution. In the second procedure, the film was deposited under the same conditions as in the first one but without the addition of sodium citrate, and the deposition was carried with stirring (PbS-2 film) or without stirring (PbS-3 film). In the third synthetic procedure, the PbS film was formed on the surface of a Trilon-containing aqueous solution of lead acetate owing to the reaction of the latter with gaseous hydrogen sulfide; the resulting film (PbS-4) was transferred onto a glass substrate. The PbS-1 film was additionally annealed in air at temperatures from 293 to 423 K with a step of 40 K.

The average grain size of PbS-1 film in the substrate surface was ~250 nm; however, upon a 20000-fold magnification (Fig. 2.22a), one can see that the grains

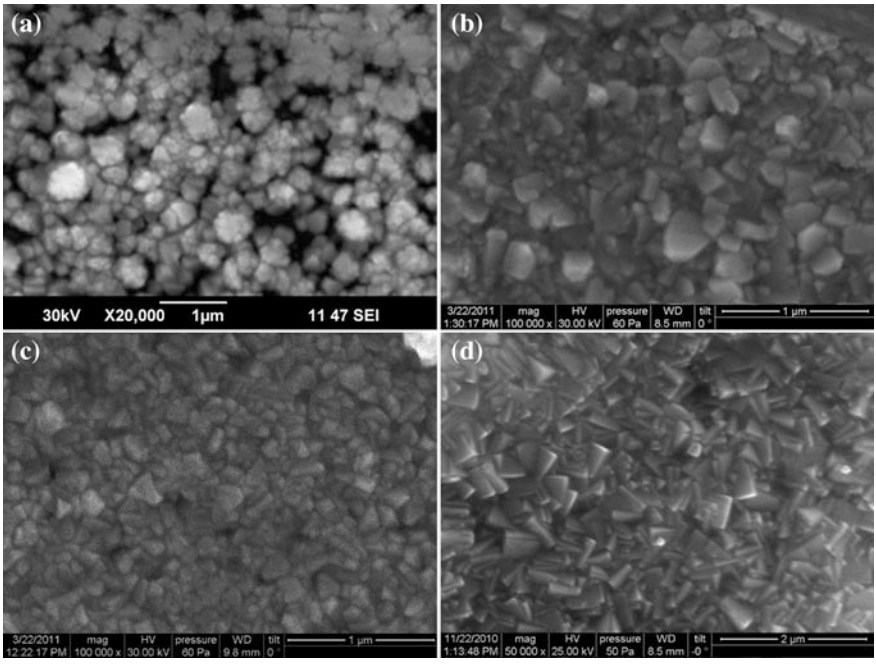

Fig. 2.22 Micrographs of **a** PbS-1, **b** PbS-2, **c** PbS-3, and **d** PbS-4 films [100]. **a** In the PbS-1 film, the nanoparticles smaller than 80–100 nm are assembled into larger aggregates of up to 200–250 nm size; the degree of film continuity does not exceed 80–85%; **b** the PbS-2 film completely coats the substrate; **c** the PbS-3 film microstructure is most uniform in grain size; **d** grains of PbS-4 film are well-faceted; more than 65% of grains have a size less than 120 nm, and ~6% of grains have a size from 250 to 400 nm. Reprinted from [100] with permission from Elsevier

are agglomerates of nanoparticles of the <100–120 nm size. The degree of continuity of PbS-1 films was not more than 80–85%. The PbS-2, PbS-3 and PbS-4 films completely coated the substrate (Fig. 2.22b–d). The smallest nanoparticle size was observed in the PbS-3 film (see Fig. 2.22c). In the PbS-4 films (see Fig. 2.22d), all grains were well-faceted and the size of most grains was <120 nm. The smaller particle size of PbS-2 and PbS-3 films compared with PbS-1 is due to the fact that the deposition was carried out without sodium citrate. In the absence of sodium citrate, the rate of formation of PbS nuclei decreases but the number of the nuclei increases, which results in a relative decrease in the particle size. The observed size of PbS nanoparticles in the films varies over a broad range, from 10 to 160 nm, the average size being 50–70 nm [97–100].

A simple method for the preparation of nanostructured PbS films, ensuring a specified range of band gap energies, has been proposed and patented by Sadovnikov and Rempel [101]. Lead sulfide nanofilms active in the near-IR range were prepared by deposition from aqueous solutions of lead acetate and thiourea in the presence of sodium citrate and sodium hydroxide; the solution pH was 10–13. By varying the reactant concentration ratio, PbS films with a controlled average particle size ranging from 35 to 80 nm were obtained in study [101].

In the case of chemical vapour deposition [102], the substrate is exposed to vapour of one or several compounds or to reactive gases which are components of the deposited material. The compound is formed via layer-by-layer condensation of atoms (molecules), similarly to the preparation of semiconductors using physical deposition methods (evaporation or ion sputtering). The difference is in the fact that in the case of chemical vapour deposition, the product arises as a result of heterogeneous chemical reaction. The advantages of this method include the possibility of high-rate deposition and doping and growing of epitaxial layers with low impurity contents. However, this method also has disadvantages, including the complexity of deposition and the necessity to heat the substrate to high temperature, which restricts the choice of the substrate material.

The spray pyrolysis method [103, 104] implies spraying a solution, most often, aqueous one, containing salts of components of the deposited compound onto a heated substrate. As the sprayed solution hits the hot substrate surface, it pyrolytically decomposes, and the reaction prod-uct forms separate crystallites or groups of crystals on the surface. This method is suitable for the preparation of films with strong adhesion to the substrate and high mechanical strength, stable under ambient conditions and at elevated temperature. A drawback of this method is the absence of direct correlation between the compositions of the deposited compounds and the sprayed solution.

The SILAR method for the preparation of thin films proposed in 1985 [105] and patented in 1987 [106] is based on the heterogeneous reaction taking place at the liquid/solid interface between the Pb^{2+} cations adsorbed on the substrate and the S^{2-} anions located in the solution [9, 107–111]. This method is schematically shown in Fig. 2.23. The purified substrate is placed into a solution containing Pb^{2+} cations (stage *a*), which are adsorbed on the substrate surface. In stage *b*, the surface is cleaned from non-adsorbed lead cations. A lead sulfide nanolayer is formed in stage

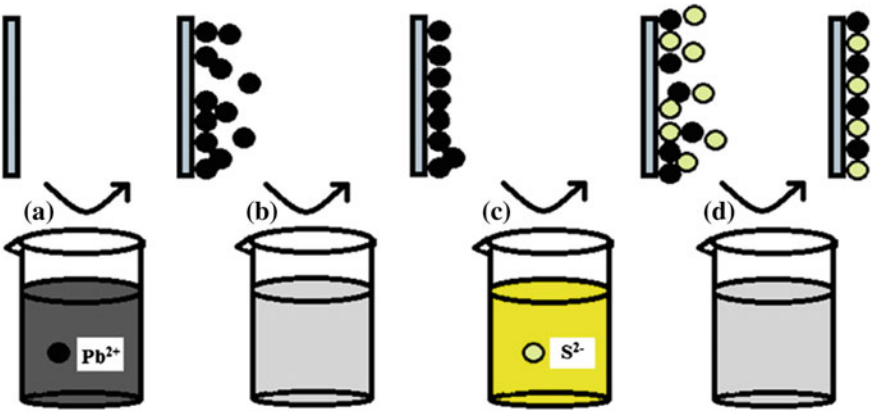

Fig. 2.23 Schematic diagram of the SILAR method [111]. **a**, **c** cationic and anionic precursoe, respectively; **b**, **d** double distilled water. For stages **a**–**d**, see the text also

c, when the substrate bearing the adsorbed Pb^{2+} ions is dipped into a solution containing S^{2-} anions. As a result of reaction between the sulfide anions and lead cations, a thin layer of lead sulfide is formed (stage *d*) (see Fig. 2.23). The deposition process repeated many times provides a layer-by-layer growth of the PbS film of a specified thickness with particles of a desired size on substrates of different type and shape [107–111].

The successive layer ionic deposition as a preparation method for thin-film coatings is upgraded hydrochemical deposition method, which makes it possible to control the morphology and thickness of the obtained films [107–111]. By using various reagents and by varying their concentration and the number of deposition cycles, it is possible to grow polycrystalline PbS films with predominant particle growth along a particular crystallographic direction [108].

An interesting method is photocatalytic chemical deposition of films [112, 113]. Zhukovskiy et al. [113] dipped a TiO_2 nanofilm on a substrate into a lead acetate and sulfur solution in ethyl alcohol. The TiO_2 nanofilm served as the catalyst. When this system was exposed to light, the following processes took place: photocatalytic reduction of sulfur with ethanol, the formation of lead sulfide and deposition of 4–10 nm PbS nanoparticles on the TiO_2 surface. An atomic force microscopy study of the surface of PbS/TiO_2 nanocomposites showed the products of the photocatalytic deposition of lead sulfides to be rod-like 30 nm nanoaggregates. The polycrystalline PbS nanorods are oriented normally to the surface of TiO_2 films and consist of separate nanosized sulfide particles manifesting pronounced quantum confinement effects [113]. Zhukovskiy et al. [113] proposed a mechanism of the formation of PbS nanorods on the surface of nanocrystalline TiO_2 films.

The problems of manufacture of photocatalysts by depositing PbS on TiO_2 are considered in a review [114].

Thin nanostructured films are formed by vacuum evaporation followed by deposition and molecular-beam and gas phase epitaxy. Because of specific features

of the deposition process (high vapour supersaturation, specific condensation kinetics, sharp change in the velocity of vaporized atoms on going to the absorbed state), the resulting fine-grained nanofilms are thermodynamically non-equilibrium and contain a large number of "frozen" structural defects. Therefore, this method is more suitable for the preparation of lead sulfide nanocrystals without aggregation on a large surface area.

Well-faceted PbS nanoparticles on an Al_2O_3 substrate were obtained in study [115] by a combined physical and chemical method. A porous membrane with 20 nm holes was used as the template. A metallic lead melt heated to 673 K was hydraulically injected through the membrane nanopores. Sulfidation of lead nanowires was carried out by gaseous hydrogen sulfide. This gave a dense layer of PbS nanoparticles of 100 nm and smaller size (Fig. 2.24). Figures 2.24a, b are the images of a porous alumina membrane in which pore diameter was 20 nm and Pb nanowire arrays formed as the hydraulic force was applied. After the 20 nm Pb nanowire arrays were fabricated, a sulfization procedure was proceeded to obtain PbS nanoparticles, as shown in Fig. 2.24c. The study [115] may give rise to an alternative method of producing PbS nanostructures.

Thus, a number of chemical and physical methods for the synthesis of nanostructured lead sulfide as colloid solutions, nanoparticles, nanopowders and films have now been developed.

2.2 Crystal Structure of Nanoparticles, Nanopowders, and Nanofilms of Lead Sulfide

The bulk lead sulfide is commonly regarded as a stoichiometric compound with a negligibly narrow homogeneity $PbS_{0.9995–1.0005}$ [2]. Under a normal atmospheric pressure and room temperature, lead sulfide crystallizes in a cubic (space group $Fm\bar{3}m$) $B1$ structure with the lattice constant a = 0.59362 nm. The lead and sulfur ions occupy sites 4(a) with coordinates (0 0 0) and sites 4(b) with coordinates (1/2 1/2 1/2), respectively.

Under a pressure of 2.5 GPa, lead sulfide with the $B1$ structure acquires orthorhombic $B16$ ($B33$) structure, i.e, a phase transition of cubic $B1$ structure to orthorhombic (space group *Pnma)* structure of the GeS type takes place [2]. As the particle size decreases, the surface energy increases; therefore, pressure needed to change the crystal structure should increase. Indeed, in a PbS nanopowder, a cubic to orthorhombic phase transition starts at a higher pressure 3.0 GPa [116]. According to the data of Qadri et al. [116], the phase transition is sluggish. The smaller the grain size, the more sluggish the transition. The two phases with the $B1$ and $B16$ ($B33$) structures can coexist up to 8 GPa. As the pressure increases to 25 GPa, a second phase transition of lead sulfide to a CsCl type ($B2$) cubic structure takes place [117].

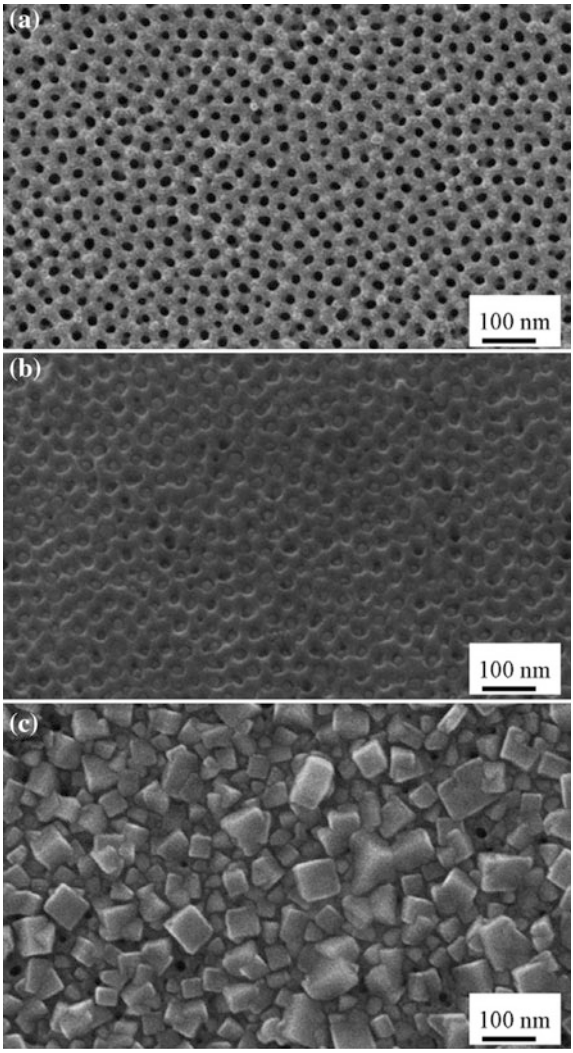

Fig. 2.24 SEM images of **a** Al_2O_3 membrane with pores of 20 nm diameter, **b** metallic lead nanofibres obtained by injection of a lead melt through membrane pores, and **c** PbS nanoparticles obtained by sulfidation of lead nanofibres with gaseous hydrogen sulfide (**c**) [115]

Recent studies showed that the decrease in the grain size of sulfides to several tens of nanometres and below, i.e, transition to the nanostructured state, is accompanied by a noticeable change in their optical properties.

The transition to the nanostate is accompanied by not only transformation of the properties of sulfides associated with size effects but also by structural changes. In particular, cadmium sulfide as single crystals or coarse-grained powders crystallize in the hexagonal wurtzite (*B*4 type) [118] or cubic sphalerite (*B*3 type) type structures [119, 120]. However, CdS thin films or nano- or ultradisperse powders have a structure different from the crystal structure of these two modifications. Recently, it was shown [121, 122] that CdS nanoparticles have a specific disordered

structure with random alternation of close-packed atomic planes; the mean lattice of this disordered structure is described by space group *P6/mmm*.

The data on the crystal structure of PbS films are also ambiguous. It is usually assumed that PbS films, like coarse-grained bulk lead sulfide, have a stoichiometric composition and a cubic (space group $Fm\bar{3}m$) *B*1 type structure. On the basis of investigating the structures of PbS films at different temperatures, Quadri et al. [123] suggested that at 375 K, subtle phase transition from the *B*1 to cubic *B*3 structure (space group $F\bar{4}3m$) takes place in the film. The phase with the *B*3 structure has nonstoichiometric composition $PbS_{0.9}$ and can coexist with the *B*1 structure. Meanwhile, it was shown [124] that the lead to sulfur ratio in PbS thin films is stoichiometric (Pb:S = 1:1). The statement of Qadri et al. [123] about the *B*3 phase is a mistake, because for interpreting the diffraction data, they suggested that some lead atoms in the detected phase occupy sites 4(*b*) with the coordinates (1/2 1/2 1/2) but there are no such sites in the *B*3 type structure, however, they exist in space group $F\bar{4}3m$. To conserve the sulfide composition, the occupancies of the 4 (*a*) and 4(*b*) positions were taken equal to 0.75 and 0.25, respectively. Thus, the structure of PbS films proposed by Quadri et al. [123] is cubic and belongs to space group $F\bar{4}3m$ but does not refer to the *B*3 type structure.

In the thin-layer heterostructures, $PbVS_3$, $PbNbS_3$ and $PbTaS_3$, which represent alternating PbS and transition metal disulfide (VS_2, NbS_2 or TaS_2) layers, lead sulfide can have monoclinic crystal structure (space groups *C*2, *C*2/*m*, *Cm*2*a*) [125–128].

Unfortunately, studies into the synthesis and properties of nanostructured PbS with different morphology usually do not include detailed investigation of the crystal structure. The conclusion about the *B*1 type cubic structure of nanostructured PbS is drawn upon visual comparison of the experimental XRD patterns with the standard data for bulk lead sulfide and comparison of the estimated unit cell constant with the unit cell constant of bulk PbS.

Thorough investigations of the crystal structure of PbS nanopowders and nanofilms [95, 96, 98–100, 129] were carried out after 2008.

2.2.1 *Crystal Structures of Nanopowders and Quantum Dots*

Nanocrystalline PbS powders with an average particle size from 100 to 8 nm were studied by X-ray diffraction [98, 99].

Nanocrystalline PbS powders with the average particle size of 20 nm and smaller were prepared by chemical condensation with the reaction between S^{2-} and Pb^{2+} ions. The synthesis of PbS nanoparticles was performed by mixing stoichiometric amounts of aqueous solutions of lead acetate $Pb(CH_3COO)_2 \equiv Pb(AcO)_2$ and sodium sulfide Na_2S.

The crystal structure and average size of the particles in nanocrystalline PbS powders was studied by XRD method. The measurements were performed by the Bragg-Brentano technique with the use of a Shimadzu XRD-7000 X-ray diffractometer with Cu$K\alpha_{1,2}$ radiation in the 2θ angle range 18°–90°, with a step of $\Delta(2\theta) = 0.03°$ and 10 s exposure at each point. The microstructure and crystal structure of PbS nanoparticles were investigated using transmission and scanning electron microscopy and electron diffraction on electron microscopes FEI Quanta_200 and JEOL JEM 200CX.

Figure 2.25 shows the XRD patterns of several finest grained PbS nanopowders with different average particle sizes from 9 to 20 nm. The observed large broadening of the diffraction reflections is associated primarily with the small size of the particles.

The set of reflections was the same for all nanopowders and, as a first approximation, it corresponded to the cubic structure with space group $Fm\bar{3}m$. The final refinement of the structure of the PbS nanopowders was performed with the X'Pert Plus software package [130]. The structure was refined using models corresponding to $B1$, $B2$, $B3$, $B16$ and $D0_3$ type structures mentioned in the literature. The best agreement between the experimental and calculated XRD patterns was achieved for the $B1$ structure.

As an example, Fig. 2.26 shows the experimental, calculated, and difference XRD patterns of the PbS nanopowder with the average particle size of 12 nm. The Rietveld reliability factors are equal to $R_I = 0.0096$, $R_p = 0.0478$, $\omega R_p = 0.0641$. The use of alternative structures such as $B2$, $B3$, $B16$ and $D0_3$ resulted in poorer agreement between the experimental and calculated XRD patterns of nanocrystalline PbS powders. The results of electron microscopy of the particles of PbS nanopowders [98, 99] are consistent with XRD data. Thus, the PbS nanopowders have a cubic (space group $Fm\bar{3}m$) $B1$ structure.

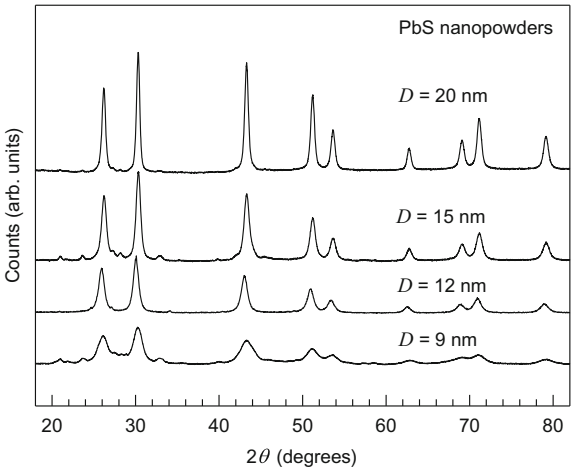

Fig. 2.25 XRD patterns of the nanocrystalline PbS powders with different average sizes D of particles [99]. All powders contain only the cubic (space group $Fm\bar{3}m$) lead sulfide with the $B1$ type structure. The large broadening of the diffraction reflections is due to the small size of PbS particles. XRD patterns are recorded in Cu$K\alpha_{1,2}$ radiation

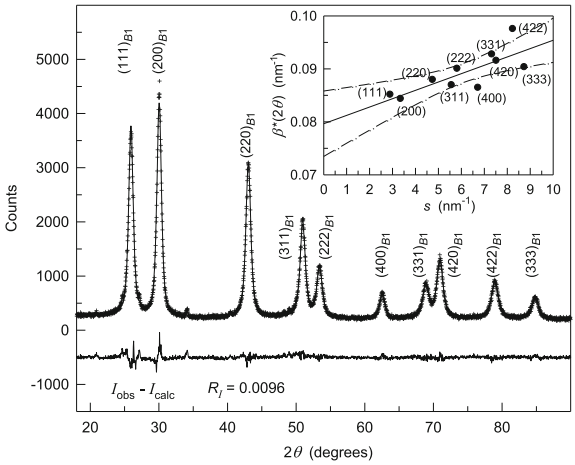

Fig. 2.26 Experimental (*crosses*) and calculated (*solid line*) XRD patterns of the nanocrystalline PbS powder with a cubic (space group $Fm\bar{3}m$) $B1$ type crystal structure [99]. The *bottom curve* shows the difference ($I_{obs} - I_{calc}$) between the experimental and calculated XRD patterns. The *inset* shows the dependence of the reduced broadening $\beta^*(2\theta)$ of diffraction reflections on the magnitude of the scattering vector s and its linear approximation. The *dot-dashed lines* indicate a 95% confidence interval of the determination of $\beta^*(2\theta)$ as a function of s. The average size of particles D is obtained by extrapolating the dependence $\beta^*(s)$ to the value of $s = 0$

Electron diffraction studies of isolated nanoparticles and lead sulfide QDs [10, 11, 58, 92] in combination with high resolution transmission electron microscopy (HRTEM) confirmed their cubic structure. However, a special quantitative refinement of the crystal structure of PbS quantum dots was never carried out; therefore, the assignment of $B1$ type structure to these objects is hypothetical. Indeed, the crystal structure of PbS nanofilms was also considered to be $B1$, but recent studies demonstrated that this opinion is erroneous.

2.2.2 *Crystal Structures of Nanofilms*

Quantitative determination of the crystal structures of nanostructured PbS films is described in studies [95, 96, 100, 129]. Synthesis of these nanostructured PbS films, their microstructure and designations are described in Sect. 2.1.6.

Lead sulfide films of ~100 nm thickness were annealed in air at temperatures from 293 to 423 K with a step of 30–40 K.

XRD examination of the films was carried out in situ on a Philips X'Pert automated diffractometer with Cu$K\alpha_{1,2}$ radiation in the 2θ angle range 18°–90°, with a step of $\Delta(2\theta) = 0.016°$ and large exposure time ~500 s in each point. The

Philips X'Pert diffractometer was equipped with a position-sensitive fast X'Celerator sector detector which is an integral device of several parallel detectors [131, 132]. Owing to this, the X'Celerator detector measures the reflection intensity in the wide range 7.2° of the 2θ angles, not in a point, as a common proportional counter-detector does. For example, if the measurement starts from 18°, at the initial moment, the detector captures the angle range 14.4°–21.6° and begins to move to a range of larger angles. By the time when the detector scans the reflection intensity in the angular range from 18.0° to 25.2°, the exposure time in the 18° point with a step of 0.016° is even 450 s. As a result, the duration of measuring the XRD of the film was decreased approximately by a factor of 100 (from 600 to 700 h as a common detector is used to 7–8 h with the X'Celerator detector) without any loss of the resolution quality.

The XRD patterns of the PbS-1 nanostructured film measured in situ at various annealing temperatures are shown in Fig. 2.27. All the observed diffraction reflections are noticeably broadened. The change in the lattice constant on heating shifts the maxima of the XRD diffraction reflections. As an example, the inset to Fig. 2.27 shows the change in the position of the (200) XRD of the film of the nanocrystalline lead sulfide as temperature increases. Thus, the lead sulfide has, at a temperature of 423 K, the lattice constant which is approximately 0.0012 nm larger than that at room temperature. An average particle size in film was estimated from the diffraction reflection broadening. The average particle size increases with

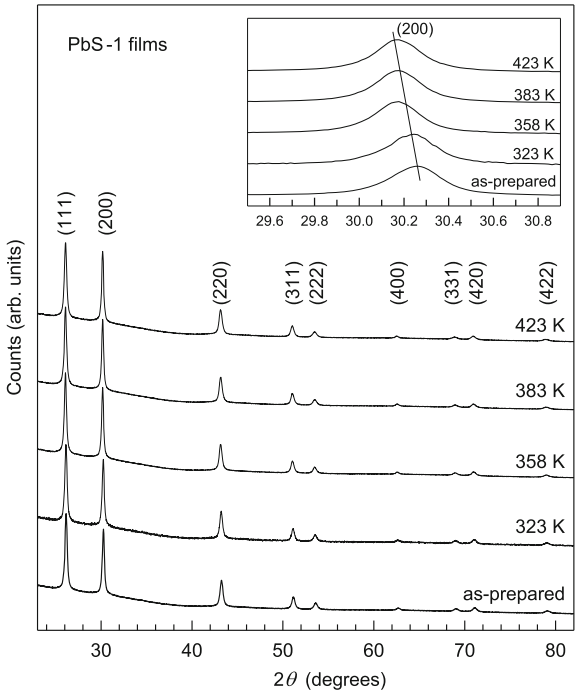

Fig. 2.27 XRD patterns of nanostructured PbS-1 film recorded in situ at different annealing temperatures. *Inset* shows a systematic displacement of the (200) diffraction reflection with increase of annealing temperature. The film are deposited onto the glass substrate, microstructure of as-prepared PbS-1 film is shown in Fig. 2.22a. The XRD patterns are recorded in Cu$K\alpha_{1,2}$ radiation. Reprinted from [100] with permission from Elsevier

temperature from 70 nm (as-prepared state at 293 K) to 175 nm at a temperature of 423 K.

Since the structural type of PbS films has not been unambiguously determined, the authors [95, 96, 100, 129] carried out quantitative analysis of the measured XRD patterns using various cubic structure models. The following crystal structure models were considered: cubic $B1$ (space group $Fm\bar{3}m$); cubic $B3$ (space group $F\bar{4}3m$); and a two-phase model of a film in which the relative contents of phases with $B1$ and $B3$ type structures are y and $(1 - y)$, respectively.

In the general case, the measured intensity of the ith structure reflection (hkl) is

$$I_i = K \cdot F_{hkl}^2 \cdot P_{hkl} \cdot PLG(\theta) \cdot f_T, \tag{2.21}$$

where K is the instrument constant, F_{hkl}^2 is the structural factor, P_{hkl} is the multiplicity factor, $PLG(\theta)$ is the angular factor of the intensity, and f_T is the temperature factor.

As the $B1$ and $B3$ type structures and the assumed intermediate structure are cubic, their coefficients K, P_{hkl}, $PLG(\theta)$ and f_T are the same at other conditions being identical, and only the factor F_{hkl}^2 is variable quantity.

The structural factor F_{hkl}^2 appearing in relationship (2.21) is the square of the structural amplitude

$$F_{hkl} = \sum_j f_j \exp[-i2\pi(x_j h + y_j k + z_j l)] \tag{2.22}$$

and, in the trigonometric form, has a general expression

$$\begin{aligned} F_{hkl}^2 = &\left[\sum_j f_j \cos[2\pi(x_j h + y_j k + z_j l)]\right]^2 \\ &+ \left[\sum_j f_j \sin[2\pi(x_j h + y_j k + z_j l)]\right]^2, \end{aligned} \tag{2.23}$$

where x_j, y_j, z_j are the coordinates of the jth atom, and f_j is the atomic scattering factor. Summation in (2.22) and (2.23) is performed over atoms of the unit cell of the crystal structure under consideration.

The unit cell basis of lead sulfide with the $B1$ structure (space group $Fm\bar{3}m$) contains eight atoms among them four Pb atoms in positions 4(a) with the coordinates (0 0 0), (1/2 1/2 0), (1/2 0 1/2), and (0 1/2 1/2), and four S atoms in positions 4(b) with the coordinates (1/2 1/2 1/2), (0 0 1/2), (0 1/2 0), and (1/2 0 0). If the atomic scattering factors of lead and sulfur atoms are f_{Pb} and f_{S}, respectively, the structural factor of the $B1$ type structure calculated by relationship (2.23) has the form

$$F_{B1}^2 = \{f_{\mathrm{Pb}}[1 + \cos\,\pi(h+k) + \cos\,\pi(h+l) + \cos\,\pi(k+l)] + f_{\mathrm{S}}[\cos\,\pi(h+k+l) + \cos\,\pi h + \cos\,\pi k + \cos\,\pi l]\}^2 \tag{2.24}$$

In the unit cell of PbS with the $B3$ structure (space group $F\bar{4}3m$), four lead atoms occupy positions 4(a) with the same coordinates which they occupy in the $B1$ structure, namely, (0 0 0), (1/2 1/2 0), (1/2 0 1/2), and (0 1/2 1/2), and four sulfur atoms occupy positions 4(c) with the coordinates (1/4 1/4 1/4), (3/4 3/4 1/4), (3/4 1/4 3/4), and (1/4 3/4 3/4). According to the foregoing, the structural factor of lead sulfide with the $B3$ structure is given by

$$\begin{aligned} F_{B3}^2 = {} & \{f_{\mathrm{Pb}}[1 + \cos\pi(h+k) + \cos\pi(h+l) + \cos\pi(k+l)] \\ & + f_{\mathrm{S}}\left[\cos\frac{\pi}{2}(h+k+l) + \cos\frac{\pi}{2}(3h+3k+l) + \cos\frac{\pi}{2}(3h+k+3l)\right. \\ & \left. + \cos\frac{\pi}{2}(3h+k+3l) + \cos\frac{\pi}{2}(h+3k+3l)\right]\Big\}^2 \\ & + f_{\mathrm{S}}^2\left[\sin\frac{\pi}{2}(h+k+l) + \sin\frac{\pi}{2}(3h+3k+l) + \sin\frac{\pi}{2}(3h+k+3l)\right. \\ & \left. + \sin\frac{\pi}{2}(h+3k+3l)\right]^2 \end{aligned} \tag{2.25}$$

If the film is two-phase and the relative content in the film of the phase with the $B1$ structure is y and the phase with the $B3$ structure is $(1 - y)$, the intensity I_i of arbitrary reflection is a superposition of the intensities of like reflections of the $B1$ and $B3$ structures. In such a two-phase film, the sulfur atoms occupy the nonmetallic positions of the $B1$ structure with the probability of y and the nonmetallic positions of the $B3$ structure with the probability $(1 - y)$. In this case, the structural factor is the superposition of the structural factors of the $B1$ and $B3$ phases and has the form

$$\begin{aligned} F_{B1+B3}^2 = {} & \{f_{\mathrm{Pb}}[1 + \cos\pi(h+k) + \cos\,\pi(h+l) + \cos\pi(k+l)] \\ & + yf_{\mathrm{S}}[\cos\,\pi(h+k+l) + \cos\,\pi h + \cos\,\pi k + \cos\,\pi l] + (1-y)f_{\mathrm{S}}\left[\cos\frac{\pi}{2}(h+k+l)\right. \\ & \left. + \cos\frac{\pi}{2}(3h+3k+l) + \cos\frac{\pi}{2}(3h+k+3l) + \cos\frac{\pi}{2}(h+3k+3l)\right]\Big\}^2 \\ & + \left\{(1-y)f_{\mathrm{S}}\left[\sin\frac{\pi}{2}(h+k+l) + \sin\frac{\pi}{2}(3h+3k+l) + \sin\frac{\pi}{2}(3h+k+3l)\right.\right. \\ & \left.\left. + \sin\frac{\pi}{2}(h+3k+3l)\right]\right\}^2 \end{aligned} \tag{2.26}$$

The determination of the phase composition and crystal lattice parameters of possible cubic phases and final refinement of the structure of the PbS film corresponding to various temperatures from 293 to 423 K were carried out using the X'Pert Plus program [130]. To estimate the validity of the structural models, authors [95, 96, 100] used the Rietveld factor of reliability [133]

$R_I = \sum_{i=1}^{N} \left|I_{\exp(i)} - I_{\text{calc}(i)}\right| \Big/ \sum_{i=1}^{N} \left|I_{\exp(i)}\right|$, where $I_{\exp(i)}$ and $I_{\text{calc}(i)}$ are the experimental and calculated intensities of the ith reflection, respectively. The minimization of the experimental XRD patterns in an approximation of two-phase film gives $y = 0.90 \pm 0.02$ and a better convergence $R_{I(B1+B3)} = 0.04$ than the minimization in an approximation in which the film contains the only phase with either the $B1$ or $B3$ structure ($R_{I(B1)} = 0.05$ и $R_{I(B3)} = 0.12$, respectively). Along with this, it follows from the minimization that the lattice constants of the phases with the $B1$ and $B3$ structures are absolutely equal. Physically, this is unlikely and indicates that the PbS film is single-phase, but its structure is similar to the $B1$ and $B3$ structures but it differs from them.

Sadovnikov, Gusev and Rempel [95] assumed that the real structure of PbS films corresponds to space group $Fm\overline{3}m$ but the S atoms in it occupy not only octahedral (sites 4(b)) but also tetrahedral interstices (sites 8(c)) (Fig. 2.28b). In this structure, the probabilities for S atoms to occupy sites 4(b) and 8(c) are equal to y and $(1 - y)/2$, respectively. The 8(c) positions of the cubic crystal lattice with space group $Fm\overline{3}m$ have the following coordinates: (1/4 1/4 1/4), (3/4 3/4 1/4), (3/4 ¼ 3/4), (1/4 3/4 3/4), (3/4 3/4 3/4), (3/4 1/4 1/4), (1/4 3/4 1/4), and (1/4 1/4 3/4).

Taking into account the coordinates of the 4(a) positions occupied with Pb atoms and the 4(b) and 8(c) positions occupied with S atoms with the probabilities y and $(1 - y)/2$, respectively, the structure amplitude of the proposed cubic (space group $Fm\overline{3}m$) phase has the form

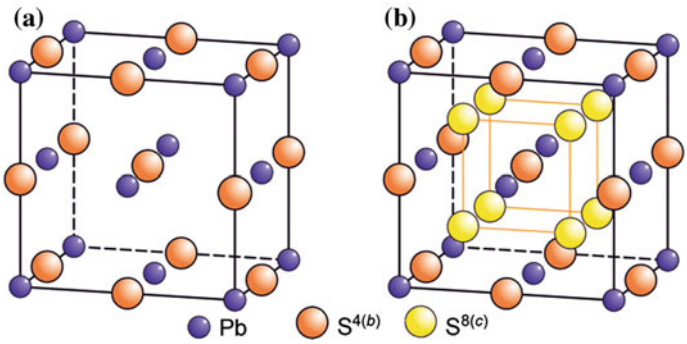

Fig. 2.28 Crystal structures of PbS. **a** Unit cell of coarse-grained bulk cubic (space group $Fm\overline{3}m$) lead sulfide with $B1$ type structure; **b** distribution of lead and sulfur atoms in the unit cell of cubic (space group $Fm\overline{3}m$) $D0_3$-type structure of a $PbS{\equiv}PbS_y^{4(b)}S_{1-y}^{8(c)}$ nanofilm. *Filled violet circle* atoms Pb в in 4(a) positions; *Filled orange (dark) circle* atoms S in 4(b) positions; *Filled yellow (light) circle* atoms S in 8(c) positions. In the unit cell of the $D0_3$-type structure, sulfur atoms randomly occupy, with probability y, octahedral sites 4(b) and randomly occupy, with probability $(1 - y)$, tetrahedral sites 8(c)

$$
\begin{aligned}
F = {} & f_{Pb}\{1+\exp[-i\pi(h+k)]+\exp[-i\pi(h+l)]+\exp[-i\pi(k+l)]\} \\
& + yf_S\{\exp[-i\pi(h+k+l)]+\exp(-i\pi h)+\exp(-i\pi k)+\exp(-i\pi l)]\} \\
& + [(1-y)f_S/2]\{\exp[-i\pi(h+k+l)/2]+\exp[-i\pi(3h+3k+l)/2] \\
& + \exp[-i\pi(3h+k+3l)/2]+\exp[-i\pi(h+3k+3l)/2] \\
& + \exp[-i\pi(3h+3k+3l)/2]+\exp[-i\pi(h+k+3l)/2] \\
& + \exp[-i\pi(h+3k+l)/2]+\exp[-i\pi(3h+k+l)/2]\}.
\end{aligned}
\tag{2.27}
$$

With the known structure amplitude (2.27), we can easily obtain the structural factor F^2 of the cubic (space group $Fm\bar{3}m$) phase of the PbS film

$$
\begin{aligned}
F^2 = {} & \{f_{\mathrm{Pb}}[1+\cos\pi(h+k)+\cos\pi(h+l)+\cos\pi(k+l)] \\
& + yf_{\mathrm{S}}[\cos\pi(h+k+l)+\cos\pi h+\cos\pi k+\cos\pi l] \\
& + \frac{1-y}{2}f_{\mathrm{S}}\Big[\cos\frac{\pi}{2}(h+k+l)+\cos\frac{\pi}{2}(3h+3k+l)+\cos\frac{\pi}{2}(3h+k+3l) \\
& + \cos\frac{\pi}{2}(h+3k+3+\cos\frac{\pi}{2}(3h+3k+3l)+\cos\frac{\pi}{2}(3h+k+l) \\
& + \cos\frac{\pi}{2}(h+3k+l)+\cos\frac{\pi}{2}(h+k+3l)\Big]\Big\}^2 \\
& + \Big\{\frac{1-y}{2}f_{\mathrm{S}}\Big[\sin\frac{\pi}{2}(h+k+l)+\sin\frac{\pi}{2}(3h+3k+l)+\sin\frac{\pi}{2}(3h+k+3l) \\
& + \sin\frac{\pi}{2}(h+3k+3l)+\sin\frac{\pi}{2}(3h+3k+3l)+\sin\frac{\pi}{2}(3h+k+l) \\
& + \sin\frac{\pi}{2}(h+3k+3l)+\sin\frac{\pi}{2}(h+k+3l)\Big]\Big\}^2
\end{aligned}
\tag{2.28}
$$

Figure 2.29 shows, as an example, the experimental XRD pattern of the PbS-1 film measured in situ at temperatures of 293 K, and the XRD pattern calculated in the approximation of the new cubic structure of the film, in which sulfur atoms are placed not only in the octahedral positions 4(*b*), but also in the tetrahedral positions 8(*c*).

Minimization of the experimental XRD patterns of PbS films demonstrated that at any temperature from 293 to 423 K, sites 4(*b*) and 8(*c*) are occupied by sulfur atoms with the probabilities of $\sim$0.84 and $\sim$0.08 (Table 2.5).

The reliability factor R_I for all XRD patterns did not exceed 0.017. Thus, the crystal lattice of PbS films is characterized by a latent nonstoichiometric distribution of sulfur atoms among sites 4(*b*) and 8(*c*). The new cubic structure (space group $Fm\bar{3}m$) found in the lead sulfide nanofilms corresponds to the $D0_3$ structural type with partially disordered (random) distribution of sulfur atoms over the sites of two types (see Fig. 2.28b). Considering the crystal structure of nanofilms and the

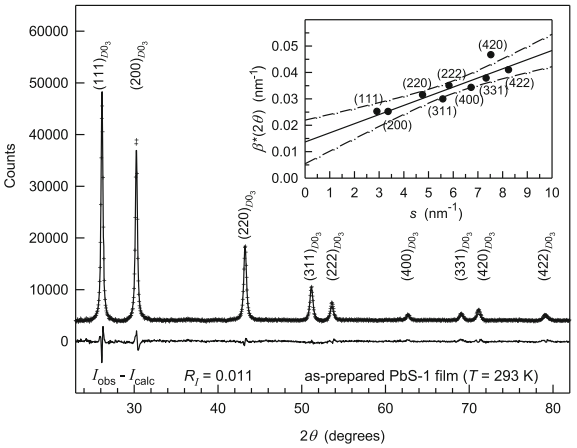

Fig. 2.29 Experimental (*crosses*) and calculated (*solid line*) XRD patterns of the as-prepared nanostructured PbS-1 film with a cubic (space group $Fm\bar{3}m$) $D0_3$-type crystal structure (each third experimental point is shown only) [100]. The *bottom curve* shows the difference ($I_{obs} - I_{calc}$) between the experimental and calculated XRD patterns

Table 2.5 Cubic (space group $Fm\bar{3}m$) $D0_3$ type structure of nanostructured PbS films [95, 100]: a = 0.59395 nm

Atom	Position and multiplicity	Atomic coordinates			Occupancy
		x/a	*y/a*	*z/a*	
Pb	4(*a*)	0	0	0	1
S 1	4(*b*)	0.5	0.5	0.5	0.84
S 2	8(*c*)	0.25	0.25	0.25	0.08

occupancies of sites 4(*b*) and 8(*c*), the formula of the lead sulfide can be written as $PbS^{4(b)}_{0.84}S^{8(c)}_{0.16} \equiv Pb(S_{0.84}\square_{0.16})^{4(b)}(S_{0.16}\square_{0.84})^{8(c)}$, where □ is a structural vacancy.

Previously, there was no experimental evidence for the occupation of tetrahedral sites in cubic sulfides by sulfur atoms, and the "latent" nonstoichiometry of lead sulfide was found for the first time in the studies considered above [95, 100, 129].

In the cubic structure (space group $Fm\bar{3}m$) of PbS, the radii of the octahedral and tetrahedral interstices are equal $r_{octa} = a/2 - r_{Pb^{2+}}$ and $r_{tetra} = a\sqrt{3}/4 - r_{Pb^{2+}}$, respectively.

The lattice constant a of the PbS films is 0.5940 nm, and the radii of the Pb^{2+} and S^{2-} ions are 0.121 and 0.184 nm, respectively. Therefore, the radii of the octahedral and tetrahedral interstices are ~0.176 and ~0.136 nm, respectively. Since $r_{S^{2-}} > r_{tetra}$, the location of the S^{2-} anion in the tetrahedral interstice would result in considerable displacements of the nearest lead atoms, which was actually observed in experiments: the microstrains in the films were 0.20–0.30% at any annealing temperatures up to 423 K.

The occupation of sites 4(*b*) and 8(*c*) by sulfur atoms with the probabilities of ~0.84 and ~0.08, respectively, implies that out of every twelve octahedral interstices, approximately ten are occupied by sulfur atoms and two are vacant.

The cubic structure with space group $Fm\bar{3}m$ has twice more tetrahedral interstices than octahedral ones. Therefore, there are 24 tetrahedral interstices per 12 octahedral ones; of these, two are occupied by sulfur atoms and the other are vacant. The absence of superstructural reflections means that the arrangement of sulfur atoms in each type of sites is disordered (random). This is illustrated in Fig. 2.30, which shows the model of the cubic structure of a PbS film in comparison with the *B*1 structure. The arrangement of some sulfur atoms in tetrahedral interstices entails some increase in the lattice constant in comparison with the lattice constant of lead sulfide with the *B*1 structure and gives rise to microstrains. As can be seen in Fig. 2.30, when a sulfur atom occupies a tetrahedral interstice, at least one neighbouring octahedral interstice is vacant, i.e, the crystal lattice of the cubic phase in question has some short-range order.

Sadovnikov and Rempel [134] studied the distribution of the sulfur atoms and vacancies in the square (001) and hexagonal (111) planes formed by sites 4(*b*) and 8

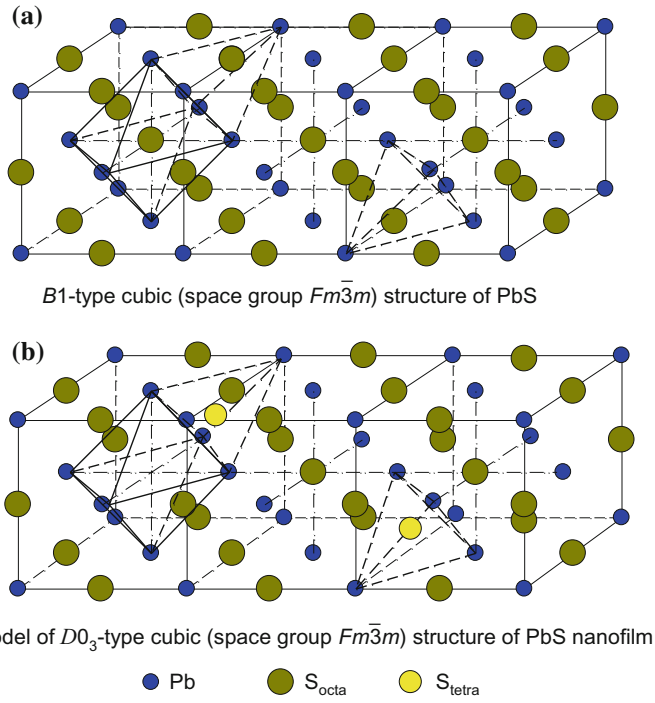

Fig. 2.30 **a** Cubic (space group $Fm\bar{3}m$) *B*1 type structure of lead sulfide and **b** model of the cubic (space group $Fm\bar{3}m$) $D0_3$ type structure of a PbS nanofilm with random distribution of sulfur atoms in the octahedral and tetrahedral interstices [95, 100]

(*c*) in the nonmetal sublattice of the nanocrystalline PbS films with cubic $D0_3$ structure and latent nonstoichiometry.

2.2.3 *Correlations of Sulfur Atoms S in PbS Nanostructured Films*

In studies [95, 96, 100, 129], it was demonstrated that PbS nanostructured films with nanoparticle sizes less than 80 nm have a cubic (space group $Fm\bar{3}m$) structure with a disordered arrangement of sulfur atoms S not only in octahedral positions 4 (*b*) but also in tetrahedral positions 8(*c*) (see Sect. 2.2.2). The newly revealed structure of PbS nanostructured films belongs to the $D0_3$ structure type. In this structure, the nonmetal lattice is separated into two nonmetal sublattices, one of which is formed by sites occupying the 4(*b*) crystallographic positions and the other sublattice is formed by sites occupying the 8(*c*) crystallographic positions.

In the case of chemical deposition of PbS films from aqueous solutions, films with different crystallographic orientations can be formed on the substrate surface. For the cubic $D0_3$ structure, the formation of PbS nanofilms corresponding to the (001) and (111) planes or equivalent to them is most probable. In the (001) planes, the 8(*c*) sites of the nonmetal sublattice form a planar square (plane group *p*4*mm*) Kepler net of the 4^4 type (Fig. 2.31a), and, in the (111) plane, the 4(*b*) sites of the nonmetal sublattice form a planar hexagonal (plane group *p*6*mm*) net of the 3^6 type (Fig. 2.31b) [134]. In the revealed structure of PbS nanofilms [95, 100], the S atoms occupy the octahedral sites 4(*b*) and tetrahedral sites 8(*c*) of the nonmetal sublattice with the probabilities $P_{\text{S-octa}} = 0.84$ and $P_{\text{S-tetra}} = 0.08$, respectively. This means that the nonmetal lattice of the PbS nanofilm with the $D0_3$ structure is characterized by a latent nonstoichiometry [129]. Therefore, in the (001) and (111) nonmetal planes of the lead sulfide nanofilm, a number of sites are occupied by S atoms and the other sites are vacant (Fig. 2.31). In planar square (Fig. 2.31c) and hexagonal (Fig. 2.31d) lattices, S atoms and vacant sites □ form an $S_y\square_{1-y}$ substitutional solid solution. Nonequivalent configurations of figures (site, bond, and square cluster) used for describing the $S_y\square_{1-y}$ solid solution with planar square lattice are shown in Fig. 2.31e. Nonequivalent configurations of figures (site, bond, and triangular cluster) used for describing the $S_y\square_{1-y}$ solid solution with planar hexagonal lattice are shown in Fig. 2.31f. With allowance made for the results obtained in works [95, 96, 100, 129], the difference between the properties of PbS nanostructured films and coarse-grained (bulk) lead sulfide can be caused, with an equal probability, by the

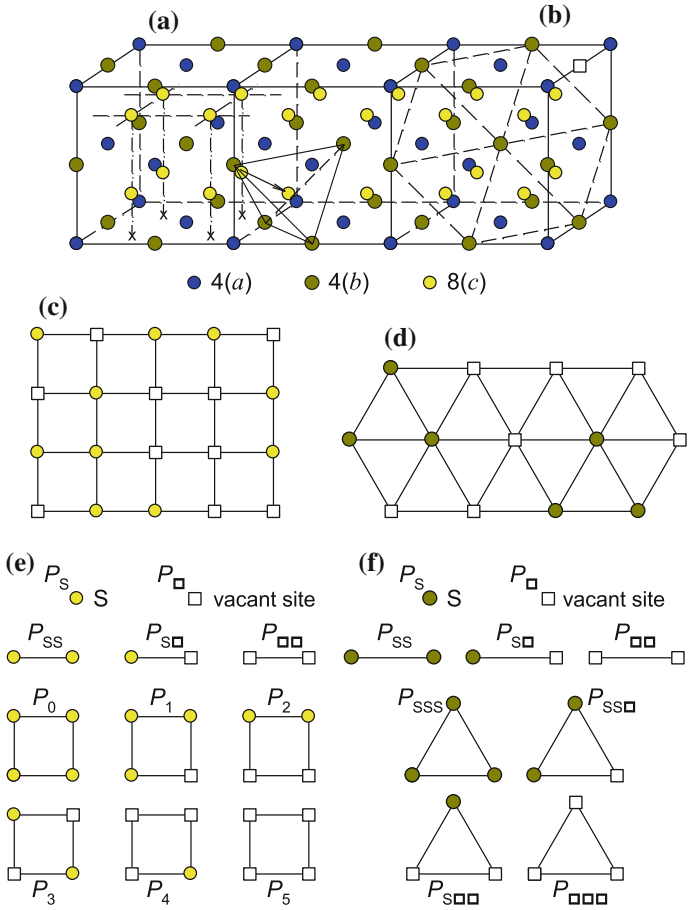

Fig. 2.31 Positions of nonmetal **a** square (001) and **b** hexagonal (111) planes in the unit cell of the cubic (space group $Fm\bar{3}m$) $D0_3$ structure of a lead sulfide nanostructured film, and **c** square (plane group $p4mm$) and **d** hexagonal (plane group $p6mm$) lattices simulating these planes [134]. The (001) and (111) nonmetal planes pass through the 8(c) and 4(b) sites, respectively. In the square and hexagonal lattices, sulfur atoms S and vacant sites □ form an $S_y□_{1-y}$ substitutional solid solution. Nonequivalent configurations (**e** and **f**) of figures (site, bond, square and triangular clusters) used for describing the $S_y□_{1-y}$ solid solution with planar square and hexagonal lattices are shown at the bottom

size effects and also the change in the structure and specific features in the mutual arrangement of atoms S and vacancies □ in defect nonmetal planes (001) and (111).

The distribution of atoms of different types (or atoms and structural vacancies) in a crystal is characterized by the long- and short-range orders [135]. Authors [95, 96, 100, 129] did not reveal superstructure reflections in the XRD patterns of lead sulfide nanofilms with the $D0_3$ structure, which indicates the absence of ordering in the nonmetal lattice. However, the possible presence of correlations (short-range

order) in the mutual arrangement of sulfur atoms S and vacancies □ was not ruled out. Therefore, the structure and properties of lead sulfide nanofilms should be described taking into account the short-range order. This is especially important because the relative number of vacancies in each nonmetal sublattice is large and sufficient for the appearance of correlations between sulfur atoms S and vacancies □.

The radius r_{tetra} of the tetrahedral interstitial site 8(*c*) is smaller than the radius $r_{S^{2-}}$ of the S^{2-} ion. Since $r_{S^{2-}} > r_{\text{tetra}}$, the transition of the S atom from the 4(*b*) site to the 8(*c*) site leads to local displacements of the nearest Pb atoms from the 8 (*c*) site occupied by the S atom. This results in the appearance of microstrains in the PbS nanofilm: their value at room temperature is approximately equal to 0.20% [95, 96, 100, 129]. In the PbS sulfide with the $D0_3$ structure, any 8(*c*) site is a center of the tetrahedral interstitial site formed by Pb atoms occupying nearest 4(*a*) sites, on the one hand, and is a center of tetrahedral interstitial site of the four nearest 4 (*b*) sites of the nonmetal lattice, on the other hand (Fig. 2.32).

Let us evaluate the possibility of transferring the S atom from the 4(*b*) site to the 8(*c*) site. This transition leads to the formation of a pair consisting of a vacancy in the (111) nonmetal plane and a sulfur atom in the (001) nonmetal plane (see Fig. 2.32), i.e., to the appearance of a vacancy in one of the four nearest sites 4(*b*). This additionally increases the size of the tetrahedral interstitial site. However, the (111) nonmetal planes already contain vacant sites and their relative concentration is $(1 - P_{\text{S-octa}}) \approx 0.16$. Therefore, in the environment of the S atom located in the (001) nonmetal plane and occupying the 8(*c*) tetrahedral interstitial site, the tetrahedron will be formed in two adjacent planes (111). Two sites of this tetrahedron are occupied by S atoms and two sites are vacant.

In the case of a disordered arrangement of sulfur atoms and vacancies over the 4 (*b*) sites, the probability of the formation of a tetrahedron formed by four neighboring sites 4(*b*) has the form

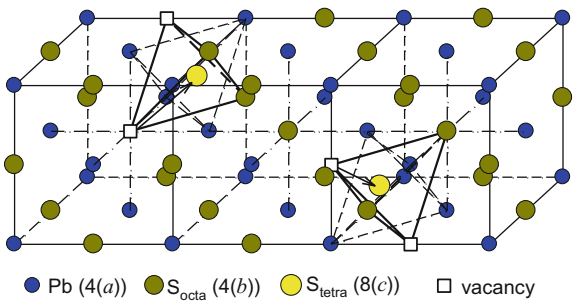

Fig. 2.32 Model of the cubic (space group $Fm\bar{3}m$) $D0_3$ structure of a PbS nanofilm with a statistical distribution of sulfur atoms S with probabilities of 0.84 and 0.08 over the octahedral and tetrahedral sites 4(*b*) and 8(*c*). *Arrows* indicate possible transitions of S atoms from the 4(*b*) sites to the 8(*c*) sites. *Solid lines* represent tetrahedral clusters formed by the 4(*b*) sites of the nonmetal lattice. *Dashed lines* show tetrahedral clusters formed by the 4(*a*) sites of the metal lattice, i.e., by Pb atoms

$$\lambda_i P_i \equiv C_4^{n_i} P_i = C_4^{n_i} P_{\text{S}-\text{octa}}^{4-n_i} (1 - P_{\text{S}-\text{octa}})^{n_i}, \tag{2.29}$$

where n_i is the number of vacancies in the i-configuration of the tetrahedron, λ_i is the multiplicity of the i-configuration (the number of configurations coinciding with each other after application of symmetry operations), and $P_{\text{S-octa}}$ is the probability of the occupation of the 4(b) octahedral positions by S atoms (in the case under consideration, $P_{\text{S-octa}} = 0.84$). The total number of nonequivalent configurations is equal to five: the tetrahedron P_{SSSS} with all sites occupied by S atoms; tetrahedra $P_{\text{SSS}\square}$, $P_{\text{SS}\square\square}$, and $P_{\text{S}\square\square\square}$ containing one, two, and three vacant sites, respectively; and tetrahedron $P_{\square\square\square\square}$, in which all sites are vacant.

The occupation of the octahedral and tetrahedral positions 4(b) and 8(c) with the probabilities $P_{\text{S-octa}} = 0.84$ and $P_{\text{S-tetra}} = 0.08$ means that, among every twelve octahedral interstitial sites, ten sites are occupied by S atoms and two sites are vacant. With due regard for the probability $P_{\text{S-octa}}$ and relationship (2.29), the probability of the formation of a tetrahedral cluster containing two vacant sites is $P_{\text{SS}\square\square} = C_4^2 P_{\text{S}-\text{octa}}^2 (1 - P_{\text{S}-\text{octa}})^2 = 0.108$. Since $P_{\text{SS}\square\square} > P_{\text{S-tetra}}$, the transition of sulfur atoms to the 8(c) tetrahedral interstitial sites with occupancies of ~ 0.08 is mathematically quite probable.

The short-range order describes the distribution of atoms around some lattice site and, specifically, determines existing two-particle atomic or atom–vacancy correlations in a particular coordination sphere [135]. The short-range order is characterized by the short-range order parameters α_j and the correlation parameters ε_j in the jth coordination sphere.

Up to now, it has not been revealed how many coordination spheres are covered by the short-range order appeared in the first coordination sphere. In study [134], this problem was solved using the computer simulation of the dependence of the correlation parameters in the jth coordination spheres ($j \geq 2$) on the correlation parameter ε_1 of the first coordination sphere. The object of the simulation was a $\text{S}_y\square_{1-y}$ substitutional solid solution with atoms located in sites of defect planar square and hexagonal lattices: a number of sites are occupied by sulfur atoms, and the other sites are vacant. Sulfur atoms S and vacancies $\square$ are mutually substituted elements of the solid solution.

The pair correlation parameter ε_j is defined as the difference between the probability of the occurrence of a pair bond formed by like elements in the jth coordination sphere of the crystal lattice with a short-range order and the probability of the occurrence of the same bond in a disordered lattice. In an infinite disordered lattice, the probability of the occurrence of pair bonds is governed by the binomial distribution [135]. As a result, we have

$$\varepsilon_{\text{SS}}(R_j) = P_{\text{SS}}^{(j)} - P_{\text{SS}}^{\text{dis}} = P_{\text{SS}}^{(j)} - P_{\text{SS}}^{\text{bin}} = P_{\text{SS}}^{(j)} - y^2, \tag{2.30}$$

$$\varepsilon_{\square\square}(R_j) = P_{\square\square}^{(j)} - P_{\square\square}^{\text{dis}} = P_{\square\square}^{(j)} - P_{\square\square}^{\text{bin}} = P_{\square\square}^{(j)} - (1 - y)^2, \tag{2.31}$$

where $P_{SS}^{(j)}$ and $P_{\square\square}^{(j)}$ are the probabilities of the occurrence of like pair bonds in the lattice with the short-range order. In the infinite disordered lattice, these probabilities are as follows: $P_{SS}^{bin} = y^2$ and $P_{\square\square}^{bin} = (1 - y)^2$. According to [135], in the presence only of a short-range order, the probabilities of the occurrence of pair bonds are given by the relationships

$$P_{SS}^{(j)} = P_{SS}^{bin} + y(1-y)\alpha_j = y^2 + y(1-y)\alpha_j, \tag{2.32a}$$

$$P_{\square\square}^{(j)} = P_{\square\square}^{bin} + y(1-y)\alpha_j = (1-y)^2 + y(1-y)\alpha_j, \tag{2.32b}$$

$$P_{S\square}^{(j)} = (1-\alpha_j)P_{S\square}^{bin} = (1-\alpha_j)y(1-y), \tag{2.32c}$$

where α_j is the short-range order parameter in the jth coordination sphere.

It follows from relationships (2.30)–(2.32) that, in the absence of a long-range order, the correlations between sulfur atoms (or vacancies) are equal to each other; that is,

$$\varepsilon_{SS}(R_j) \equiv \varepsilon_{\square\square}(R_j) \equiv \varepsilon_j = y(1-y)\alpha_j. \tag{2.33}$$

The parameters of unlike pair correlation of sulfur atoms and vacancies are equal in magnitude to the pair correlation parameters of sulfur atoms (vacancies) but opposite in sign: $\varepsilon_{S\square}(R_j) \equiv \varepsilon_{S\square}(R_j) \equiv -\varepsilon_j$. In the case of a disordered distribution of atoms in an infinite lattice, the correlation parameter is exactly equal to zero. In study [134], all probabilities were calculated for the finite lattice model without long-range order. In this case, the probabilities of the occurrence of bonds in the disordered lattice are close to the binominal probabilities $P_{SS}^{bin} = y^2$ and $P_{\square\square}^{bin}$. $= (1 - y)^2$ but are not equal to them due to the limited size of the lattice and the contribution of bonds lying at the boundary of the two-dimensional crystal.

The probabilities of the occurrence of the pair bonds S–S, S–□, and □–□ in the $S_y\square_{1-y}$ solid solution with the atoms located at the sites of the square and hexagonal lattice were calculated for nine coordination spheres. This is enough to judge the influence of the short-range order in the first coordination sphere on the pair correlation parameters in distant coordination spheres and a decrease in the short-range order parameters with an increase in the radius R_j of the coordination sphere. Furthermore, the simulation showed that the correlations in the 9th and 10th coordination spheres decrease to values comparable to the error in the calculations and almost decay.

In the disordered infinite lattice, the correlation parameter ε_j in all coordination spheres is exactly equal to zero. In the case of the short-range order when the nearest coordination sphere of the S atom predominantly contains vacancies □, the correlation parameter ε_1 is negative. For the short-range decomposition, when the environment of the S atom predominantly involves S atoms (or the environment of the vacancy □ predominantly contains vacancies), the correlation is positive, i.e., $\varepsilon_j > 0$.

In order to reveal the dependences between the correlation parameters in different coordination spheres, authors [134] considered two-dimensional square and hexagonal lattices of fixed size with a specified vacancy content. The calculations were performed for 23 × 23 and 32 × 32 square lattices containing 529 and 1024 sites, respectively, and for 33 × 33 hexagonal lattice containing 1089 sites. Some number of sites was filled with atoms, and the other sites were vacant. In the simulation, the boundaries of the solid solution lattice were assumed to be perfectly rigid. As a consequence, the lattice boundaries were fixed in the space and the number of atoms and vacancies in the lattice always remained unchanged.

At the first stage of the simulation of the lattice with a specified size, the computer synthesis of an $S_y\square_{1-y}$ disordered solid solution with a given quantity y, i.e., with the known number of atoms and vacancies, was performed. The composition of the $S_y\square_{1-y}$ solid solution was determined by the number n of sulfur atoms in the crystal lattice containing N sites. In this case, the probability of the occupation of a site in the infinite disordered crystal lattice by an atom is equal to $y = n/N$ and the relative number of vacancies is defined as $(1 - y)$. The composition was varied from 0.1 to 0.9 with a step of 0.1. The synthesis of the disordered solution was carried out after the choice of the lattice size and the solution composition. The number of sulfur atoms necessary for providing the specified composition $S_y\square_{1-y}$ was introduced into the lattice with the use of a random-number generator. As a result of statistical occupation of sites, the atoms and vacancies were distributed in the lattice in a disordered manner. The disordered state of the synthesized solution was initial state for the subsequent simulation.

In the simulation of the solid solution with the hexagonal lattice, there arises a problem associated with the fractional irrational coordinates of sites in the rectangular coordinate system. The fractional atomic coordinates lead to the error in the determination of interatomic distances. In the description of correlations in distant coordination spheres, when the increment of the radius upon changing over from the nth coordination sphere to the $(n + 1)$th coordination sphere is equal to a relatively small value comparable to the error in the atomic arrangement, there arises a probability that the site belonging to the nth coordination sphere appears to be in the $(n + 1)$th coordination sphere. In order to exclude this error, the hexagonal lattice was simulated using a special algorithm for transforming the coordinates of the sites of the hexagonal lattice into the coordinates of a hypothetical square lattice, which was described in work [136].

Then, we carried out correlation walks of atoms over the lattice sites. For this purpose, energy fluctuations were introduced into arbitrarily chosen sites, as a result of which the atom can pass to vacant sites. Only energy fluctuations sufficient for the "jump" of the atom from its site of the crystal lattice into the neighboring vacant site were taken into account.

The virtual annealing was performed after the synthesis of the disordered lattice. An arbitrary lattice site was chosen using the Monte Carlo method. The probability of choice of an occupied or vacant site depends directly on the solid solution composition. The annealing process involved displacements of atoms depending on the initial value of the correlation parameter ε_1 in the first coordination sphere. If the site was occupied by the atom, it diffused to the neighboring vacant site. The

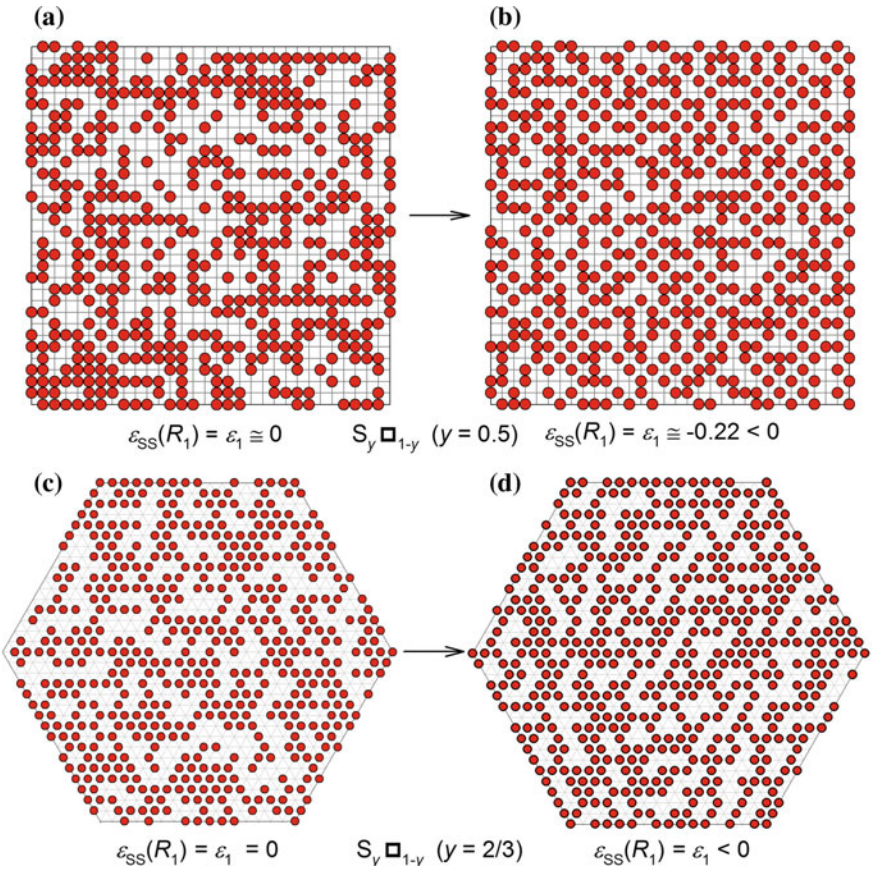

Fig. 2.33 Model distributions of sulfur atoms in **a**, **b** the square (plane group *p*4*mm*) lattice of the $S_y\square_{1-y}$ ($y = 0.5$) solid solution and **c**, **d** the hexagonal (plane group *p*6*mm*) lattice of the $S_y\square_{1-y}$ ($y = 0.66$) solid solution [134]. **a**, **c** disordered solid solutions. **b**, **d** short-range order formed after virtual annealing of the solid solution at a negative pair correlation parameter $\varepsilon_1 < 0$ in the first coordination sphere

direction of the displacement was stochastically chosen using a random-number generator. Therefore, the probabilities of atomic displacements to each side of the simulated lattice were equal to each other.

The calculations showed that there are two radically different processes: the decomposition of the $S_y\square_{1-y}$ solid solution when the pair correlation parameter ε_1 in the first coordination shell is positive ($\varepsilon_1 > 0$) and ordering at $\varepsilon_1 < 0$ (Fig. 2.33).

Figure 2.34 shows the variation in the pair correlation parameters ε_j as a function of the relative radius R_j/a_{sq} or R_j/a_{hex} of the *j*th coordination sphere for the $S_y\square_{1-y}$ solid solutions with the square and hexagonal lattices. It can be seen from Fig. 2.34 that the correlations occurring in the first coordination sphere of the $S_y\square_{1-y}$ ($y = 1/2$) solid solution with the square lattice or the $S_y\square_{1-y}$ ($y = 1/3$) solid solution

with the hexagonal lattice propagate (gradually decaying) up to the 9th coordination sphere; i.e., they extend over a distance no shorter than $4a_{sq}$ or $4a_{hex}$, where a_{sq} and a_{hex} are the lattice constants of these lattices. For the cubic $D0_3$ structure of the lead sulfide, these lattice constants are as follows: $a_{sq} = a_{cub}/2$ and $a_{hex} = (\sqrt{2}/2)a_{cub}$, where a_{cub} is the lattice constant of the cubic (space group $Fm\bar{3}m$) lead sulfide. In the case of the short-range order, the correlation parameters ε_j oscillate, change sign, and asymptotically tend to zero in magnitude: at $\varepsilon_{SS}(R_1) \equiv \varepsilon_1 < 0$, we have $|\varepsilon_j| \to 0$ при $j \to \infty$. For the short-range decomposition at $\varepsilon_{SS}(R_1) \equiv \varepsilon_1 > 0$, the correlation parameters ε_j are positive in all coordination spheres, decrease with an increase in the radius of the coordination sphere, and tend to zero.

The simulation of correlations in the mutual arrangement of sulfur atoms with due regard only for the nearest pair interactions has revealed that these interactions lead to correlations in distant coordination spheres of the square planes (001) and hexagonal planes (111). These correlations decay only at the coordination sphere radius equal to $4a_{sq}$ or $4a_{hex}$. Moreover, the results of the simulation [134] have demonstrated that, in the hexagonal planes (111), the pair correlations result in the appearance of three-particle correlations.

2.3 Properties of Nanostructured Lead Sulfide

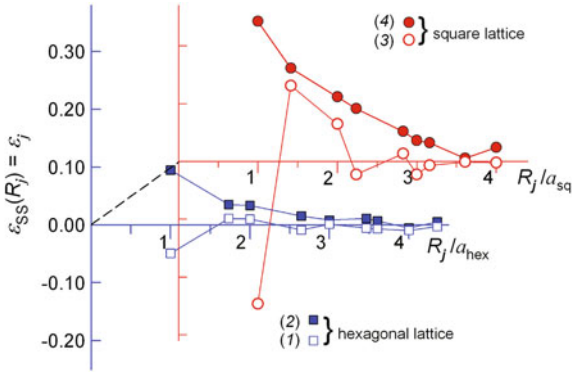

Fig. 2.34 Variation in the pair correlation parameters ε_j as a function of the relative radius of the jth coordination sphere [134]. Parameters ε_j for the $S_{1/3}\square_{2/3}$ ($y = 0.33$) solid solution with the hexagonal lattice for (*1*) the short-range order with $\varepsilon_1 < 0$ and (*2*) the short-range decomposition with $\varepsilon_1 > 0$. Parameters ε_j for the $S_{0.5}\square_{0.5}$ ($y = 0.5$) solid solution with the square lattice for (*3*) the short-range order with $\varepsilon_1 < 0$ and (*4*) the short-range decomposition with $\varepsilon_1 > 0$. Designations a_{hex} and a_{sq} are the lattice constants of the hexagonal and square lattices, respectively

Lead sulfide is used in fire alarm sensors and flame sensors, IR detectors and heat source detection systems, photodetectors operating in the range from infrared to ultraviolet, converters of solar energy to electrical energy and other thermoelectric transducers and optical switches. These applications are dependent on the optical and thermal properties of lead sulfide. These properties are considered below.

2.3.1 Optical Properties and Band Gap

Of most interest are the properties of nanostructured lead sulfide related to the band gap. There are quite a few publications on determination of the band gap of PbS as isolated nanoparticles and films.

The first measurements of light transmission and reflection and studies of the absorption edge for PbS films were carried out in the period from 1948 to the 1970s. According to the results of these studies, which were surveyed in a number of publications [4, 137–139], at a temperature of 300 K, the direct band gaps in the single crystalline PbS and in polycrystalline PbS films are 0.41 and 0.42 eV, respectively.

Light scattering and absorption by nanoparticles have specific features and differ from those of coarse-grained materials. For this reason, investigations of size effects in the optical and luminescent properties of semiconductors have attracted considerable attention in recent years.

Electronic excitation of semiconductor crystals gives rise to loosely bound electron-hole pair – an exciton. The exciton delocalization area can be much larger than the crystal lattice constant of the semiconductor; therefore, the decrease in the semiconductor crystal size to a value comparable with the exciton radius affects the properties of the crystal [79–82, 140]. For example, as the PbS particle size decreases to 5 nm, the band gap in the electronic spectrum can increase from 0.41 to 1.92 eV [53, 141] or to 2.30 eV [142]. For films based on PbS nanoparticles, the band gap can increase to 2.81 eV [143]. A decrease in the semiconductor particle size should be accompanied by a shift of the absorption band to higher frequency, i.e., so-called blue shift [144, 145]. In the case of lead sulfide films, blue shift of the absorption band is observed at a film thickness less than 150 nm [146–148].

The recombination of charges generated under the action of light (photons with energy exceeding the band gap) gives rise to luminescence. A blue shift following a decrease in the particle size was also found in the luminescence spectra of PbS nanoparticles [115, 143, 149, 150].

Systematic investigations of optical transmission of PbS nanofilms have been reported [97, 100, 151]. The optical transmission spectra were measured for PbS-1, PbS-2, PbS-3 and PbS-4 films and for the PbS-1 film annealed at temperatures of 473 and 523 K. Microstructure of these films are shown in Fig. 2.22.

The particle size distributions (Fig. 2.35) for the PbS films studied are determined from SEM-images with the use of the Altami Studio 2.0.0 software package. Unimodal distribution is observed only in the as-prepared PbS-1 film: the peak of

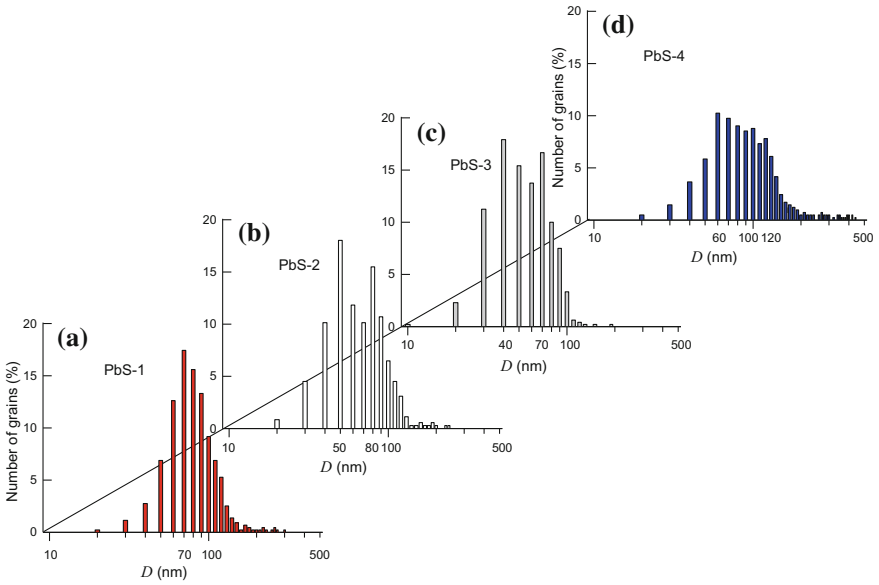

Fig. 2.35 Particle size distributions in the lead sulfide films [97, 100]: **a** In the as-prepared PbS-1 film, about 50% particles are from 60 to 80 nm in size. **b** The PbS-2 film has a bimodal size distribution of nanoparticles with peaks at 50 and 80 nm. **c** In the PbS-3 film, two peaks of the size distribution correspond to particles 40 and 70 nm in size. **d** In the PbS-4 film, a broad peak in the size distribution is observed at 60 nm, the size of about 50% of particles are in the range defined by the inequality 60 nm < $D \leq$ 120 nm. Reprinted from [100] with permission from Elsevier

the distribution corresponds to grains, whose size is 70 nm, with about half of all grains having sizes in the range 60–80 nm (Fig. 2.35a). In the size distribution of nanograins in the PbS-2 film, we observe two peaks, one at 50 nm and the other at 80 nm. The average grain size D is 73 nm, and the sizes of $\sim$55% of the grains are in the range 60–90 nm (Fig. 2.35b). In the PbS-3 film, the two size distribution peaks correspond to grains, whose sizes are 40 and 70 nm, the average size D is 59 nm, and more than 43% of grains have a size from 30 to 50 nm (Fig. 2.35c). In the microstructure of the PbS-4 film, we observe a broad 60 nm size distribution peak, $\sim$20% of grains are $\leq$ 60 nm in size, about 50% of grains have a size in the range from 60 to 120 nm, and the average grain size D is equal 110 nm (Fig. 2.35d).

For determining the band gap, most useful is the part of the optical spectra in which the transmittance changes noticeably as a function of wavelength λ, i.e., the region from 700–800 to 2500–600 nm (Fig. 2.36) corresponding to the pho-ton energies from $\sim$1.6 to $\sim$0.5 eV. Analysis of the optical spectra at $\lambda > 600$ nm allows one to exclude errors that can appear in determining E_g due to the absorption band edge of the substrate at $\lambda \approx 320$ nm. Studies of the microstructure (see Fig. 2.22) show that the PbS-1 film covers no more than 80–85% of the substrate surface since PbS-4 film covers the substrate completely. As a result, the

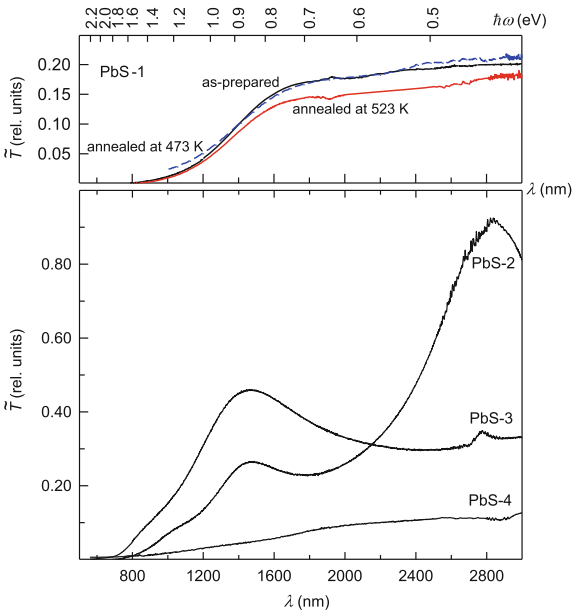

Fig. 2.36 Transmission spectra $\tilde{T}(\lambda)$ (*top*) of the PbS-1 films as-prepared and annealed at 473 and 573 K, and also (*bottom*) of PbS-2, PbS-3, and PbS-4 films [97, 100]. The thickness of PbS-1, PbS-2, PbS-3, and PbS-4 films is equal to 120 ± 20, 200 ± 20, 300 ± 20 and 400 ± 20 nm, respectively. Reprinted from [100] with permission from Elsevier

transmittance $\tilde{T}$ of the PbS-1 film at $\lambda > 800$ nm is nearly twice as high as the transmittance of the PbS-4 film (Fig. 2.36). The highest transmittance $\tilde{T}$ is inherent to the PbS-2 and PbS-3 films (Fig. 2.36). It should be noted that the transmission spectra of the PbS-2 and PbS-3 films exhibit several evident inflection points (see Fig. 2.36), in contrast to the smoother transmission spectra of the PbS-1and PbS-4 films.

In order to quantitatively estimate E_g, absorption spectra rather than transmission spectra are considered. The absorption coefficient σ is the absorbance for a 1 cm thick material layer, $\sigma = (-\lg \tilde{T})/s$, where $\tilde{T} = I/I_0$ is transmittance in relative units, s is the material thickness in cm (in some publications, the coefficient σ is designated by α).

The spectral dependence of the absorption coefficient $\sigma(\omega)$ on the semiconductor band gap E_g (or the Tauc function) has the form [139, 152–154]

$$[\hbar\omega\sigma(\omega)]^{1/n} = A_n(\hbar\omega - E_g), \tag{2.34}$$

where $\omega = 2\pi c/\lambda$ is the incident radiation frequency, $\hbar\omega = 2\pi\hbar c/\lambda = hc/\lambda$ is the photon energy, $A_n = const$ is a coefficient independent of frequency ω but depending on the type of transition. The magnitude n in an exponent is determined by the transition nature (n = 1/2 for the direct allowed transition; n = 3/2 for the direct forbidden transition; n = 2 for the indirect allowed transition and n = 3 for the indirect forbidden transition. When reflection spectra are measured, the $\sigma(\omega)$

value in relation (2.34) is replaced by the reflection function $F(R_\infty) = (1 - R)^2/(2R)$ defined via the reflection coefficient R.

For the direct allowed transitions with $n = 1/2$, relation (2.34) has the form

$$[\sigma(\omega)\hbar\omega]^2 = A_d^2(\hbar\omega - E_g) \equiv A(\hbar\omega - E_g), \tag{2.35}$$

where $A_\mathrm{d} = 2e^2(2\mu_\mathrm{ex})^{3/2}|P_{if}|^2/(\tilde{n}m_0^2\ c\,\hbar^2)$, $\mu_\mathrm{ex} = m_\mathrm{e}m_\mathrm{h}/(m_\mathrm{e} + m_\mathrm{h})$ is the reduced exciton mass; m_e and m_h are the electron and hole effective masses; P_{if} is the matrix element of the $i \to f$ transition between the ith and fth energy levels; $\tilde{n}$ is the refractive index; and e and m_0 are the charge and the free electron rest mass, respectively. This equation is more convenient for the quantitative treatment of experimental optical absorption data and band gap determination. In an ideal case, $\sigma(\omega) \geq 0$ only when $\hbar\omega \geq E_g$ and the experimental results in the "$[\sigma(\omega)\hbar\omega]^2 \leftrightarrow \hbar\omega$" coordinates are described by a linear plot. In a real experiment, since the absorption band is diffuse, the dependence $[\sigma(\omega)\hbar\omega]^2 = f(\hbar\omega)$ is non-linear near the absorption edge; therefore, the band gap E_g is determined as the intercept on the $\hbar\omega$ axis tangential to the linear part of the experimental absorption curve.

Relation (2.34) was derived without taking account of the electron—hole interaction, which may be significant if the difference $(\hbar\omega - E_g)$ is not too high. The spectral dependence of optical absorption derived taking account of the electron-hole interaction [155] has the form

$$\sigma(\omega) = B\{1 - \exp[-C(\hbar\omega - E_g)^{-1/2}]\}^{-1}, \tag{2.36}$$

where B and C are constants. In lead sulfide, the electron-hole interaction is markedly shielded because of the high dielectric constant ε_d (at 300 K, the ε_PbS value varies from 17.2 to 17.9 [138]; therefore, the optical absorption of PbS at $n = 1/2$ is better described by relation (2.30).

Usually, the films are not monodisperse. Considering this fact, Sadovnikov et al. [97] proposed a model for the absorption spectra of polydisperse films. The absorption spectrum of monodisperse nanoparticles is a smooth function of the wavelength λ or energy $E = hc/\lambda$. In the case of polydisperse films, the absorption spectra represent superpositions of the spectra corresponding to nanoparticles of different size,

$$\sigma(\omega) = \sum_i a_i\sigma_i(\omega) = \sum_i a_iA(\hbar\omega - E_{g_i})^{1/2}/\hbar\omega \equiv \sum_i a_iA(E - E_{g_i})^{1/2}/E \tag{2.37}$$

where c_i and E_{g_i} are the relative content of nanoparticles of a definite size in the film and the band gap corresponding to these nanoparticles.

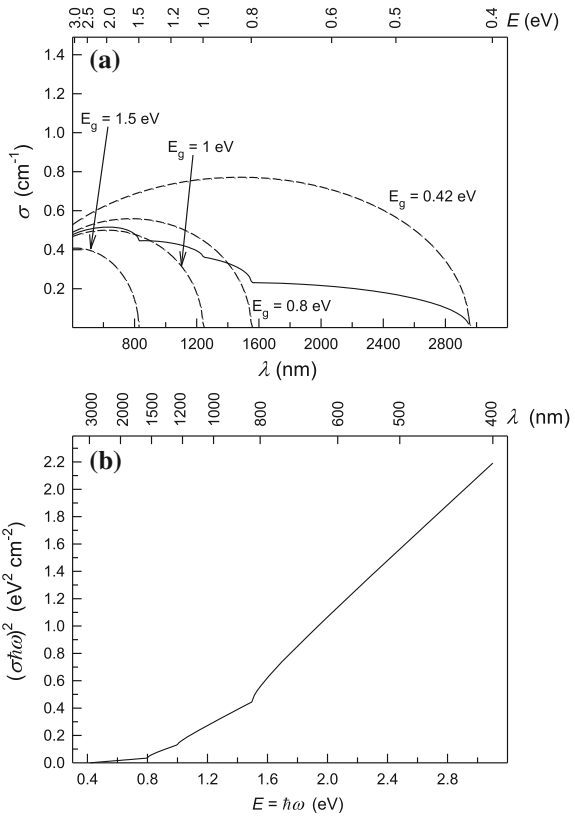

Fig. 2.37 **a** *Solid line* shows the model absorption spectrum calculated as a superposition of (*dashed lines*) the absorption spectra of four groups of nanoparticles (formula (2.37)) with the band gap = 0.42, 0.8, 1.0, and 1.5 eV, and the relative content c_i = 30, 30, 15, and 25%, respectively [97]. **b** The same absorption spectrum plotted in the energy scale: contributions to the absorption in regions *1–4* are made by particles with E_{g_i} = 0.42, 0.8, 1.0, and 1.5 eV (region *1*), 0.42, 0.8, and 1.0 eV (region *2*), 0.42 and 0.8 eV (region *3*), and 0.42 eV (region *4*)

For illustration, Fig. 2.37a shows the model absorption spectrum calculated as a superposition of the absorption spectra of four groups of nanoparticles with the band gap E_{g_i} = 0.42, 0.8, 1.0, and 1.5 eV, and the relative content c_i = 30, 30, 15, and 25%. In Fig. 2.37b, the same model absorption spectrum is shown in the $[\sigma(\omega)\hbar\omega]^2 \leftrightarrow \hbar\omega$ coordinates. In this spectrum, we can see four clearly pronounced regions, which can be used to estimate the band gap corresponding to nanoparticles of different sizes. The observable band gap $E_{g\Sigma}$ can be found by minimizing the quantity of the experimental data with formula (2.35) and determining the portion intercepted on the energy axis $\hbar\omega$ by any linear portion of the curve $[\sigma(\omega)\hbar\omega]^2$ extrapolated to the axis. In polydisperse films, any section of the dependence $[\sigma(\omega)\hbar\omega]^2 \equiv [\sigma E]^2$ is a superposition of $[\sigma_i(\omega)\hbar\omega]^2 \equiv [\sigma_i E]$ values; therefore, the observed band gap $E_{g\Sigma}$ is an additive function of the energies E_{g_i} corresponding to nanoparticles of different size. Considering the identity $[\sigma E]^2 \equiv A^2(E - E_{g\Sigma})$, it was approximately shown [97] that

$$E_{g\Sigma} \sim \sum_i c_i^2 E_{g_i} + 2 \sum_{i \neq j} c_i c_j (E_{g_i} E_{g_j})^{1/2} + |E_{g_i} - E_{g_j}|/3. \tag{2.38}$$

For a monodisperse film, i.e., when $c_1 = 1$ and $c_{i \neq 1} = 0$, relation (2.38) is transformed to the obvious boundary conditions $E_{g\Sigma} \equiv E_{g1}$.

An important feature of continuous films is the existence of developed grain boundaries. This results in diffuse positions of the conduction and valence bands in the electronic structures of particular grains and, as a consequence, in some uncertainty of the band gap and in additional smearing of the optical spectra of the films. This effect is of the same order as the presence of different size nanoparticles in the film, i.e., the size inhomogeneity of the film, as indicated by Mittleman et al. [156].

Thus, the intricate pattern of the absorption spectra of semiconductor films is a consequence of polydispersity.

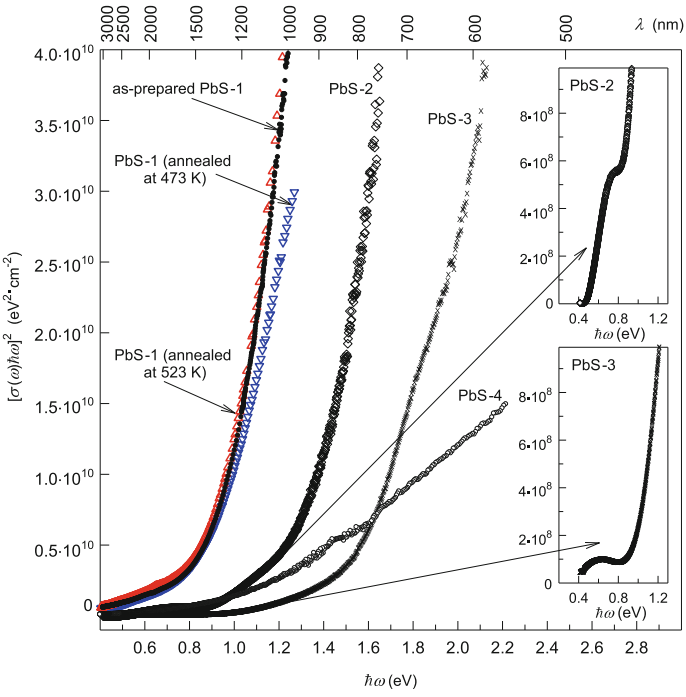

Fig. 2.38 Absorption spectra of the PbS-1 films (*filled circle*) as-prepared and annealed at (*inverted open triangle*) 473 and (*open triangle*) 573 K, and also of (*open diamond*) PbS-2, (*multiplication sign*) PbS-3 (*open circle*), and PbS-4 films on the energy scale [97, 100]. For simplicity, each 5th experimental point is shown only). Insets show the nonmonotonic behavior of an absorption coefficient of the PbS-2 and PbS-3 films in the energy interval from 0.4 to 1.1 eV. Reprinted from [100] with permission from Elsevier

The absorption spectra of lead sulfide nanofilms plotted in the $[\sigma(\omega)\hbar\omega]^2 \leftrightarrow \hbar\omega$ coordinates are shown in Fig. 2.38. Two (PbS-1 and PbS-4) or three (PbS-2 and PbS-3) linear segments can be distinguished in the spectra. More detailed analysis of the plots for $[\sigma(\omega)\hbar\omega]^2$ dependences revealed a non-monotonic variation of the absorption of PbS-2 and PbS-3 films (see insets in Fig. 2.38) in the energy region $\hbar\omega$ = 0.5–1.1 eV; no specific behaviour of absorption was found in this region for PbS-1 and PbS-4 films.

The low-energy absorption edge of all spectra is smeared. The "tails" observed near the absorption edge, i.e, in the region $\hbar\omega < E_g = 0.41$ eV, are mainly caused by the dispersion (deviation from the mean value) of the size of the film nanoparticles, i.e, inhomogeneous broadening [156]. Other possible causes for absorption edge smearing are structure defects of the semiconductor and/or indirect interband transitions. The portions of the absorption curves $\sigma(\omega)$ at $\hbar\omega < E_g$ are described by the Urbach rule [157]: $\sigma(\omega) \sim \exp[\beta(\hbar\omega - E_g)]$.

The quantitative minimization of the experimental data with respect to absorption coefficient $\sigma(\omega)$of the PbS-1, PbS-2, PbS-3 and PbS-4 films by function (2.35) made it possible to find E_g for these films. The calculation showed that the band gap of the synthesized PbS-1 film is 0.92 eV, while the band gaps of the same film after annealing at 473 and 523 K are 0.87 and 0.89 eV, respectively. The average nanoparticle size in the annealed PbS-1 films is 80 nm. For the synthesized and annealed PbS-1 films, the spectral regions with $E < 0.7$ eV are characterized by $E_g \approx 0.42$ eV.

The $[\sigma(\omega)\hbar\omega]^2 = f(\hbar\omega)$ plots for the PbS-2 and PbS-3 films (see Fig. 2.38) have clear-cut singular points, and between these points, linear segments can be distinguished. For the PbS-2 film, these segments are characterized by E_g values 0.43, 0.84, and 1.30 eV. For the PbS-3 film, these segments are characterized by E_g values 0.98 and 1.50 eV, and for the PbS-4 film E_g values equal to 0.41 and 1.05 eV.

A correlation of the E_g values with the particle size distribution in the PbS films (see Fig. 2.35) demonstrated that all films contain up to 50% particles with the size from 100–120 to 300 nm and more. Apparently, the band gap of these large particles is equal to E_g = 0.41 eV of the bulk lead sulfide.

A considerable contribution to the absorption spectra is made by the groups of nanoparticles corresponding to the maxima of size distributions and the adjacent smaller nanoparticles [97, 100]. In the PbS-1 film, the distribution maximum corresponds to 70 nm particles, and 40% of all particles in the film have a size from 10 to 70 nm (Fig. 2.35a). The average nanoparticle size of the PbS-1 film in this range is 60 nm (Table 2.6). This average size can be correlated to the E_g value, which was found to be 0.92 eV. In the annealed PbS-1 films, the nanoparticles have an average size of 80 nm and are characterized by E_g = 0.87–0.89 eV. Size distribution maxima corresponding to nanoparticles of 40 and 70 nm average sizes are inherent in the PbS-2 film (see Fig. 2.35b). This nanoparticle size can be correlated to the E_g values of 1.30 and 0.84 eV, respectively. The size distribution of particles of the PbS-3 film has two maxima, the average particle sizes at these maxima being 35

Table 2.6 Thickness s, nanoparticle size D, and the band gap E_g of nanostructured PbS films [97, 100]

Film	Thickness $s \pm 20$ (nm)	Nanoparticle size			Band gap $E_g \pm 0.1$ (eV)
		XRD	SEM		
		D (nm)	$D \pm 10$ (nm)[a]	D (nm)[b]	
PbS-1 (as-prepared)	120	70 ± 10	70	60 (10–70)	0.92
PbS-1 (annealed at 473 K)	120	80 ± 10	–	–	0.87
PbS-1 (annealed at 523 K)	120	80 ± 10	–	–	0.89
PbS-2	200	75 ± 15	50	40 (10–50)	1.30
			80	70 (60–80)	0.84
PbS-3	300	65 ± 15	40	35 (10–40)	1.50
			70	60 (50–70)	0.98
PbS-4	400	90 ± 15	60	50 (10–60)	1.05

[a]Nanoparticle sizes correspond to the maxima of the size distribution (see Fig. 2.35)

[b]Average size of nanoparticles in the range specified in brackets

and 60 nm (see Fig. 2.35c). The nanoparticles of these sizes are characterized by E_g values found to be 1.50 and 0.98 eV, respectively. For the PbS-4 film, the weakly pronounced size distribution maximum corresponds to an average particle size of 50 nm (see Fig. 2.35d) for which E_g = 1.05 eV (Table 2.6).

The established correlation between the nanoparticle size in the films and the band gap (Table 2.6) can serve to elucidate the influence of the PbS nanoparticle size on the E_g value. The E_g value tends to increase as the nanoparticle size decreases (Fig. 2.39). The band gap of coarse-grained lead sulfide E_b is 0.41–0.42 eV [4, 138], and the E_g of the considered films [97, 100] increases from $\sim 0.8 \pm 0.1$ to 1.5 ± 0.1 eV as the average nanoparticle size decreases from 80 to 35 nm. In view of this, one can consider that a blue shift of the optical absorption band was observed for PbS nanofilms in studies [97, 100]. The value $E_g = 2.0 \pm 0.1$ eV, similar to the cited results [97, 100], was found in another study [158] for PbS films with an average particle size of 40 nm deposited on a glass substrate.

According to the results of Brus [144], for monodisperse semiconductor nanoparticles, the dependence of the exciton energy E_g on the particle radius $R = D/2$ is described as

$$E_g = E_b - \mu_{ex} e^4 / 2n^2\hbar^2 + (n^2\pi^2\hbar^2 / 2\mu_{ex} R^2) - (1.78e^2/\varepsilon_d R), \tag{2.39}$$

where n = 1, 2, 3,…. In relation (2.39), the first and second terms are the band gap of the bulk crystal and the electron and hole binding energy (effective Rydberg energy). For coarse-grained lead sulfide, E_b = 0.41–0.42 eV. The third term $n^2\pi^2\hbar^2/(2\mu_{ex}R^2)$ is the exciton kinetic energy, and the last term $1.78e^2/\varepsilon_d R$ takes into

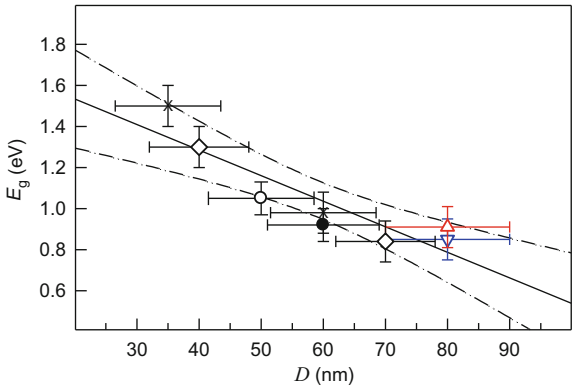

Fig. 2.39 Variation in the observed band gap E_g depending on the nanoparticle size D in the nanostructured PbS films [97, 100]. *Filled circle* as-prepared PbS-1 (*inverted open triangle*), PbS-1 annealed at 473 K, *Open triangle* PbS-1 annealed at 523 K, *Open diamond* PbS-2, (*multiplication sign*) PbS-3, and *Open circle* PbS-4 films. The dashes restrict the 95% confidence interval of determination of the band gap E_g as a function of particle size D. Reprinted from [100] with permission from Elsevier

account the Coulomb interaction between an electron and a hole. Thus, interband absorption should give rise to a series of discrete lines for different n values and the absorption threshold is determined by transition to the ground state with $n = 1$. The sum of the first, third and fourth terms of (2.39) is the effective band gap; for the ground state ($n = 1$), it is expressed as

$$E_g(R) = E_b + (\pi^2\hbar^2/2\mu_{ex}R^2) - (1.78e^2/\varepsilon_d R). \tag{2.40}$$

For lead sulfide with the particle size $D \geq 10$ nm, the correction for Coulomb interaction is lower than $\sim$0.029 eV ($\sim$7% of the value E_b = 0.41–0.42 eV typical of bulk PbS); therefore, in the first approximation, this correction in (2.40) can be neglected. Then the dependence of E_g on the particle radius R is described by the relation $E_g = E_b + \pi^2\ \hbar^2/(2\mu_{ex}R^2)$, откуда следует, что $E_g(R) \propto 1/R^2$ or $E_g(D) \propto 1/D^2$. Using the data obtained in studies [97, 100] and reported previously literature data [141, 143, 158, 159], we plotted the band gap of PbS as a function of $1/D$ where D is the PbS particle size (Fig. 2.40). In should be noted that, in studies [141, 143, 159] the band gap E_g was determined for isolated (separated) PbS particles dispersed in a film polymer matrix. It is seen from Fig. 2.40 that the dependences $E_g(D^{-1})$ measured on PbS films in works [97, 100] and in study [158], substantially differ from those measured on isolated PbS nanoparticles by authors [141, 143, 159].

In the optical properties of semiconductors, the size effects are manifested most clearly if the particle size is commensurable with (or less than) the characteristic

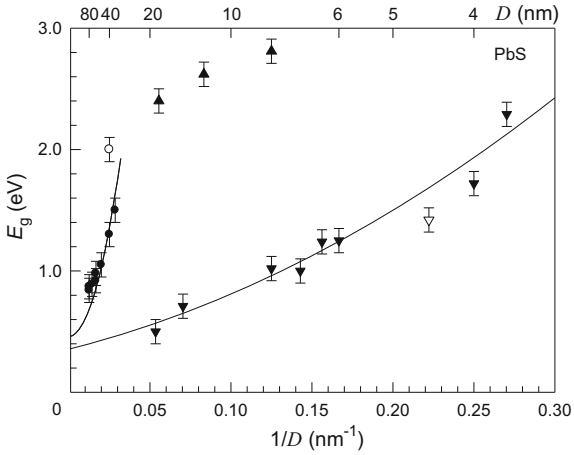

Fig. 2.40 Dependence of the band gap E_g on the PbS nanoparticle size D, plotted as the function $E_g(D) \propto 1/D^2$. *Filled circle* the results [97, 100] obtained on the PbS films, *Open circle* data reported in [158] for the PbS film, *inverted open triangle*, *filled triangle*, and *inverted filled triangle* data obtained for isolated PbS nanoparticles in [141, 143, 159], respectively. In [159], the average size of particles is estimated with methodical errors. For reduction of these errors all data [159] on the particle size D on this figure are increased in 1.5 times. *Solid lines* show the parabolic approximations of the dependences $E_g(D^{-1})$, obtained in the present study and in [159]. The extremely large values of E_g determined in [143] are doubtful. Reprinted from [100] with permission from Elsevier

size $R_{ex} = (n^2\varepsilon m_0/\mu_{ex})a_B$ of the Wannier-Mott exciton where $a_B = \hbar^2/m_0e^2 =$ 0.053 nm is the Bohr radius. A pronounced localization is best achievable for narrow-gap semiconductors with a high dielectric constant; this weakens considerably the electron-hole electrostatic interaction and, as a result, the exciton radius increases (the exciton size may far exceed the crystal lattice constant)., respectively, For lead sulfide at 4 K, the electron and hole effective masses are equal $m_e =$ $(0.092 \pm 0.012)m_0$ and $m_h = (0.090 \pm 0.015)m_0$ [160] therefore, the exciton mass is $\mu_{ex} = (0.045 \pm 0.006)m_0$. For this μ_{ex} value and dielectric constant $\varepsilon_{PbS} \approx 18$ for lead sulfide [138, 160], the radius R_{ex} of the first exciton state with $n = 1$ is $(22 \pm 3)\varepsilon a_B$ or 18–24 nm.

Despite the fact that the average PbS particle size in the films studied by Sadovnikov et al. [97, 100] and Kumara et al. [158] is 2–4 times as large as the exciton size, the band gap is much wider that that in the bulk PbS. This is due to the considerable dispersion of nanoparticle sizes: The presence of particles smaller than ~10–30 nm in the films accounts for the increase in the band gap, while the presence of much larger particles leads to the average particle size increasing to ~60–80 nm [97, 100].

The band gap E_g found for the isolated PbS particles which were dispersed in a polymeric film matrix (Fig. 2.41) is, most often, greater than E_g of nanofilms (see Fig. 2.38). According to Jana et al. [143], the E_g values for 8, 12 and 18 nm

nanoparticles are 2.81, 2.62 and 2.40 eV, respectively. The isolated PbS nanoparticles of ~13 nm size distributed in a copolymer matrix have E_g = 3.36 eV [161]. For isolated PbS particles of 1.5–12.5 nm size dispersed in a polymeric film matrix, E_g was found to be from 2.4 to 0.5 eV [159]. However, the size of PbS nanoparticles in the cited study [159] is apparently underestimated. In the case of 0.8–2.8 nm PbS nanoparticles dispersed in a polyacrylamide film, the blue shift of absorption band to 2.6–2.8 eV is observed [162]. An E_g value of 3.76 eV was reported for isolated PbS nanoparticles not exceeding 15 nm size coated by thioglycerol and dispersed in polyvinyl alcohol [163] (Fig. 2.42). According to Chakraborty and Moulik [12], colloid PbS nanoparticles of 2.4–3.0 nm size synthesized in an aqueous heptane microemulsion are characterized by E_g ranging from 3.45 to 3.30 eV.

Yucel et al. [111] determined the band gap of nanostruc-tured PbS films prepared on a glass substrate by the SILAR process. Deposition was performed from a mixture of 1 M aqueous solutions of lead acetate and sodium sulfide at room temperature. The E_g value was found as a function of conditions of synthesis (pH and the number n and duration t of cycles of substrate dipping into the reaction medium) (Fig. 2.43).

According to the study [111], a PbS film with the greatest band gap of 2.24 eV can be synthesized by the SILAR method at pH = 9.1 using ten dipping cycles, 10 s each.

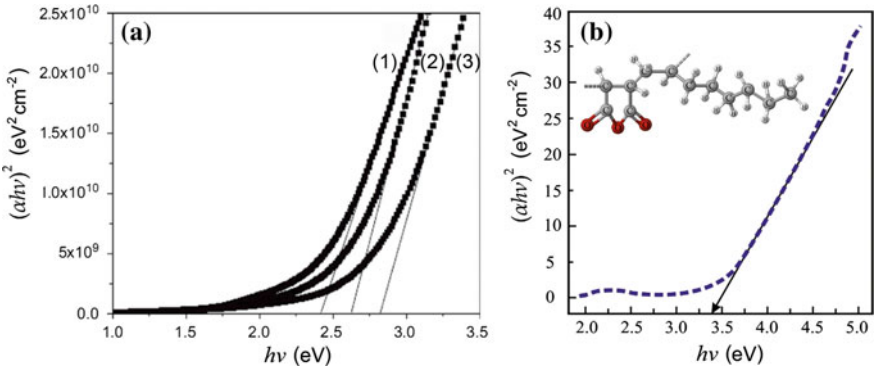

Fig. 2.41 Absorption spectra and band gap of isolated PbS nanoparticles. **a** Polyvinyl alcohol matrix; the deposition temperatures for (*1*) 18, (*2*) 12, and (*3*) 8 nm particles are 303, 293 and 283 K, respectively [143]. **b** Copolymer matrix with PbS nanoparticles of ~13 nm size; the inset shows the presumptive molecular structure of the copolymer [161]

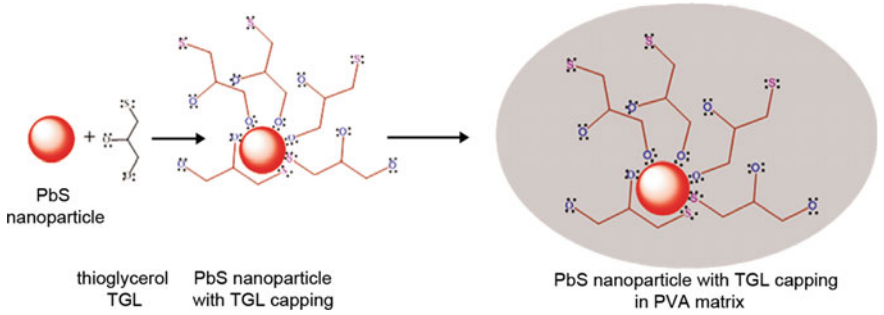

Fig. 2.42 Formation mechanism of thioglycerol-coated PbS nanoparticles in a polyvinyl alcohol matrix [163]

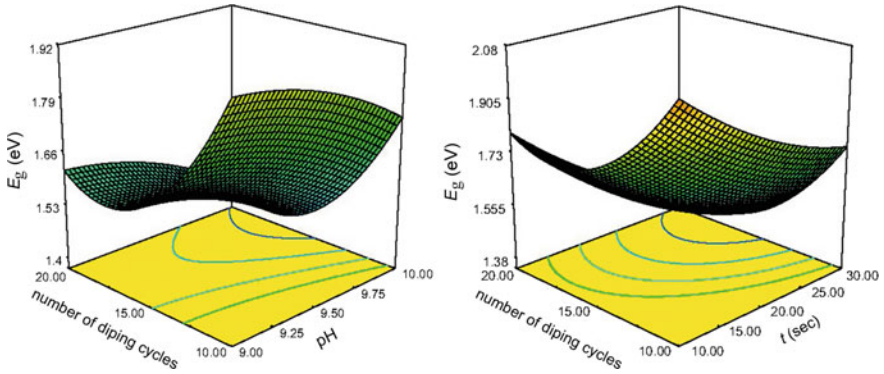

Fig. 2.43 Band gap of PbS films obtained by the SILAR process versus pH of the reaction mixture, duration t and number n of dipping cycles of the substrate into the reaction mixture [111]

2.3.2 Thermal Properties

Data on the thermal expansion of lead sulfide, including films, are very scarce, although these data are useful for the application of films at elevated temperature and for selection of substrates with similar thermal expansion coefficients. It was found [164, 165] that the thermal expansion coefficient of polycrystalline PbS at 300 K is (19–20) $\times$ 10^{-6} K^{-1}. According to study [165] the Grüneisen constant γ of polycrystalline PbS monotonically decreases from $\sim$2.2 to $\sim$1.9 as the temperature is raised from 20 to 340 K, while according to the other study [164] the constant γ, conversely, increases from 1.98 to 2.26 with temperature rise from 320 to 670 K. The lattice properties of PbS were calculated by *ab initio* density functional theory in the quasiharmonic approximation [166]. At 300 K, the thermal

expansion coefficient α and the Grüneisen constant γ of lead sulfide were found to be 29.8×10^{-6} K^{-1} and 2.50–2.52, respectively [166].

The thermal expansion coefficient of a nanostructured PbS film has been measured by Sadovnikov et al. [96, 167]. According to study [96], as the PbS film is cooled down from 423 to 293 K, the lattice constant a decreases from 0.59637 to 0.59326 nm, and this change in the lattice constant is correlated with the thermal expansion coefficient $\alpha(423\ K) = \sim 40 \times 10^{-6}$ K^{-1}. Upon the repeated heating of the PbS film from 293 to 393 K, the lattice constant increases from 0.59326 to 0.59492 nm. This change implies that $\alpha(393\ K) = \sim 28 \times 10^{-6}$ K^{-1}.

The first study of the thermal expansion of the PbS nanofilm in situ at temperatures of up to 473 K was reported by Sadovnikov et al. [167]. The measured linear thermal expansion coefficient of the PbS nanofilm was $(37–39) \times 10^{-6}$ K^{-1}, which is close to the α value determined in another publication [96]. Note that the α value of nanofilms [96, 167] is approximately twice as high as α of the bulk PbS. The authors of study [167] stated, without discussing the physical grounds of the observed effect, that the great difference between the coefficients a is attributable to the small particle size of PbS in the films and to different crystal structures of the films and coarse-grained PbS.

The precision diffraction measurements of the PbS films [167] were carried out in situ at temperatures from 293 to 473 K on a Philips X'Pert automated diffractometer equipped with a position-sensitive fast X'Celerator sector detector. The error of determination of the lattice constant did not exceed $\pm$ 0.00005 nm.

The structure refinement of the PbS film demonstrated [167] that reflection positions and intensities correspond to cubic (space group $Fm\overline{3}m$) lead sulfide with $D0_3$ type structure, which is in line with the results of other publications [95, 96, 100]. The crystal lattice constant a_{cub} of the PbS film is 0.59335 $\pm$ 0.00005 nm. All of the observed diffraction reflections were substantially broadened. Estimation showed that the average coherent scattering region (CSR) in the film is $\sim$40 nm.

According to the results of measurements [167], the dependence of the lattice constant a on the annealing temperature T is non-linear and in the range of 293–473 K, it is described by a polynomial

$$a(T) = a_0 + a_1 T + a_2 T^2 + a_3 T^3, \tag{2.41}$$

with a_0 = 0.59057 nm, $a_1 = -8.1896 \times 10^{-6}$ nm K^{-1}, $a_2 = 7.9452 \times 10^{-8}$ nm K^{-2}, and $a_3 = -6.5455 \times 10^{-11} T^3$ nm K^{-3}. The nonlinear character of the $a(T)$ dependence means that the thermal expansion coefficient α is not constant and it also changes with the temperature.

Figure 2.44 shows the found temperature dependence of the thermal expansion coefficient $\alpha(T)$ for the nanostructured PbS film.

The experimental linear thermal expansion coefficient α is determined as the average expansion coefficient in the temperature interval between the initial temperature 293 K and measured temperature T, i.e.

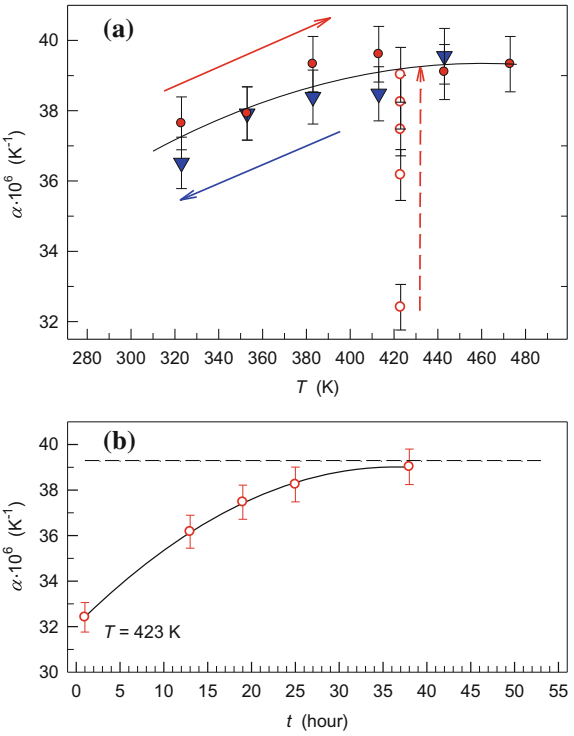

Fig. 2.44 The linear thermal expansion coefficient α of PbS nanofilm versus **a** the temperature and **b** duration of annealing: *Filled circle* the coefficient α during temperature increase from 293 to 423 K, *Inverted filled triangle* the coefficient α during cooling from 423 to 293 K, *Open circle* the coefficient α as a function of the annealing duration of the film at 423 K [167, 168]. Reprinted from [168] with permission from Elsevier

$$\alpha(T) = \frac{1}{a_{293\mathrm{K}}}\frac{\Delta a}{\Delta T} = \frac{a(T) - a_{293\mathrm{K}}}{a_{293\mathrm{K}}(T - 293)}, \tag{2.42}$$

where $a(T)$ and $a_{293\ \mathrm{K}}$ are the crystal lattice constants of PbS film measured at temperature T and at the initial temperature 293 K, respectively. As is seen from Fig. 2.44a, during slow heating of PbS film from 323 to 473 K the thermal expansion coefficient α increases nonlinearly from $\sim 37 \times 10^{-6}$ to $\sim 39 \times 10^{-6}$ K^{-1}. The dependence of the thermal expansion coefficient α on the annealing temperature T in the range 323–473 K can be represented through coefficients of the polynomial (2.41) as

$$\begin{aligned}\alpha(T) &= [(a_1 + a_2T_0 + a_3T_0^2) + (a_2 + a_3T_0)T + a_3T^2]/a_{293\ \mathrm{K}} \\ &= 9.4705 \times 10^{-6} + 6.0273 \times 10^{-8}T - 6.5455 \times 10^{-11}T^2.\end{aligned} \tag{2.43}$$

According to [167], on the scale of the performed experiments the relaxation processes are very slow and equilibrium values of the lattice constant a and thermal expansion coefficient α are achieved only after many-hour annealing. The measured thermal expansion coefficient α of PbS nanofilms is much greater than that reported in the literature for bulk lead sulfide [164–166].

In the most general case, the difference in the coefficients α of nanofilm and coarse-grained PbS can be caused by four reasons [168, 169]: (1) the substrate influence, (2) the method of measurement, (3) different crystal structure of the nanofilm and coarse-grained PbS, and (4) the small size of the particles in nanofilm which leads on to change of phonon spectrum and its edges. The thermal expansion coefficient α of the glass substrate in the temperature range between 293 and 473 K is measured in study [167] by the dilatometry method and is equal to 12.5×10^{-6} K^{-1}, which is a third of that for the PbS nanofilm. Therefore, the effect of the substrate on α of PbS can be excluded. Different methods of measurements of the thermal expansion coefficient used in work [167] and in studies [164, 165] can lead to quantitative differences in the values of the coefficient α, but no more than 5%. Thus, the main reason of the difference in the coefficients α for the PbS film and the coarse-grained PbS are different crystal structure ($D0_3$ type for the PbS nanofilm and $B1$ type for the bulk coarse-grained PbS) and the small size of particles in the nanostructured film.

It is known from the literature that a decrease in the size of particles (grains, crystallites) to the nanometer scale is accompanied by an increase in the thermal expansion coefficient as compared with conventional polycrystals [81, 82]. It is exactly this effect that is observed in study [167]. This effect was explained by Sadovnikov and Gusev in studies [168, 169].

Thermal expansion of a solid state is due to anharmonicity of vibration of atoms. In case of small deviations of r of atoms from the equilibrium position r_0, the potential energy $U(r)$ of a system of interacting atoms can be expanded into a Taylor series according to the displacement value $u = (r - r_0)$. In the equilibrium position $r = r_0$, the energy is minimal; therefore $(\partial U/\partial r)_{r=r_0} = 0$. By limiting the expansion to the third-order terms, which is sufficient for qualitative description of thermal expansion of solids, the energy U, being a function of the displacement value u, can be written in the first approximation as

$$U(u) = U_0 + A_h u^2/2 - \beta_{\text{anh}} u^3/3\,, \tag{2.44}$$

where $A_h = (\partial^2 U/\partial r^2)_{r=r_0}$ is a some constant and $\beta_{\text{anh}} = \frac{1}{2}(\partial^3 U/\partial r^3)_{r=r_0}$ is a coefficient allowing for the anharmonicity of vibration of atoms.

According to Boltzmann distribution, the probability $f(u)$ of deviation of an atom from the equilibrium position by the value u is equal to $f(u) = (A_h/2\pi k_B T)^{1/2}\exp[-U(u)/k_B T]$, therefore the time-average deviation $\langle u \rangle$ of an atom from the equilibrium position is

$$\langle u \rangle = \left[\int_{-\infty}^{+\infty} uf(u)du\right] \Big/ \left[\int_{-\infty}^{+\infty} f(u)du\right] = \frac{k_B T \beta_{\text{anh}}}{A_h^2}. \tag{2.45}$$

The linear expansion coefficient has the form

$$\alpha(T) = (1/a_{293K})d\langle u\rangle/dT = k_B\beta_{anh}(A_h^2 a_{293K}), \tag{2.46}$$

where $a_{293\ K}$ is the crystal lattice constant at 293 K. Thermal expansion (or compression) of solid can be explained only with allowance for anharmonicity of atomic vibrations, i.e. at $\beta \neq 0$, since in harmonic approximation, when $\beta = 0$, the linear thermal expansion coefficient is equal to 0 and thermal expansion is lacking. From (2.46) it is clear that the observed enhancement of the thermal expansion coefficient during transition from bulk to nanocrystalline lead sulfide can occur only when the coefficient β increases, i.e. when anharmonicity of atomic vibrations takes place.

The linear thermal expansion coefficient $\alpha(T)$ is related to specific heat capacity $C_{sp} = C_V/v_m$ per unit volume of substance and measured in J m^{-3} K^{-1} by [170]:

$$\alpha(T) = \gamma C_{sp}(T)/3B \equiv \frac{\gamma}{3B}\frac{C_V(T)}{v_m}, \tag{2.47}$$

where B is the bulk modulus, $\gamma = \left[\sum_{\mathbf{k}} \gamma_{\mathbf{k}} C_V(\mathbf{k})\right] / \left[\sum_{\mathbf{k}} C_V(\mathbf{k})\right]$ is the Grüneisen constant, $\gamma_{\boldsymbol{k}} = -(V/\omega_{\boldsymbol{k}})[\partial(\omega_{\boldsymbol{k}})/\partial V]\} = -\partial(\ln\omega_{\boldsymbol{k}})\partial(\ln V)$ is the Grüneisen parameter for the vibrational mode with wave vector $\boldsymbol{k}$ and angular frequency $\omega_{\boldsymbol{k}} = ck$, c is the velocity of propagation of elastic vibrations in the lattice, $k = |\boldsymbol{k}|$, and v_m is the molar volume.

If the temperature dependences of the Grüneisen constant and the compression modulus are neglected, then in the zeroth approximation the thermal expansion coefficient $\alpha(T)$ in the low-temperature region should exhibit the same temperature dependence as the specific heat capacity C_{sp}. However, in a real solid the values of $\gamma_{\boldsymbol{k}}$ are not similar for all normal modes, therefore the Grüneisen constant γ, which can be considered as a measure of anharmonicity, depends on temperature.

The electronic contribution to heat capacity of dielectrics and semiconductors at 10 K < $T \leq 0.4T_{melt}$ (T_{melt} is the melting temperature) is small, and in this temperature region lattice heat capacity plays the leading role.

If the lattice heat capacity C_V of monoatomic substance is represented in terms of the average energy $\varepsilon(\omega, T) = (\hbar\omega/2)\coth(\hbar\omega/2k_BT)$ of a linear oscillator and the frequency distribution function $g(\omega)$ as $C_V(T) = \int \frac{\partial\varepsilon(\omega,T)}{\partial T} g(\omega)d\omega$, then the expression (2.47) takes the form

$$\alpha(T) = \frac{\gamma}{3v_m B}\int \frac{\partial\varepsilon(\omega,T)}{\partial T} g(\omega)d\omega. \tag{2.48}$$

From (2.48) it is clear that the temperature dependence of the thermal expansion coefficient depends directly on the spectral distribution of frequencies $g(\omega)$.

Thus, the main reason of variation of the lattice properties of nanocrystals in comparison with bulk substances is variation of the shape and boundaries of the phonon spectrum, i.e. change of the frequency distribution function of atomic vibrations.

The main idea of the majority of models for modification of the phonon spectrum of small particles and/or nanostructured systems consists in the appearance of low-frequency modes in the phonon spectrum, which are absent in the spectrum of the bulk crystal [80–82]. According to [81, 171], waves can occur in the nanoparticles, whose length does not exceed the doubled maximum size of the particle D, i.e. $\lambda \leq 2D$; so, on the side of low-frequency vibrations the phonon spectrum is limited by a certain minimal frequency $\omega_{\min} \geq 2\pi \frac{c_t}{2D}$, where c_t is the velocity of propagation of transverse elastic vibrations (i.e. transverse velocity of sound). In bulk crystals, there is no limitation like this. Besides, the phonon spectrum is limited on the side of high frequencies. Taking into account the low- and high-frequency restrictions of the phonon spectrum, the molar heat capacity of a substance, whose molecule contains n atoms, is equal to

$$C_V(T) = n \int_{\omega_{\min}}^{\omega_{\max}} \frac{\partial \varepsilon(\omega, T)}{\partial T} g(\omega) d\omega. \tag{2.49}$$

The distribution of natural vibrations in the presence of low-frequency restrictions was discussed in studies [172–174]. In work [174], expressions for the frequency distribution function $g(\omega)$ and the upper boundary $\omega_{\max}$ of the phonon spectrum of small rectangular particle have been obtained:

$$g(\omega) = V\omega^2/2\pi^2 c_3 + S\omega/8\pi c_2 + L/16\pi c_1, \tag{2.50}$$

$$\omega_{\max} \approx \left(\frac{18\pi^2 N c_3}{V}\right)^{1/3} \left[1 - \frac{S}{144\pi c_2 N^{1/3}} \left(\frac{18\pi^2 c_3}{V}\right)^{2/3} + \Delta(N^{-2/3})\right], \tag{2.51}$$

where V, S and L are the volume, surface area and the total edge length of small particle, N is the number of atoms in the particle, and $\Delta(N^{-2/3})$ is the correction term of the order $N^{-2/3}$. The quantities c_1, c_2 and c_3 are effective propagation velocities of elastic vibrations determined through the velocities of longitudinal and transverse vibrations, c_l and c_t: $c_1^{-1} = c_\ell^{-1} + 2c_t^{-1}$, $c_2^{-1} = \frac{2c_t^4 - 3c_t^2 c_\ell^2 + 3c_\ell^4}{c_t^2 c_\ell^2 (c_\ell^2 - c_t^2)}$ and $c_3^{-1} = c_\ell^{-3} + 2c_t^{-3}$.

Considering (2.50) and (2.51), it was shown in studies [168, 169] that the molar heat capacity (2.49) of a nanocrystalline substance with particles of a right-angled shape can be written upon mathematical transformations as a function not only of the temperature T, but also of the size D of the small particle:

$$\begin{aligned} C_V(T, D) &= n\left[\frac{12\pi^4 N_A k_B}{5}\left(\frac{k_B T}{\hbar\omega_{\max}}\right)^3 + k_1 L_\Sigma T + k_2 S_\Sigma T^2\right] \\ &= C_V^{\text{bulk}}(T) + n(k_1 L_\Sigma T + k_2 S_\Sigma T^2), \end{aligned} \tag{2.52}$$

where the first summand represents the Debye heat capacity of bulk crystal in the low-temperature region, L_Σ and S_Σ are the total edge length and the total surface area of small particles. If we assume that small particles have a cubic shape with edges in length D, then the number of such particles in the volume v_m is equal to $n_p = v_m/D^3$. In this case $L_\Sigma = 12n_pD = 12v_m/D^2$ and $S_\Sigma = 6n_pD^2 = 6v_m/D$. The values $k_1 = (k_B^2 c_1^{-1}/8\pi\hbar)I_2$ and $k_2 = (k_B^3 c_2^{-1}/2\pi\hbar^2)I_3$ are positive constants, $I_m = (4m!/2^{m+1})\sum_{N=1}^{\infty} N^{-m} \equiv (4\ m!/2^{\ m+1})\zeta(m)$, $\zeta(m)$ is the Riemann zeta function ($I_3 = 1.8031$; $I_2 = \pi^2/6$). It is clear from (2.52) that the heat capacity contribution $\Delta C_V(T, D)$ caused by the small size of particles, is equal

$$\Delta C_V(T, D) = n(k_1 L_\Sigma T + k_2 S_\Sigma T^2). \tag{2.53}$$

With allowance for (2.48), (2.52) and expressions for L_Σ и S_Σ, the thermal expansion coefficient of nanocrystalline substance was be presented in studies [168, 169] as

$$\begin{aligned}\alpha(T, D) &= \frac{\gamma C_{V(\text{bulk})}(T)}{3v_m B} + n\frac{\gamma}{3v_m B}(k_1 L_\Sigma T + k_2 S_\Sigma T^2) \\ &= \alpha_{\text{bulk}}(T) + n\frac{\gamma}{3B}\left(\frac{12k_1 T}{D^2} + \frac{6k_2 T^2}{D}\right),\end{aligned} \tag{2.54}$$

where contribution $\Delta\alpha(T, D)$ in the thermal expansion coefficient, which is caused by small size of particles, is equal to

$$\Delta\alpha(T, D) = n\frac{\gamma}{3B}\left(\frac{12k_1 T}{D^2} + \frac{6k_2 T^2}{D}\right). \tag{2.55}$$

Let us determine the theoretical value of the contribution $\Delta\alpha(T, D)$ for nanocrystalline PbS with cubic structure. For lead sulfide, $n = 2$, the average particle size D in PbS nanofilm at 300 K is $\sim$50 nm, and the density of cubic lead sulfide is assumed to be equal to 7.5 g cm^{-3}. Sadovnikov and Gusev [168, 169] calculated the coefficients k_1 and k_2, necessary for quantitative estimation of $\Delta\alpha(T, D)$, using the propagation velocities of longitudinal and transverse elastic vibrations c_l and c_t or elastic constants c_{11}, c_{12}, and c_{44} for lead sulfide [166, 175–178].

In high-symmetry crystals, completely longitudinal or completely transverse atomic vibrations propagate only in those directions that correspond to synchronously moving atomic planes. For cubic crystals, such crystallographic directions are [100, 110, 111] and their equivalents. According to calculation [168, 169] with using data [175], at $\sim$300 K c_l and c_t are $\sim$3975 and $\sim$1881 m s^{-1}. These values are in good agreement with experimental data [179], according to which the velocities c_l and c_t at room temperature are equal to 4080 and 1840 m s^{-1}. Figure 2.45 demonstrates the calculated changes in the velocities of transverse c_t and longitudinal c_l elastic vibrations versus the crystallographic direction for a single crystal of cubic lead sulfide PbS at 300 K. The distances from the figure center (Fig. 2.45) are

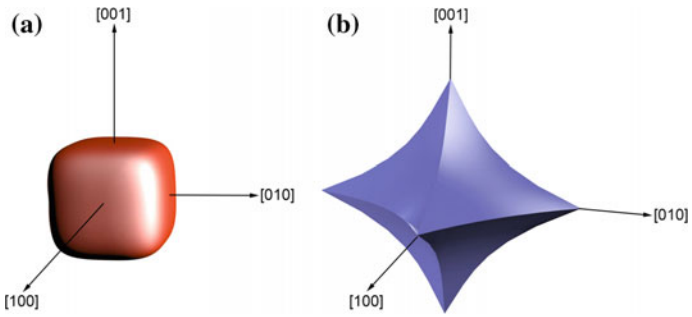

Fig. 2.45 The calculated velocities of transverse c_t (**a**) and longitudinal c_l (**b**) elastic vibrations versus the crystallographic direction for cubic lead sulfide PbS at 300 K [168]. The distance from the figure center is proportional to the velocity value ($c_t^{[100]} = c_t^{[010]} = c_t^{[001]} = 1.9 \times 10^3$ m s^{-1} and $c_\ell^{[100]} = c_\ell^{[010]} = c_\ell^{[001]} = 4.0 \times 10^3$ m s^{-1}). Reprinted from [168] with permission from Elsevier

proportional to the corresponding velocity value ($c_t^{[100]} = c_t^{[010]} = c_t^{[001]} = 1.9 \times 10^3 \mathrm{m\,s^{-1}}$ and $c_\ell^{[100]} = c_\ell^{[010]} = c_\ell^{[001]} = 4.0 \times 10^3 \mathrm{m\,s^{-1}}$).

According to estimations performed with taking into account these values of c_l and c_t, the low and upper boundaries ω_{min} and ω_{max} of the phonon spectrum of a small cubic particle of PbS with edges in length $D = 50$ nm are equal to $\sim 1.18 \times 10^{11}$ and $\sim 2.76 \times 10^{13}$ rad s^{-1}, respectively [168, 169]. At 300 K, the constants k_1 and k_2 are equal to $\sim 1.55 \times 10^{-16}$ J m^{-1} K^{-2} and $\sim 6.00 \times 10^{-8}$ J m^{-2} K^{-3}, i.e. $k_2 \gg k_1$. With increasing temperature to 500 K, the constants k_1 and k_2 increase weakly up to $\sim 1.67 \times 10^{-16}$ J m^{-1} K^{-2} and $\sim 7.06 \times 10^{-8}$ J m^{-2} K^{-3}, respectively [168, 169]. Since $k_2 \geq k_1$, from (2.49) it follows that in the case of small particles, essentially, an additional contribution appears in the thermal expansion coefficient, which is proportional to $S_\Sigma T^2$ and is due to large surface area of small particles. Therefore reduction of the particle size to the nanometer scale should be accompanied by the thermal expansion coefficient growth.

Exactly this effect, namely, ~ 1.7 time greater coefficient α of nanostructured PbS film as compared with bulk PbS, has been found in studies [167–169].

Figure 2.46 shows the dependence of the thermal expansion coefficient of PbS nanofilm in the temperature region between 300 and 500 K calculated as $\alpha_{nano}^{calc}(T, D) = \alpha_{bulk}(T) + \Delta\alpha(T, D)$ with allowance for the derived coefficients k_1 and k_2. The experimental results [162] were used as the $\alpha_{bulk}(T)$ dependence. The variation of the equilibrium particle size in PbS nanofilm versus the temperature was taken into account in the calculation (see Fig. 2.44). It was also considered that with an increase in temperature a small linear growth of the Grüneisen constant γ is observed [164] and the compression modulus B calculated from data [175] decreases. The experimental linear thermal expansion coefficient α of PbS

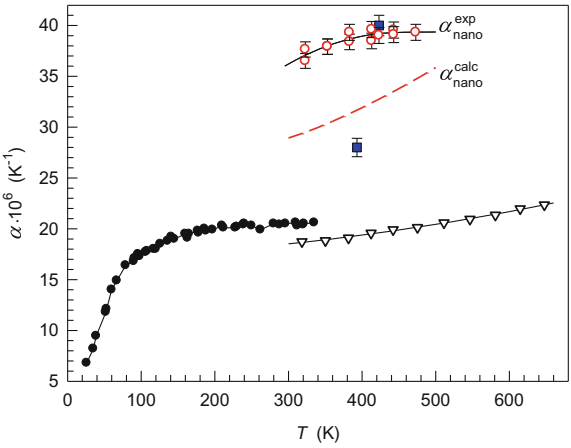

Fig. 2.46 The linear thermal expansion coefficient α of lead sulfide: *Filled square* PbS film [96], *Inverted open triangle* bulk coarse-grained polycrystalline PbS [164], *Filled circle* bulk coarse-grained polycrystalline PbS [165], *Open circle* experimental data of studies [167, 168] for nanostructured PbS film. The *dotted line* shows calculated dependence $\alpha_{nano}^{calc}(T, D) = \alpha_{bulk}(T) + \Delta(T, D)$ of thermal expansion coefficient for PbS nanofilm. Reprinted from [168] with permission from Elsevier

nanofilms [167], as well as the literature data [164, 165] on the coefficient α for bulk coarse-grained lead sulfide and the data [96] for the nanofilm are given in Fig. 2.46 for comparison.

The calculated dependence $\alpha_{nano}^{calc}(T, D)$ for a PbS nanofilm is slightly lower than the experimental dependence $\alpha_{nano}^{exp}(T, D)$: in the examined temperature region, 300–473 K, the difference in the coefficients α is (5–6) × 10^{-6} K^{-1}. Apparently, this difference is due to the approximations of the model [174], which is the basis of the calculation [168, 169]. Besides, the experimental data [175] used for the estimation of effective propagation velocities of elastic vibrations c_1^{-1}, c_2^{-1}, c_3^{-1} and for subsequent calculation of the $\Delta\alpha$ (T, D) value, as well as the data [164] taken as α_{bulk} (T) of lead sulfide can be not quite accurate. In particular, the compression modulus B calculated from the data [175] is half as much again the modulus B measured in study [180]. Besides, the nonstoichiometric distribution of sulfur atoms S in the nanofilm and the difference in the crystal structures ($D0_3$ type for the PbS nanofilm and $B1$ type for the bulk coarse-grained PbS) can make a small, about a few percents, additional contribution to the thermal expansion coefficient of the nanofilm. Therefore the calculated dependence of the thermal expansion coefficient of PbS nanofilm agrees rather well with the experimental dependence $\alpha_{nano}^{exp}(T, D)$ (Fig. 2.46).

The thermal expansion coefficient α of PbS film at 423 K estimated from data [96] on lattice constant variation during cooling of the film from 423 to 293 K is ∼40 × 10^{-6} K^{-1} and agrees well with the results obtained in studies [167, 168]. Estimation of α from data [96] obtained during cooling of the film from room

temperature to 393 K yields a smaller value, $\sim 28 \times 10^{-6}$ K^{-1}. This can be caused by the circumstance that in work [96] the annealing duration of PbS film at 393 K was insufficient for attaining the equilibrium value of the crystal lattice constant. Indeed, the equilibrium values of the lattice constant and thermal expansion coefficient (see Fig. 2.44) are achieved only after long-term 40 h exposure of films.

Since $\beta_{\text{anh}} = A_h^2 a_{293\text{K}} \alpha / k_{\text{B}}$, then with allowance for (2.49) the dependence between the coefficient of anharmonicity of atomic vibrations and the particle size can be expressed as

$$\beta_{\text{anh}}(T, D) = \frac{A_h^2 a_{293\text{K}}}{k_{\text{B}}} \left[\alpha_{\text{bulk}}(T) + n \frac{\gamma}{3 v_{\text{m}} B} (k_1 L_\Sigma T + k_2 S_\Sigma T^2) \right]. \tag{2.56}$$

According to (2.56), reduction of the particle size that leads to the growth of their surface area S_Σ should be accompanied by an increase in the anharmonicity of atomic vibrations.

According to [49, 95–97, 100, 123, 181], the lattice constant of lead sulfide remains unchanged when its particle size decreases. If we assume that the coefficient A_h also remains constant when the particle size decreases, then the ratio of anharmonicity coefficients of nanofilm and bulk PbS is $\beta_{\text{anh-nano}}/\beta_{\text{anh}} = \alpha_{\text{nano}}/\alpha$, hence $\beta_{\text{anh-nano}} = (\alpha_{\text{nano}}/\alpha)\beta_{\text{anh}}$. At 293 K, the coefficient α of bulk PbS is $\sim 21 \times 10^{-6}$ K^{-1} [160, 165], while the measured thermal expansion coefficient of nanofilm is $\alpha_{\text{nano}} \cong 36 \times 10^{-6}$ K^{-1}. Therefore $\beta_{\text{anh-nano}} \approx 1.7 \beta_{\text{anh}}$.

Thus, the linear thermal expansion coefficient α of a PbS nanofilm in the temperature range of 293–443 K is approximately 1.5–2 times as high as the a of bulk PbS. The observed difference between the coefficients α is associated with the small PbS particle size in the film, resulting in a change of the distribution function of the atomic vibration frequencies and increase in the vibration anharmonicity.

2.3.3 *Stability of Nanostructured Lead Sulfide*

The most widely used devices based on lead sulfide are fire alarm sensors, flame sensors and heat source detection systems; therefore, the thermal and oxidation stabilities of the nanostate largely determine the application of nanostructured PbS in this type of devices. However, nanoparticles and quantum dots are metastable materials and are prone to recrystallization and oxidative degradation, which is promoted by their large surface area. Therefore, extensive use of nanostructured PbS requires the knowledge of temperature range in which the nanoparticles do not grow (no transition from the nano- to the coarse-grained state) and the temperature of the onset of oxidation.

The thermal stability of the structure of PbS nanofilms obtained by laser deposition on heated quartz substrates has been studied [123]. The annealing of films in air demonstrated that upon temperature rise to 375 K, the intensity ratio of

some diffraction reflections changes but no additional peaks are observed up to 475 K; hence, the PbS nanofilm is not oxidized. The change in the diffraction reflection intensities was attributed [123] to the fact that a phase transition from the $B1$ structure to the high-temperature cubic $B3$ structure (space group $F\overline{4}3m$) takes place in the PbS film at 375 K.

From the XRD patterns of the vacuum-annealed nanostructured PbS powders and films, the particle size, lattice microstrain, and lattice constant of the powders and films were determined as functions of temperature.

The vacuum annealing of PbS nanopowders at a temperature of up to 700 K leads to minimization of microstrains and a slight growth of nanoparticles (Fig. 2.47a); hence, this temperature range can be regarded as the thermal stability region of lead sulfide nanopowders.

The temperature range from 700 to 800 K, in which the particle size increases 5–10-fold, corresponds to the temperature of collective recrystallization of PbS nanopowder. The vacuum annealing of PbS nanofilms at a temperature of up to 673 K is also accompanied by a minor growth of nanocrystallites, while at higher annealing temperature, the particle size increases jumpwise (Fig. 2.47b). The recrystallization in nanofilms starts at a lower temperature than the recrystallization of nanopowders. This is a consequence of tighter contact of crystallites in nanofilms compared with the particle contact in nanopowders.

According to [82, 185], collective recrystallization in nanocrystalline materials starts, most often, at the temperatures $T_{recr} \approx (0.30–0.35)T_{melt}$. In other studies [182, 183], the recrystallization temperature of PbS nanopowders and nanofilms

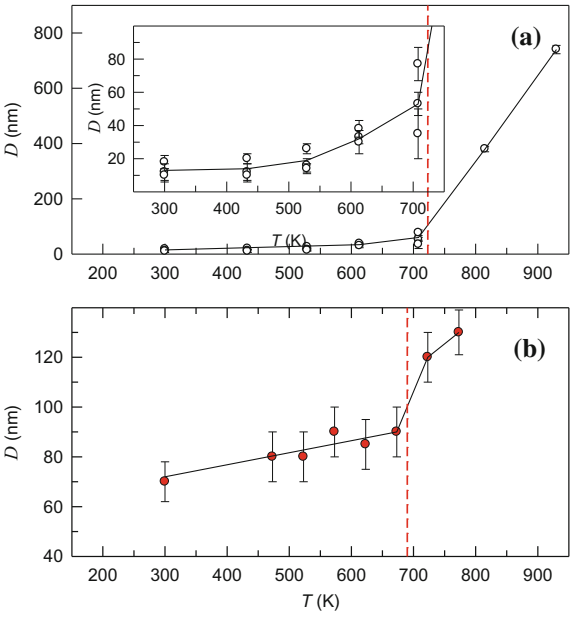

Fig. 2.47 Effect of the vacuum annealing temperature on the particle (crystallite) size in nanostructured PbS **a** powders and **b** films [182, 183]. The temperature of the onset of recrystallization is marked by the *dashed line*

was found to be ~700 K, which is half the melting point of bulk PbS (1391 K). Thus, PbS nanopowders and nanofilms have higher relative recrystallization temperature $T_{recr} \approx 0.5T_{melt}$, i.e, they differ from other nanomaterials by a higher thermal stability of particle (crystallite) size.

Analysis of phase composition of the annealed PbS powders shows that annealing at 930 K is accompanied by changes in phase composition: the formation of metallic lead Pb in addition to PbS.

The oxidation of PbS nanopowders with atmospheric oxygen was studied on samples with a particle size of 10–20 nm [183]. The XRD patterns of the initial PbS nanopowder with a particle size of 15 nm and of the same powder after annealing at a temperature from 473 to 623 K are presented in Fig. 2.48. The XRD pattern of the initial PbS nanopowder shows only reflections from cubic lead sulfide. Small increasing anneling temperature up to 423 K initiates the reaction between PbS and O_2, as is indicated by the appearance of strong diffraction reflections from oxygen-containing phases on XRD patterns.

Annealing of PbS nanopowder at 473–523 K does not cause any narrowing of the diffraction reflections (Fig. 2.48). Therefore, the lead sulfide particles retain their small size in this temperature range. After annealing of the nanopowder at $T > 523$ K, weakening of an intensity of all diffraction reflections from cubic lead

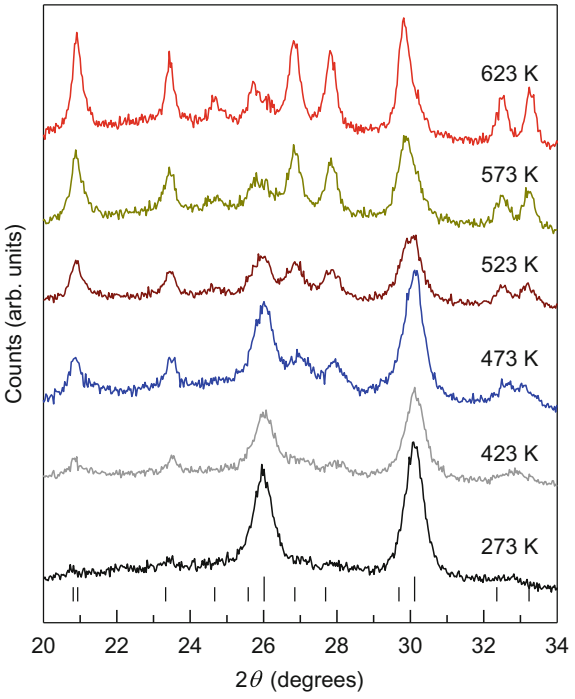

Fig. 2.48 XRD patterns of the initial PbS nanopowder with a particle size of 15 nm and of the same nanopowder after annealing in air at a temperature from 423 to 623 K. Long and short ticks indicate reflections from PbS and $PbSO_4$, respectively [183]. The XRD patterns are recorded in Cu$K\alpha_{1,2}$ radiation

sulfide is observed (Fig. 2.48). It is a consequence of decreasing content of PbS phase in annealed nanopowder.

Most of the nanopowders annealed in air at a temperature from 423 to 523 K contain lead sulfite $PbSO_3$. The absence of the $PbSO_4$ lead sulfate phase in the oxidation products does not mean that this phase does not form at all. It is likely that, under the given conditions, the $PbSO_4$ disappearance rate is higher than the rate of formation of this phase and, accordingly, this phase does not accumulate in the reaction products. As the temperature is raised to 573 K, the $PbO{\cdot}PbSO_4$ phase appears along with lead sulfate. When the temperature increases to 623 K, $PbO{\cdot}PbSO_4$ phase disappears and $PbSO_4$ lead sulfate starts to accumule.

Figure 2.49 presents the XRD patterns of the initial nanostructured PbS film with particle size of 70 nm and of the same film after annealing in air at a temperature from 473 to 773 K [183].

The XRD pattern of the initial PbS film shows only reflections from cubic lead sulfide. Annealing of the film at 473–573 K leads to a narrowing of the diffraction

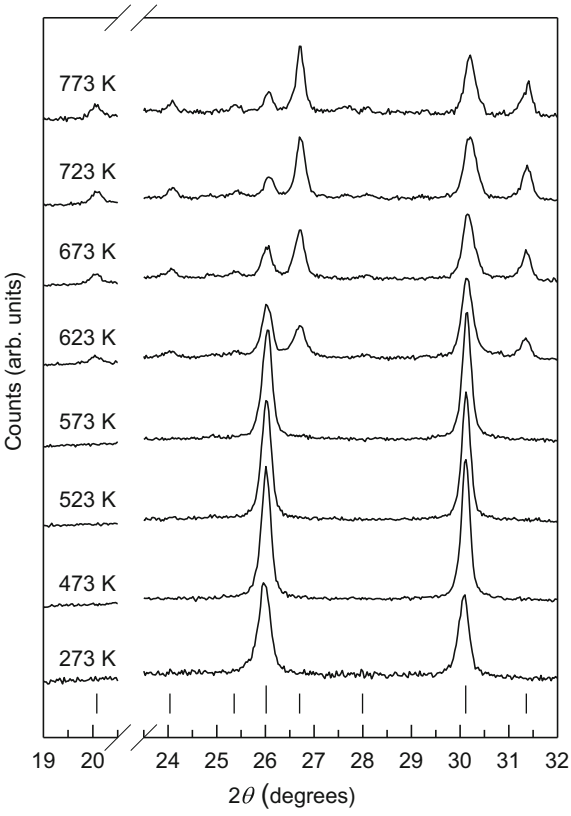

Fig. 2.49 XRD patterns of the initial PbS film with thick of ~100 nm and particle size of 70–80 nm on a glass substrate and of the same film annealed in air at a temperature from 473 to 773 K. Long and short ticks indicate reflections from cubic PbS and the oxide-sulfate $PbO{\cdot}PbSO_4$ phase, respectively [183]. The XRD patterns are recorded in Cu$K\alpha_{1,2}$ radiation

reflections of cubic lead sulfide because of the growth of the PbS nanoparticles from 70 to 90 nm.

Annealing of the PbS film at $T < 623$ K does not change its phase composition; that is, no oxidation takes place. The film annealed at 623 K is partially oxidized, and its XRD pattern shows reflections from the surface oxide-sulfate $PbO{\cdot}PbSO_4$ phase (Fig. 2.49). According to XRD data, the size of the PbS particles decreases from 90 to 50 nm in the temperature range from 573 to 673 K because of their surface oxidation. The formation of the loose $PbO{\cdot}PbSO_4$ phase on the surface increases the film thickness to 420 nm. As determined by XRD, the particle size of the surface $PbO{\cdot}PbSO_4$ phase is about 12 nm, and the particle size remains invariable as the temperature is further raised up to 773 K [182].

According to XRD data, the content of the oxide-sulfate phase in the film increases as the annealing temperature is increased, and no other oxidation products appear in the film up to 773 K.

Thus, the nanostructured lead sulfide film is stable in air up to 573 K.

Comparative analysis of the oxidative activities of lead sulfide demonstrated that the temperatures of the onset of all oxidative processes are much lower for PbS nanopowders than for the bulk coarse-grained sulfide, these processes being facilitated by oxygen-containing impurities [183, 184]. A decrease in the particle size is accompanied by a shift of the onset of oxidation to lower temperatures, while the ox idation of bulk lead sulfide starts at about 800 K [7].

The sequence of transformations involved in the oxidation of lead sulfide is illustrated in Fig. 2.50 in relation to PbS nanopowder with a particle size of 15 nm [183].

The presence of a small amount ($\sim$10 wt%) of $PbSO_3$ lead sulfite in the initial nanopowder is due to its formation at the PbS synthesis stage. As the temperature is raised from 423 to 473 K, the amount of $PbSO_3$ first increases and then (on further temperature rise) decreases, and at 573 K, this phase disappears. The absence of PbO in the temperature range of 423–623 K indicates that the reactions yielding

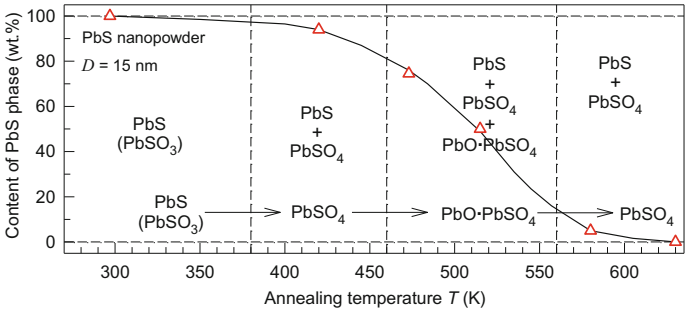

Fig. 2.50 Content of the PbS phase in a PbS nanopowder with a particle size of 15 nm as a function of annealing temperature in air [183]. A minor amount of $PbSO_3$ is present in the synthesized nanopowder as an impurity. The *vertical dashed lines* mark the conventional temperatures of transitions from one phase to the other

this oxide as the final product proceed at higher temperature > 700 K. The temperature of the onset of oxidation of PbS nanopowders increases with increase in the nanoparticle size.

When PbS nanofilms are annealed in air at temperatures below 623 K, no oxidation takes place. This is consistent with the data of study [123]. Annealing at $T > 623$ K leads to partial film oxidation to give the PbO $PbSO_4$ oxide sulfate phase on the film surface. Thus, the nanostructured film of lead sulfide is stable in air up to 573 K and is more stable against oxidation than nanopowders [183].

The results obtained by Mikhlin et al. [186] are useful for the understanding of the oxidation pattern of nanostructured PbS. According to [186] s, the surface of a single-crystalline sulfide is oxidized in air only an increased relative humidity reaching ~90%. The oxidation products form ~20-nm protrusions on the PbS surface. Water condensed on the protrusions promote the oxidation of PbS. 0ver a period of three to five days, the protrusions uniformly cover the surface and them merge together to form a loose surface oxide layer. At normal or low air humidity, the lead sulfide surface is not oxidized. The oxidation of nanostructured PbS also starts on the surface but at a lower humidity.

According to Ihly et al. [187], keeping PbS quantum dots in air is accompanied by a blue shift of the first exciton peak in the optical spectra. This shift is caused by partial oxidation of the QDs. Nanostructured films were prepared by layer-by-layer deposition of lead sulfide accomplished by dipping the substrate into a colloid solution of QDs. The oxidation of PbS nanofilms in air was found to induce broadening of the first exciton peak. In order to prevent the oxidative degradation of nanostructured lead sulfide films, it was proposed to cover the films by an amorphous Al_2O_3 layer [187]. A 18-nm thick Al_2O_3 layer completely prevents the oxidation of PbS nanofilms and prevents the growth of nanoparticles in the films.

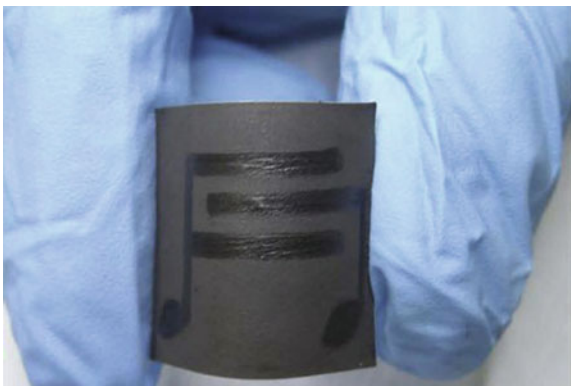

Fig. 2.51 Photograph of flexible photodetector made of PbS quantum dots on a paper substrate [192]

2.4 Applications of Nanostructured Lead Sulfide

Traditional applications of lead sulfide, in particular nanostructured one, in devices such as broad-band photodetectors, high-efficiency solar cells, thermoelectric transducers, optical switches, fire alarm sensors and photovoltaic, photonic and optoelectronic cells are known and have been repeatedly described [188–196]. The application of nanostructured lead sulfide is exemplified in Fig. 2.51, which shows a photograph of a flexible photodetector based on paper covered by a layer of PbS quantum dots [192]. Nanostructured PbS has been used as the key working part in systems of detection of extraterrestrial objects by their thermal emission and in the operated and autonomous (unaided) target guidance systems.

Less widely known is the use of nanostructured PbS as a solid-phase sensor for detection of gases [CO, CO_2, SO_2, N_2, NO and especially NO_2 and NH_3 [197–201], for monitoring of heavy metals, including lead, in aqueous media [202, 203]. Polymeric matrices with PbS nanoparticles are used for protection from γ-radiation [204, 205].

As a result of active integration of the achievements of chemistry, biology and medicine, a background for biomedical applications and development of more perfect tools for medical diagnosis and therapy [206] using nanostructured lead sulfide has been created in the last decade. An example is provided by hybrid PbS nanoparticles coated by *L*-cysteine as a capping agent [58]. Of interest is the drug delivery to injured organs and tumour cells, which is a prerequisite for more successful therapy. For this purpose, it is especially promising to use core-shell sulfide heteronanostructures [207].

Enhancement of the luminescence intensity of the hybrid sulfide heteronanostructures based on PbS is attained owing to combination of luminescent sulfide nanoparticles with metal (especially silver) nanoparticles possessing the surface plasmon resonance. The injured areas can be visualized by using luminescent PbS quantum dots combined into a single nanostructure with organic drugs. Hybrid nanomaterials of this type based on PbS find use and are often indispensable in biosensorics, medicine, green chemistry and other areas [207–210]. Furthermore, the design of hybrid nanomaterials involving lead sulfide promotes elaboration of new analytical methods for the detection and identification of impurities, preconcentration and separation of compounds and visualization of biological action [211–213]. For example, in recent years, many reports have appeared about the successful synthesis and application in vivo of multifuctional hybrid nanostructures for the targeted drug delivery to damaged cells. Apart from other compounds, lead, cadmium and zinc sulfides are used in these structures as luminescent markers.

Lead sulfide nanoparticles embedded in multi-walled carbon nanotubes have been proposed as highly sensitive genomic sensors for the detection of pathogenic bacteria [214].

In parallel with the studies devoted to biomedical applications of PbS nanoparticles, the toxicity of nanostructured lead sulfide was studied [215, 216]; the

results confirmed the applicability of these particles in living organisms provided that the PbS particles are coated by protective biologically harmless shells.

Controllable self-assembly of star-shaped PbS nanocrystals into large-scale ordered close-packed arrays was demonstrated in study [217]. The obtained arrays of star-shaped PbS nanocrystals can be used as anisotropic nanostructured materials for photoelectronic and photonic nanodevices.

The key principles and approaches developed for the synthesis and investigations of various forms of nanostructured lead sulfide are used in relation to other nanocrystalline compounds ranging from sulfides to oxides and carbides. For example, the effect of the small particle size on the thermal expansion and non-stoichiometry of nanocrystalline Ag_2S has been considered in studies [218–220] using an approach proposed previously [168, 169] for nanostructured PbS. Modification of optical and electronic properties of indium and gallium oxide nanofilms has been considered by Chen et al. [221], who took into account data of a study of PbS films [100].

Nanostructured PbS acquire desirable properties when synthesized by processes that ensure the controlled size of structure elements and passivation of the surface. Among numerous methods of synthesis of nanostructured PbS, these conditions are met by deposition from aqueous solutions, which is implemented in many ways. Synthesis in water makes it possible to avoid the influence of toxic organic ligands or toxic organic solvents on biological objects when PbS quantum dots are utilized as biolabels. It can be expected that further development of the methods for the synthesis of PbS nanoparticles of specified size and shape would extend the scope of their applicability, in particular, in optoelectronics, biology and medicine.

The conversion and storage of clean and sustainable energy are major challenges that we are facing today under the background of the energy crisis. As the performance of energy conversion and storage devices depend significantly upon the advancement of their materials, many new energy materials including nanostructured PbS have been developed to meet these challenges. Based on its unique physical and chemical properties, nanostructured lead sulfide and modified lead sulfide nanomaterials promise many advanced applications in the development of technologies of conversion and storage of energy. Moreover, lead sulfide nanomaterials possess such advantage as low cost, which is of great importance for their practical applications.

References

1. Lin, J.C., Sharma, R.C., Chang, Y.A.: Pb-S (Lead-Sulfur). In: Massalski, T.B. (ed.) Binary Alloy Phase Diagrams, 2nd edn, vol. 3, pp. 3005–3009. Materials Park, Ohio (1990) (ASM Intern. Publ.)
2. Lin, J.C., Sharma, R.C., Chang, Y.A.: The Pb-S (lead-sulfur) system. Bull. Alloy Phase Diagr. **7**(4), 374–381 (1986)
3. Scanlon, W.W.: Recent advances in the optical and electronic properties of PbS, PbSe, PbTe and their alloys. J. Phys. Chem. Solids. **8**(1), 423–428 (1959)

4. Schoolar, R.B., Dixon, J.R.: Optical constants of lead sulfide in the fundamental ab-sorption edge region. Phys. Rev. **137**(2A), 667–670 (1965)
5. Zemmel, J.N., Jensen, J.D., Schoolar, R.B.: Electrical and optical properties of epitaxial films of PbS, PbSe, PbTe and SnTe. Phys. Rev. **140**(1A), 330–342 (1965)
6. Hodes, G.: Chemical Solution Deposition of Semiconductor Films, p. 377. Dekker, New York (2002)
7. Sadovnikov, S.I., Gusev, A.I., Rempel, A.A.: Nanostructured lead sulfide: Synthesis, structure, and properties. Russ. Chem. Rev. **85**(7), 731–758 (2016)
8. Rempel, A.A.: Nanotechnologies. Properties and applications of nanostructured materials. Russ. Chem. Rev. **76**(5), 435–461 (2007)
9. Pawar, S.M, Pawar, B.S., Kim, J.H., Joo, O.-S., Lokhande, C.D.: Recent status of chemical bath deposited metal chalcogenide and metal oxide thin films. Curr. Appl. Phys. **11**(2), 117–161 (2011)
10. Deng, D., Xia, J., Cao, J., Qu, L., Tian, J., Qian, Z.: Forming highly fluorescent near-infrared emitting PbS quantum dots in water using glutathione as surface-modifying molecule. J. Coll. Interf. Sci. **367**, 234–240 (2012)
11. Zhang, B., Li, G., Zhang, J., Zhang, Y., Zhang, L.: Synthesis and characterization of PbS nanocrystals in water/C12E9/cyclohexane microemulsions. Nanotechnology **14**(3), 443–446 (2003)
12. Chakraborty, I., Moulik, S.P.: On PbS nanoparticles formed in the compartments of water/AOT/n-heptane microemulsion. J. Nanoparticle Res. **7**(2–3), 237–247 (2005)
13. Jiao, Y., Gao, X., Lu, J., Chen, Y., Zhou, J., Li, X.: A novel method for PbS quantum dot synthesis. Mater. Lett. **72**, 116–118 (2012)
14. Karim, M.R., Zaman, M.D.A., Zaman, M.D.B.: A conventional synthesis approach to prepare lead sulfide (PbS) nanoparticles via solvothermal method. Chalcogen. Lett. **11**(10), 531–539 (2014)
15. Li, F., Huang, X., Kong, T., Liu, X., Qin, Q., Li, Z.: Synthesis and characterization of PbS crystals via a solvothermal route. J. Alloys Comp. **485**(1–2), 554–560 (2009)
16. Kitaev, G.A., Bol'shchikova, T.P., Fofanov, G.M., Yatlova, L.E., Goryukhina, N.M.: Thermodynamic justification of metal sulfide deposition conditions from aqueous solutions by thiourea. In: Kinetika i Mekhanizm Obrazovaniya Tverdoi Fazy (Kinetics and Formation Mechanism of the Solid Phase), pp. 113–126. Ural Pedagogical Institute, Sverdlovsk (1968) (in Russian)
17. Gaiduk, A.P., Gaiduk, P.I., Larsen, A.N.: Chemical bath deposition of PbS nanocrystals: Effect of substrate. Thin Solid Films. **516**, 3791–3795 (2008)
18. Wang, J., Tang, S.H., Wang, B.Y., Li, Y.Q.: In-situ interaction of nano-PbS with gelatin. Sci. China Chem. **56**(11), 1593–1600 (2013)
19. Sadovnikov, S.I., Kuznetsova, Yu., V., Rempel, A.A.: Synthesis of a stable colloidal solution of PbS nanoparticles. Neorg. Mater. **50**(10), 1049–1056 (2014) (in Russian). (Engl. Transl.: Inorg. Mater. **50**(10), 969–975 (2014))
20. Sadovnikov, S.I., Gusev, A.I.: Chemical deposition of nanocrystalline lead sulfide powders with controllable particle size. J. Alloys Comp. **586**, 105–112 (2014)
21. Kozhevnikova, N.S., Sadovnikov, S.I., Rempel, A.A.: One-pot synthesis of lead sulfide nanoparticles. Zh. Obshch. Khim. **81**(10), 1608–1613 (2011) (in Russian). (Engl. Transl.: Russ. J. Gen. Chem. **81**, 2062–2066 (2011))
22. Sadovnikov, S.I., Kuznetsova Yu, V., Rempel, A.A.: A method of producing a colloidal solution of lead sulfide nanoparticles. Patent No. 2567326 of Russian Federation, pp. 1–5 (2015)
23. Froment, M., Lincot, D.: Phase formation processes in solution at the atomic level: Metal chalcogenide semiconductors. Electrochem. Acta. **40**(10), 1293–1303 (1995)

24. Yusupov, R.A., Abzalov, R.F., Smerdova, S.G., Gafarov, M.R.: Sophisticated heterophase equilibria in the system "Pb (II)—water—KOH". Chem. Comput. Simul. Butlerov Commun. **3**, 29–36 (2000) (in Russian)
25. O'Brien, P., Saeed, T.: Deposition and characterization of cadmium sulfide thin films by chemical bath deposition. J. Cryst. Growth. **158**(4), 497–504 (1996)
26. O'Brien, P., McAleese, J.: Developing an understanding of the processes controlling the chemical bath deposition of ZnS and CdS. J. Mater. Chem. **8**(11), 2309–2314 (1998)
27. Osherov, A., Ezersky, V., Golan, Y.: The role of solution composition in chemical bath deposition of epitaxial thin films of PbS on GaAs(100). J. Cryst. Growth. **308**(2), 334–339 (2007)
28. De Farias, P.M.A., Saegesser, Santos D., de Menezes, F.D., de Carvalho Ferreira, R., de Lourdes Barjas-Castro, M., Castro, V., Moura Lima, P.R., Fonte, A., Cesar, C.L.: Core-shell CdS/Cd(OH)2 quantum dots: synthesis ana bioconjugation to target res cells antigens. J. Microscopy. **219**(3), 103–108 (2005)
29. Kozhevnikova, N.S., Sadovnikov, S.I., Uritskaya, A.A., Gusev, A.I.: Lead homogeneous and heterogeneous ion equilibria in water solutions. Izv. VUZov. Khimiya i Khim. Technologiya—Chem. Chem. Technol. **55**(3), 13–18 (2012). (in Russian)
30. Kozhevnikova, N.S., Sadovnikov, S.I., Uritskaya, A.A., Gusev, A.I.: Considering the polynuclear complexes in the ionic equilibria of the Pb^{2+}–H_2O system. Zh. Obshch. Khim. **82**(4), 538–547 (2012) (in Russian) (Engl. Transl.: Russ. J. Gen. Chem. **82**(4), 626–634 (2012))
31. Powell, K.J., Brown, P.L., Byrne, R.H., Gajda, T., Hefter, G., Leuz, A.-K., Sjöberg, S., Wanner, H.: Chemical speciation of environmentally significant metals with inorganic ligands. Part 3: The Pb^{2+} + OH^-, Cl^-, CO_3^{2-}, SO_4^{2-}, and PO_4^{3-} systems (IUPAC Technical Report). Pure Appl. Chem. **81**(12), 2425–2476 (2009)
32. Markov, V.F., Maskaeva, L.N., Ivanov, P.N.: Calculation of the conditions of formation of the solid phase of metal chalcogenides by hydrochemical deposition. Condens. Media Interph. Bound. **6**(4), 374–380 (2004). (in Russian)
33. Wang, Y., Chai, L., Chang, H., Peng, X., Shu, Y.: Equilibrium of hydroxyl complex ions in Pb^{2+}–H_2O system. Trans. Nonferrous Met. Soc. China. **19**(2), 458–462 (2009)
34. Semenov, V.N., Ovechkina, N.M., Khoviy, D.A.: Influence ща hydroxo ycomplexes on the process of deposition and phase composition of the SnS and PbS films. Vestn. Voronezhsk. Univ., Ser. Khimiya, Biologiya, Farmatsiya. **2**, 50–55 (2007) (in Russian)
35. Dean, J.N. (ed.): Lange's Handbook of Chemistry, 15th edn., p. 1424. McGraw-Hill, New York (1998)
36. Patnaik, P.: Dean's Analytical Chemistry Handbook, 2nd edn., pp. 1280. McGraw-Hill, New York (2004) (Table 4.2)
37. Kawai, T.: Ishiguro Shin–ichi, Ohtaki H. A thermodynamic study on hydrolytic reactions of lead(II) ion in an aqueous solution and dioxane-water mixtures. I. Potentiometric study. Bull. Chem. Soc. Jpn. **53**(8), 2221–2227 (1980)
38. Sylva, R.N., Brown, P.L.: The hydrolysis of metal ions. Part 3. Lead(II). J. Chem. Soc., Dalton Trans. **9**(9), 1577–1581 (1980)
39. Cruywagen J.J., van de Water R.F: The hydrolysis of lead(II). A potentiometric and enthalpimetric study. Talanta **40**(7), 1091–1095 (1993)
40. Perera, W.N., Hefter, G., Sipos, P.M.: An investigation of the lead(II) - hydroxide system. Inorg. Chem. **40**(16), 3974–3978 (2001)
41. Pettit, L.D., Powell, K.J.: IUPAC Stability Constants Database (SC-Database, Release 5.8 for Windows). Academic Software and K.J. Powell, Ottley. www.acadsoft.co.uk (2009)
42. Tikhonov, A.S.: Study of complex lead citrate compounds depending on the pH of the aqueous medium. Sb. Trudov Voronezhsk. Gos. Univ. **49**, 23–24 (1958) (in Russian)
43. SigmaPlot 2001 for Windows, Version 7.0 © 1986–2001, SPSS Inc., USA
44. Lur'e Yu, Yu.: Handbook on Analytical Chemistry, p. 448. Khimiya, Moscow (1967) (in Russian)

45. Kitaev, G.A., Bol'shchikova, T.P., Yatlova, L.E.: On the question of solubility of salts of cyanamide with some metals. Zh. Neorg. Khim. **16**(12), 3173–3175 (1971). (in Russian)
46. Sadovnikov, S.I., Gusev, A.I.: Preparation of nanocrystalline lead sulfide powder with controlled particles size. Zh. Obshch. Khim. **84**(2), 177–184 (2014) (in Russian). (Engl. Transl.: Russ. J. Gen. Chem. **84**(2), 173–180 (2014))
47. Sadovnikov, S.I., Gusev, A.I.: Hydrochemical precipitation of nanocrystalline lead sulfide powders. Neorg. Mater. **51**(12), 1313–1318 (2015) (in Russian). (Engl. Transl.: Inorg. Mater. **51**(12), 1219–1224 (2015))
48. Noda, Y., Ohba, S., Sato, S., Saito, Y.: Charge distribution and atomic thermal parameters of lead chalcogenide crystals. Acta Crystallogr. B. **B39**(3), 312–317 (1983)
49. Noda, Y., Masumoto, K., Ohba, S., Saito, Y., Toriumi, K., Iwata, Y., Shibuya, K.: Temperature dependence of atomic thermal parameters of lead chalcogenide, PbS, PbSe, and PbTe. Acta Crystallogr. C. **C43**(8), 1443–1445 (1987)
50. Rempel, A.A., Kozhevnikova, N.S., Leenaers, A.J.G., van den Berghe, S.: Towards particle size regulation of chemically deposited lead sulfide (PbS). J. Cryst. Growth. **280**, 300–308 (2005)
51. Sadovnikov, S.I., Gusev, A.I.: A method of producing nanocrystalline lead sulfide, pp. 1–5. Patent No. 2591160 of Russian Federation (2016)
52. Jiang, Y., Wu, Y., Xie, B., Yuan, S.W., Liu, X.M.: Hydrothermal preparation of uniform cubic-shaped PbS nanocrystals. J. Cryst. Growth. **231**, 248–251 (2001)
53. Yang, Y.J., He, L.Y., Zhang, Q.F.: A cyclic voltametric synthesis of PbS nanoparticles. Electrochem. Commun. **7**(4), 361–364 (2005)
54. Sharon, M., Ramaiaha, K.S., Kumar, M., Neumann-Spallart, M., Levy-Clement, C.: Electrodeposition of lead sulphide in acidic medium. J. Electroanal. Chem. **436**, 49–52 (1997)
55. Yang, Y.J.: A novel electrochemical preparation of PbS nanoparticles. Mater. Sci. Eng. B. **131**(1–3), 200–202 (2006)
56. Pellegri, N., Trbojevich, R., de Sanctis, O.: Fabrication of PbS nanoparticles embedded in silica gel by reverse micelles and sol-gel routes. J. Sol-Gel Sci. Techn. **8**, 1023–1028 (1997)
57. Xu, L., Chen, X., Wang, L., Sui, Z.M., Zhao, J., Zhu, B.: Formation of lead sulfide nanoparticles via Langmuir-Blodgett technique. Colloids and Surface A: Physicochem. Eng. Aspects **257-258**, 457–460 (2005)
58. Yu, Y., Zhang, K., Sun, S.: One-pot aqueous synthesis of near infrared emitting PbS quantum dots. Appl. Surf. Sci. **258**, 7181–7187 (2012)
59. Gerion, D., Pinaud, F., Williams, S.C., Parak, W.J., Zanchet, D., Weiss, S., Alivisatos, A.P.: Synthesis and properties of biocompatible water-soluble silica-coated CdSe/ZnS semiconductor quantum dots. J. Phys. Chem. B. **105**(37), 8861–8871 (2001)
60. Gao, X., Cui, Y., Levenson, R.M., Chung, L.W.K., Nie, S.: In vivo cancer targeting and imaging with semiconductor quantum dots. Nature Biotechnology. **22**(8), 969–976 (2004)
61. Sathyamoorthy, R., Kungumadevi, L.: Facile synthesis of PbS nanorods induced by concentration difference. Advanc. Powd. Techn. **26**(2), 355–361 (2015)
62. Ding, B., Shi, M., Chen, F., Zhou, R., Deng, M., Wang, M., Chen, H.Z.: Shape-controlled synthesis of PbS submicro-/nanocrystals via hydrothermal method. J. Cryst. Growth. **311**(6), 1533–1538 (2009)
63. Emadi, H., Salavati-Niasari, M.: Hydrothermal synthesis and characterization of lead sulfide nanocubes through simple hydrothermal method in the presence of [bis(salicylate)lead(II)] as a new precursor. Superlatt. Microstr. **54**, 118–127 (2013)
64. Ni, Y., Liu, H., Wang, F., Liang, Y., Hong, J., Ma, X., Xu, Z.: Shape controllable preparation of PbS crystals by a simple aqueous phase route. Cryst. Growth Design. **4**(4), 759–764 (2004)
65. Huang, Q., Gao, L.: Simple route for synthesis of PbS dendritic nanostructured materials. Chem. Lett. **33**(10), 1338–1339 (2004)
66. Zhao, P.T., Chen, G., Hu, Y., He, X.L., Wu, K., Cheng, Y., Huang, K.X.J.: Preparation of dentritic PbS nanostructures by ultrasonic method. J. Cryst. Growth. **303**(2), 632–637 (2007)

67. Ma, Y., Qi, L., Ma, J., Cheng, H.: Hierarchical, star-shaped PbS crystals formed by a simple solution route. Cryst. Growth Design. **4**(2), 351–354 (2004)
68. Ding, Y.H., Liu, X.X., Guo, R.: Synthesis of hollow PbS nanospheres in pluronic F127/cyclohexane/H_2O microemulsions. Colloids Surf. A: Physicochem. Eng. Aspects. **296** (1–3), 8–18 (2007)
69. Leontidis, E., Orphanou, M., Kyprianidou-Leondidou, T., Krumeich, F., Caseri, W.: Composite nanotubes formed by self-assembly of PbS nanoparticles. Nano Letters. **3**(4), 569–572 (2003)
70. Li, G., Shi, G., Xu, H., Guang, S., Yin, R., Song, Y.: Nonlinear optical properties of the PbS nanorods synthesized via surfactant-assisted hydrolysis. Mater. Lett. **61**(8–9), 1809–1811 (2007)
71. Wang, W., Li, Q., Li, M., Lin, H., Hong, L.: Growth of PbS microtubes with quadrate cross sections. J. Cryst. Growth. **299**(1), 17–21 (2007)
72. Sun, J.-Q., Shen, X.-P., Guo, L.-J., Chen, K.-M., Liu, Q.: Microwave-assisted synthesis of flower-like PbS crystals. Physica E: Low-Dimens. Systems Nanostructures. **41**(8), 1527–1532 (2009)
73. Jiao, J., Liu, X., Gao, W., Wang, C., Feng, H., Zhao, X., Chen, L.: Synthesis of PbS nanoflowers by biomolecule-assisted method in the presence of supercritical carbon dioxide. Sol. State Sci. **11**(5), 976–981 (2009)
74. Shakouri-Arani, M., Salavati-Niasari, M.: A facile and reliable route to prepare of flower shaped lead sulfide nanostructures from a new sulfur source. J. Industr. Eng. Chem. **20**(5), 3141–3149 (2014)
75. Wu, M., Zhong, H., Jiao, Z., Li, Z., Sun, Y.: Synthesis of PbS nanocrystallites by electron beam irradiation. Colloids Surf. A: Physicochem. Eng. Aspects. **313–314**, 35–39 (2008)
76. Mozafari, M., Moztarzadeh, F., Seifalian, A.M., Tayebi, L.: Self-assembly of PbS hollow sphere quantum dots via gas-bubble technique for early cancer diagnosis. J. Luminesc. **133**, 188–193 (2013)
77. Schiener, A., Wlochowitz, T., Gerth, S., Unruh, T., Rempel, A., Amenitsch, H., Magerl, A.: Nucleation and growth of CdS nanoparticles observed by ultrafast SAXS. MRS Symp. Proc. **1528**, 1–6 (2013)
78. Schiener, A., Magerl, A., Krach, A., Seifert, S., Steinrück, H.-G., Zagorac, J., Zahn, D., Weihrich, R.: In-situ investigation of two-step nucleation and growth of CdS nanoparticles from solution. Nanoscale. **7**(26), 11328–11333 (2015)
79. Gusev, A.I.: Effects of the nanocrystalline state in solids. Uspekhi Fiz. Nauk. **168**(1), 55–83 (1998) (in Russian). (Engl. Transl.: Physics - Uspekhi. **41**(1), 49–76 (1998))
80. Gusev, A.I., Rempel, A.A.: Nanocrystalline Materials, p. 224. Nauka - Fizmatlit, Moscow (2000) (in Russian)
81. Gusev, A.I., Rempel, A.A.: Nanocrysnalline Materials, p. 351. Cambridge Intern. Science Publ, Cambridge (2004)
82. Gusev A.I.: Nanomaterials, Nanostructures, and Nanotechnologies. 3rd edn., p. 416. Nauka – Fizmatlit, Moscow (2009) (in Russian)
83. Okuno, T., Lipovskii, A.A., Ogawa, T., Amagai, I., Masumoto, Y.: Strong confinement of PbSe and PbS quantum dots. J. Luminesc. **87–89**, 491–493 (2000)
84. Wundke, K., Auxier, J., Schülzgen, A., Peyghambarian, N., Borrelli, N.F.: Room-temperature gain at 1.3 mm in PbS-doped glasses. App. Phys. Lett. **75**(20), 3060–3062 (1999)
85. Malyarevich, A.M., Gaponenko, M.S., Savitski, V.G., Yumashev, K.V., Rachkovskaya, G. E., Zakharevich, G.B.: Nonlinear optical properties of PbS quantum dots in boro-silicate glass. J. Non-Crystall. Solids. **353**, 1195–1200 (2007)
86. Kai, Xu, Heo, Jong: Precipitation of PbS quantum dots in glasses by thermal diffusion of Ag + ions from silver pastes. J. Non-Crystall. Solids. **387**, 76–78 (2014)
87. Del Monte, F., Xu, Y., Mackenzie, J.D.: Preparation and characterization of PbS quantum dots doped ormocers. J. Sol-Gel Sci. Techn. **17**, 37–45 (2000)

88. Pinero, M., de la Rosa-Fox, N., Erge-Montilla, R., Esquivias, L.: Small angle neutron scattering study of PbS quantum dots synthetic routes via sol-gel. J. Sol-Gel Sci. Techn. **26**, 527–531 (2003)
89. Krauss, T.D., Wise, F.W., Tanner, D.B.: Observation of coupled vibrational modes of a semiconductor nanocrystal. Phys. Rev. Lett. **76**(8), 1376–1379 (1996)
90. Haché, A.: LeBlanc Serge-Emile, LoCascio M., Martucci A. Optical switchings pectroscopy of PbS quantum dots with dual-wavelength pump-probe. Physica E. **17**, 104–106 (2003)
91. Ullrich, B., Wang, J.S.: Impact of laser excitation variations on the photoluminescence of PbS quantum dots on GaAs. J. Luminesc. **143**, 645–648 (2013)
92. Yu, Y., Zhang, K., Sun, S.: Effect of ligands on the photoluminescence properties of water-soluble PbS quantum dots. J. Molec. Str. **1031**, 194–200 (2013)
93. Pentia, E., Pintilie, L., Matei, I., Botila, T., Pintilie, I.: Combined chemical-physical methods for enhancing IR photoconductive properties of PbS thin films. Infrared Phys. Techn. **44**(3), 207–211 (2003)
94. Hodes, G.: Semiconductor and ceramic nanoparticle films deposited by chemical bath deposition. Phys. Chem. Chem. Phys. **9**(18), 2181–2196 (2007)
95. Sadovnikov, S.I., Gusev, A.I., Rempel, A.A.: New crystalline phase in thin lead sulfide films. Pisma v ZhETF. **89**(5), 279–284 (2009) (in Russian). (Engl. Transl.: JETP Lett. **89**(5), 238–243 (2009))
96. Sadovnikov, S.I., Rempel, A.A.: Crystal structure of nanostructured PbS films at temperatures of 293–423 K. Fiz. tverd. Tela. **51**(11), 2237–2245 (2009) (in Russian). (Engl. Transl.: Phys. Sol. State. **51**(11), 2375–2383 (2009))
97. Sadovnikov, S.I., Kozhevnikova, N.S., Gusev, A.I.: Optical properties of nanostructured lead sulfide films with a D03 cubic structure. Fiz. Tekhn. Poluprovodnikov. **45**(12), 1621–1632 (2011) (in Russian). (Engl. Transl.: Semiconductors. **45**(12), 1559–1570 (2011))
98. Sadovnikov, S.I., Kozhevnikova, N.S., Pushin, V.G., Rempel, A.A.: Microstructure of nanocrystalline PbS powders and films. Neorg. Mater. **48**(1), 26–33 (2012) (in Russian). (Engl. Transl.: Inorg. Mater. **48**(1), 21–27 (2012))
99. Sadovnikov, S.I., Kozhevnikova, N.S.: Microstructure and crystal structure of nanocrystalline powders and films. Fiz. tverd. Tela. **54**(8), 1459–1465 (2012) (in Russian). (Engl. Transl.: Phys. Sol. State. **54**(8), 1554–1561 (2012))
100. Sadovnikov, S.I., Gusev, A.I.: Structure and properties of PbS films. J. Alloys Comp. **573**, 65–75 (2013)
101. Sadovnikov, S.I., Rempel, A.A.: Method of producing thin films of lead sulfide, pp. 1–5. Patent No. 2553858 of Russian Federation (2015)
102. Fainer, N.I., Kosinova, M.L., Rumyantsev, YuM, Salman, E.G., Kuznetsov, F.A.: Growth of PbS and CdS thin films by low-pressure chemical vapour deposition using dithiocarbamates. Thin Solid Films. **280**(1–2), 16–19 (1996)
103. Chamberlin, R.R., Sharman, J.S.: Chemical spray deposition process for inorganic films. J. Electrochem. Soc. **113**(1), 86–89 (1966)
104. Thangaraju, B., Kaliannan, P.: Polycrystalline lead thin chalcogenide thin films grown by spray pyrolysis. Cryst. Res. Technol. **35**(1), 71–75 (2000)
105. Nicolau, Y.F.: Solution deposition of thin solid compound films by a successive ionic-layer adsorption and reaction process. Appl. Surf. Sci. **22**(23), 1061–1074 (1985)
106. Nicolau, Y.F.: Process and apparatus for the deposition on a substrate of a thin film of a compound containing at least one cationic constituent and at least one anionic constituent, pp. 1–3. US Patent No. 4675207 (1987)
107. Kanniainen, T., Lindroos, S., Ihanus, J., Leskela, M.: Growth of strongly orientated lead sulfide thin films by successive ionic layer adsorption and reaction (SILAR) technique. J. Mater. Chem. **6**(2), 161–164 (1996)

108. Puišo, J., Tamuleviius, S., Laukaitis, G., Lindroos, S., Leskelä, M., Snitka, V.: Growth of PbS thin films on silicon substrate by SILAR technique. Thin Solid Films. **403–404**, 457–461 (2002)
109. Puišo, J., Lindroos, S., Tamulevičius, S., Leskelä, M., Snitka, V.: Growth of ultra thin PbS films by SILAR technique. Thin Solid Films. **428**, 223–226 (2003)
110. Preetha, K.C., Murali, K.V., Ragina, A.J., Deepa, K., Remadevi, T.L.: Effect of cationic precursor pH on optical and transport properties of SILAR deposited nano crystalline PbS thin films. Curr. Appl. Phys. **12**(1), 53–59 (2012)
111. Yucel, E., Yucel, Y., Beleli, B.: Process optimization of deposition conditions of PbS thin films grown by a successive ionic layer adsorption and reaction (SILAR) method using response surface methodology. J. Cryst. Growth. **422**, 1–7 (2015)
112. Nair, P.K., Garcia, V.M., Hernandez, A.B., Nair, M.T.S.: Photoaccelerated chemical deposition of PbS thin films: novel applications in decorative coatings and imaging techniques. J. Phys. D: Appl. Phys. **24**(8), 1466–1472 (1991)
113. Zhukovskiy, M.A., Stroyuk, A.L., Shvalagin, V.V., Smirnova, N.P., Lytvyn, O.S., Eremenko, A.M.: Photocatalytic growth of CdS, PbS, and CuxS nanoparticles on the nanocrystalline TiO2 films. J. Photochem. Photobiol. A: Chem. **203**(2–3), 137–144 (2009)
114. Ananikov, V.P., Khemchyan, L.L., Ivanova, Y.V., Bukhtiyarov, V.I., Sorokin, A.M., Prosvirin, I.P., Vatsadze, S.Z., Medved'ko, A.V., Nuriev, V.N., Dilman, A.D., Levin, V.V., Koptyug, I.V., Kovtunov, K.V., Zhivonitko, V.V., Likholobov, V.A., Romanenko, A.V., Simonov, P.A., Nenajdenko, V.G., Shmatova, O.I., Muzalevskiy, V.M., Nechaev, M.S., Asachenko, A.F., Morozov, O.S., Dzhevakov, P.B., Osipov, S.N., Vorobyeva, D.V., Topchiy, M.A., Zotova, M.A., Ponomarenko, S.A., Borshchev, O.V., Luponosov, Y.N., Rempel, A.A., Valeeva, A.A., Stakheev, A.Y., Turova, O.V., Mashkovsky, I.S., Sysolyatin, S.V., Malykhin, V.V., Bukhtiyarova, G.A., Terent'ev, A.O., Krylov, I.B.: Development of new methods in modern selective organic synthesis: preparation of functionalized molecules with atomic precision. Russ. Chem. Rev. **83**(10), 885–985 (2014)
115. Chen, J.-H., Chao, C.-G., Ou, J.-C., Liu, T.-F.: Growth and characteristics of lead sulfide nanocrystals produced by the porous alumina membrane. Surf. Sci. **601**(22), 5142–5147 (2007)
116. Qadri, S.B., Yang, J., Ranta, B.R., Skelton, E.F., Hu, J.Z.: Pressure induced structural transitions in nanometer size particles of PbS. Appl. Phys. Lett. **69**(15), 2205–2207 (1996)
117. Knorr, K., Ehm, L., Hytha, M., Winkler, B., Depmeier, W.: The high-pressure & #x03B1;/β phase transition in lead sulphide (PbS). Eur. Phys. J. B. **31**(3), 297–303 (2003)
118. Zhang, J., Sun, L., Liao, S., Yan, C.: Size control and photoluminescence enhancement of CdS nanoparticles prepared via reverse micelle method. Solid State Commun. **124**(1–2), 45–48 (2002)
119. Metin, H., Esen, R.: Annealing studies on CBD grown CdS thin films. J. Cryst. Growth **258** (1–2), 141–148 (2003)
120. Wu, G.S., Yuan, X.Y., Xie, T., Xu, G.C., Zhang, L.D., Zhuang, Y.L.: A simple synthesis route to CdS nanomaterials with different morphologies by sonochemical reduction. Mat. Lett. **58**(5), 794–797 (2004)
121. Vorokh, A.S., Rempel, A.A.: Atomic structure of cadmium sulfide nanoparticles. Fiz. tverd. Tela. **49**(1), 143–148 (2007) (in Russian). (Engl. Transl.: Phys. Sol. State. **49**(1), 148–153 (2007))
122. Rempel, A.A., Magerl, A.: Non-periodicity in nanoparticles with close-packed structures. Acta Crystallogr. A. **A66**(4), 479–483 (2010)
123. Qadri, S.B., Singh, A., Yousuf, M.: Structural stability of PbS films as a function of temperature. Thin Solid Films. **431–432**, 506–510 (2003)
124. Fernandez-Lima, F.A., Gonzalez-Alfaro, Y., Larramendi, E.M., Fonseca Filho, H.D., Maia da Costa, M.E.H., Freire Jr., F.L., Prioli, R., de Avillez, R.R., da Silveira, E.F., Calzadilla, O., de Melo, O., Pedrero, E., Hernández, E.: Structural characterization of chemically deposited PbS thin films. Mater. Sci. Eng. B. **136**(2–3), 187–192 (2007)

125. Gotoh, Y., Onoda, M., Goto, M., Oosawa, Y.: Preparation and characterization of "PbVS3" a new composite layered compound. Chem. Lett. **18**(7), 1281–1282 (1989)
126. Wiegers, G.A., Meetsma, A., Haange, R.J., van Smaalen, S., de Boer, J.L., Meerschaut, A., Rabu, P., Rouxel, J.: The incommensurate misfit layer structure of (PbS)1.14NbS2 "PbNbS3" and (LaS)1.14NbS2 "LaNbS3": an x-ray diffraction study. Acta Crystallog. **B46** (3), 324–332 (1990)
127. Wullf, J., Meetsma, A., van Smaalen, S., Haange, R.J., de Boer, J.L., Wiegers, G.A.: Structure, electrical transport and magnetic properties of the misfit layer compound (PbS) 1.13TaS2. J. Solid State Chem. **84**(1), 118–129 (1990)
128. Wiegers, G.A.: Misfit layer compounds: Structures and physical properties. Progr. Solid State Chem. **24**(1–2), 1–139 (1996)
129. Sadovnikov, S.I., Rempel, A.A.: Nonstoichiometric distribution of sulfur atoms in lead sulfide structure. Dokl. Akad. Nauk. **428**(1), 48–52 (2009) (in Russian). (Engl. Transl.: Dokl. Phys. Chem. **428**(1), 167–171 (2009)
130. X'Pert Plus Version 1.0. Program for Crystallography and Rietveld analysis Philips Analytical B. V. © Koninklijke Philips Electronics N. V
131. Philips Analytical.: Philips Analytical X'Celerator. J. Appl. Crystallogr. **34**(4), 538 (2001)
132. Morton, R.W., Simon, D.E., Gislason, J.J., Taylor, S.: Managing background profiles using a new X'Celerstor detector. Adv. X-ray Anal. **46**, 80–85 (2003)
133. Rietveld, H.M.: A profile refinement method for nuclear and magnetic structures. J. Appl. Cryst. **2**(2), 65–71 (1969)
134. Sadovnikov, S.I., Rempel, A.A.: Correlation of sulfur atoms in nonmetal planes of lead sulfide films with the D03 structure. Fiz. tverd. Tela. **52**(12), 2299–2306 (2010) (in Russian). (Engl. Transl.: Phys. Sol. State. **52**(12), 2458-2466 (2010))
135. Gusev, A.I., Rempel, A.A., Magerl, A.J.: Disorder and Order in Strongly Nonstoichiometric Compounds. Transition Metal Carbides, Nitrides and Oxides, p. 608. Springer, Berlin (2001)
136. Sadovnikov, S.I, Rempel, A.A.: Simulation of pair and three-particle correlations in a binary solid solution with a hexagonal lattice. Fiz. tverd. Tela. **50**(6), 1085–1089 (2008). (in Russian). (Engl. Transl.: Phys. Sol. State. **50**(6), 1131–1136 (2008))
137. Moss, T.S.: Optical Properties of Semiconductors, p. 279. In: Hogarth, C.A. (ed.) Butterworths Sci. Publ. Ltd., London (1959)
138. Zemmel, J.N., Jensen, J.D., Schoolar, R.B.: Electrical and optical properties of epitaxial films of PbS, PbSe, PbTe and SnTe. Phys. Rev. **140**(1A), 330–342 (1965)
139. Ukhanov Yu, I.: Optical Properties of Semiconductors, p. 366. Nauka, Moscow (1977) (in Russian)
140. Gusev, A.I.: Nanocrystalline Materials: Production and Properties, p. 200. Ural Division of the RAS, Ekaterinburg (1998) (in Russian)
141. Sashchiuk, A., Lifshitz, E., Reisfeld, R., Saraidarov, T., Zelner, M., Willenz, A.J.: Optical and conductivity properties of PbS nanocrystals in amorphous zirconia sol-gel films. Sol-Gel Sci. Techn. **24**(1), 31–38 (2002)
142. Yu, B., Yin, G., Zhu, G., Gan, F.: Optical nonlinear properties of PbS nanoparticles studied by the Z-scan technique. Opt. Mater. **11**(1), 17–21 (1998)
143. Jana, S., Thapa, R., Maity, R., Chattopadhyay, K.K.: Optical and dielectric properties of PVA capped nanocrystalline PbS thin films synthesized by chemical bath deposition. Phys. E. **40**(10), 3121–3126 (2008)
144. Brus, L.E.: Electron-electron and electron-hole interactions in small semiconductor crystallites: The size dependence of the lowest excited electronic state. J. Chem. Phys. **80** (9), 4403–4409 (1984)
145. Wang, Y., Herron, N.: Nanometer-sized semiconductor clusters: materials synthesis, quantum size effects, and photophysical properties. J. Chem. **95**(2), 525–532 (1991)
146. Najdovski, M., Minceva-Sukarova, B., Drake, A., Grozdanov, I., Chunnilall, C.J.: Optical properties of thin solid films of lead sulfide. J. Mol. Struct. **349**(1), 85–88 (1995)

147. Parra, R.S., George, P.J., Sánchez, G.G., Jiménez González, A.E., Baños, L., Nair, P.K.: Optical and electrical properties of PbS+ In thin films subjected to thermal processing. J. Phys. Chem. Solids. **61**(5), 659–668 (2000)
148. Valenzuel-Jaureguia, J.J., Ramirez-Bon, R., Mendoza-Galvan, A., Sotelo-Lerma, M.: Optical properties of PbS thin films chemically deposited at different temperatures. Thin Solid Films **441**, 104–110 (2003)
149. Peterson, J.J., Krauss, T.D.: Fluorescence spectroscopy of single lead sulfide quantum dots. Nano Lett. **6**(3), 510–514 (2006)
150. Zhao, Y., Zou, J., Shi, W.: In situ synthesis and characterization of lead sulfide nanocrystallites in the modified hyperbranched polyester by gamma-ray irradiation. Mater. Sci. Eng. B. **121**(1–2), 20–24 (2005)
151. Sadovnikov, S.I., Kozhevnikova, N.S., Rempel, A.A.: The structure and optical properties of nanocrytalline lead sulfide films. Fiz. Tekhn. Poluprovodnikov. **44**(10), 1394–1400 (2010) (in Russian). (Engl. Transl.: Semiconductors. **44**(10), 1349–1356 (2010))
152. Tauc, J. (ed.): Amorphous and Liquid Semiconductors. Plenum, New York (1974)
153. Klingshirn, C.F.: Semiconductor Optics, p. 797. Springer, New York (2005)
154. Pankove, J.I.: Optical processes in semiconductors, 2nd edn, p. 428. Dover Publ, New York (1975)
155. Elliot, R.J.: Intensity of optical absorption by excitons. Phys. Rev. **108**(6), 1384–1389 (1957)
156. Mittleman, D.M., Schoenlein, R.W., Shiang, J.J., Colvin, V.L., Alivisatos, A.P., Shank, C. V.: Quantum size dependence of femtosecond electronic dephasing and vibrational dynamics in CdSe nanocrystals. Phys. Rev. B. **49**(20), 14435–14447 (1994)
157. Mozer, F., Urbach, F.: Optical absorption of pure silver halides. Phys. Rev. **102**(6), 1519–1523 (1956)
158. Kumara, D., Agarwal, G., Tripathi, B., Vyas, D., Kulshrestha, V.: Characterization of PbS nanoparticles synthesized by chemical bath deposition. J. Alloys Comp. **484**, 463–466 (2009)
159. Wang, Y., Suna, A., Mahier, W., Kasowski, R.: PbS in polymers. From molecules to bulk solids. J. Chem. Phys. **87**(12), 7315–7322 (1987)
160. Hellwege, K.-H., Madelung, O. (eds): Landolt-Börnstein: Zahlenwerte und Funktionen aus Naturwissenschaften und Technik – Neue Serie/Grouppe III: Kristall- und Festkorperphysik, Band 17f, pp. 155–162. Springer, Berlin (1983)
161. Mamiyev, Z.Q.: Balayeva N.O. Preparation and optical studies of PbS nanoparticles. Optic. Mat. **46**, 522–525 (2015)
162. Lifshitz, E., Sirota, M., Porteanu, H.: Continuous and time-resolved photoluminescence study of lead sulfide nanocrystals, ebmedded in polymer film. J. Cryst. Growth. **196**, 126–134 (1999)
163. Navaneethan, M., Sabarinathan, M., Harish, S., Archana, J., Nisha, K.D., Hayakawa, Y., Ponnusamy, S., Muthamizhchelvan, C.: Chemical synthesis and functional properties of multi-ligands passivated lead sulfide nanoparticles. Mat. Lett. **158**, 75–79 (2015)
164. Sharma, S.S:. Thermal expansion of crystals. Part VIII. Galena and pyrite. Proc. Indian Acad. Sci. Sect.A. **A34**(2), 72–76 (1951)
165. Novikova, S.I., Abrikosov, N.Kh.: Investrigation of thermal expansion of the lead chalcogenides. Fiz. Tved. Tela. **5**(7), 1913–1916 (1963) (in Russian) (Engl. Transl.: Sov. Phys. Solid State. **5**(7), 1558–1559 (1963)
166. Zhang, Yi, Ke, X., Chen, C., Yang, J., Kent, P.R.C.: Thermodynamic properties of PbTe, PbSe, and PbS: First-principles study. Phys. Rev. B. **B80**(2), 12 (2009) Paper 024304
167. Sadovnikov, S.I., Kozhevnikova, N.S., Rempel, A.A., Magerl, A.: Thermal expansion of a lead sulfide nanofilm. Thin Solid Films. **548**, 230–234 (2013)
168. Sadovnikov, S.I., Gusev, A.I.: Effect of particle size on the thermal expansion of nanostructured lead sulfide films. J. Alloys Comp. **610**, 196–202 (2014)

169. Sadovnikov, S.I., Gusev, A.I.: Thermal expansion of nanostructured PbS films and anharmonicity of atomic vibrations. Fiz. Tverd. Tela. **56**(11), 2274–2278 (2014) (in Russian). (Engl. Transl.: Phys. Sol. State. **56**(11), 2353–2358 (2014)
170. Ashcroft, N.W., Mermin, N.D.: Solid State Physics, pp. 492–494. Cornell University, New York (1976)
171. Petrov Yu, I. Physics of Small Particles, 360 pp. Nauka, Moscow (1982) (in Russian)
172. Bolt, R.H.: Frequency distribution of eigentones in a three-dimensional continuum. J. Acoust. Soc. Am. **10**(3), 228–234 (1939)
173. Maa, D.-Y.: Distribution of eigentones in a rectangular chamber at low frequency range. J. Acoust. Soc. Am. **10**(3), 235–238 (1939)
174. Montrol, E.W.: Size effect in low temperature heat capacities. J. Chem. Phys. **18**(2), 183–185 (1950)
175. Chudinov, A.A.: Dependence of velocity of ultrasound in monocrystals PbS on temperature in the range of 80–640 K. Fiz. tverd. Tela. **5**(5), 1458–1460 (1963). (in Russian). (Engl. Transl.: Sov. Phys. Sol. State. **5**(5), 1061–1062 (1963))
176. Padaki, V., Lakshimikumar, S., Subramanyam, S., Gopal, E:. Elastic constants of galena down to liquid helium temperatures. Pramana (J. Phys.) **17**(1), 25–32 (1981)
177. Li, W., Chen, J.-F., Wang, T.: Electronic and elastic properties of PbS under pressure. Physica B. **405**, 1279–1282 (2010)
178. Bhardwaj, P:. Investigation of structural phase transition of PbS. ISRN Cond. Matter Physics. **2012** (2012). Article ID 596397
179. Pei, Y.-L., Liu, Y.: Electrical and thermal transport properties of Pb-based chalcogenides: PbTe, PbSe, and PbS. J. Alloys Comp. **514**, 40–44 (2012)
180. Peresada, G.I., Ponyatovskii, E.G., Sokolovskaya, Zh.D.: Pressure dependence of the elastic constants of PbS. Phys. Status Sol. **35**(2), K177–K180 (1976)
181. Choudhury, N., Sarma, B.K.: Structural characterization of lead sulfide thin films by means of X-ray line profile analysis. Bull. Mater. Sci. **32**(1), 43–47 (2009)
182. Sadovnikov, S.I., Kozhevnikova, N.S., Rempel, A.A.: Thermal stability of lead sulfide nanocrystalline films. Fiz. Khim. Stekla. **35**(1), 74–82 (in Russian). (Engl. Transl.: Glass Phys. Chem. **35**(1), 60–66 (2009))
183. Sadovnikov, S.I., Kozhevnikova, N.S., Rempel, A.A:. Oxidation of nanocrystalline lead sulfide in air. Zh. neorg. Khimii. 56(12), 1951–1957 (2011) (in Russian). (Engl. Transl.: Russ. J. Inorg. Chem. **56**(12), 1864–1869 (2011))
184. Sadovnikov, S.I., Kozhevnikova, N.S., Rempel, A.A.: Stability and recrystallization of PbS nanoparticles. Neorg. Mater. **47**(8), 929–935 (2011) (in Russian). (Engl. Transl.: Inorg. Mater. **47**(8), 837–843 (2011))
185. Gertsman, V.Y., Birringer, R., Valiev, R.Z., Gleiter, H.: On the structure and strength of ultrafine-grained copper produced by severe plastic deformation. Scr. Met. Mat. **30**(2), 229–234 (1994)
186. Mikhlin Yu, L., Romanchenko, A.S., Shagaev, A.A.: Scanning probe microscopy studies of PbS surfaces oxidized in air and etched in aqueous acid solutions. Appl. Surf. Sci. **252**(16), 5645–5648 (2006)
187. Ihly, R., Tolentino, J., Liu, Y., Gibbs, M., Law, M.: The photothermal stability of PbS quantum dot solids. ACS Nano. **5**(10), 8175–8186 (2011)
188. García, V.M., Nair, M.T.S., Nair, P.K.: Optical properties of PbS·Cu_xS and Bi_2S_3·Cu*x*S thib films with reference to solar control and solar absorber applications. Sol. Energy Mater. **23** (1), 47–59 (1991)
189. Nair, P.K., Gomezdaza, O., Nair, M.T.S.: Metal sulphide thin film photography with lead sulphide thin films. Adv. Mater. Opt. Electron. **1**(3), 139–145 (1992)
190. Loiko, P.A., Rachkovskaya, G.E., Zakharevich, G.B., Gurin, V.S., Gaponenko, M.S., Yumashev, K.V.: Optical properties of novel PbS and PbSe quantum-dot-doped alumino-alkali-silicate glasses. J. Non-Cryst. Solids **358**(15), 1840–1845 (2012)

191. Carrillo-Castillo, A., Salas-Villasenor, A., Mejia, I., Aguirre-Tostado, S., Gnade, B.E., Quevedo-Lopez, M.A.: P-type thin films transistors with solution-deposited lead sulfide films as semiconductor. Thin Solid Films. **520**, 3107–3110 (2012)
192. He, J., Luo, M., Hu, L., Zhou, Y., Jiang, S., Song, H., Ye, R., Chen, J., Gao, L., Tang, J.: Flexible lead sulfide colloidal quantum dot photodetector using pencil graphite electrodes on paper substrates. J. Alloys Comp. **596**, 73–78 (2014)
193. Slonopas, A., Alijabbari, N., Saltonstall, C., Globus, T., Norris, P.: Chemically deposited nanocrystalline lead sulfide thin films with tunable properties for use in photovoltaics. Electrochim. Acta. **151**, 140–149 (2015)
194. Sabet, M., Salavati-Niasari, M.: Deposition of lead sulfide nanostructure films on TiO2 surface via different chemical methods due to improving dye-sensitized solar cells efficiency. Electrocim. Acta. **169**, 168–179 (2015)
195. Jang, J., Song, J.H., Choi, Y., Baik, S.J., Jeong, S.: Photovoltaic light absorber with spatial energy band gradient using PbS quantum dot layers. Solar Energy Mater. Solar Cells. **141**, 270–274 (2015)
196. Zimin, S.P., Gorlachev, E.S.: Nanostructured Lead Chalcogenides, 230 pp. Yaroslavl's State University, Yaroslavl (2011) (in Russian)
197. Markov, V.F., Maskaeva, L.N.: Lead sulfide semiconductor sensing element for nitrogen oxide gas analyzers. Zh. Anal. Khimii. **56**(8), 846–850 (2001) (in Russian). (Engl. Transl.: J. Anal. Chem. **56**(8), 754–757 (2001))
198. Fu, T.: Research on gas-sensing properties of lead sulfide-based sensor for detection of NO2 and NH3 at room temperature. Sens. Actuators B. **140**(1), 116–121 (2009)
199. Bandyopadhyay, S.: Performance of nanocrystalline PbS gas sensor with improved cross-sensitivity. Particul. Sci. Technol. **30**(1), 43–54 (2012)
200. Karami, H., Ghasemi, M., Matini, S.: Synthesis, characterization and application of lead sulfide nanostructures as ammonia gas sensing agent. Int. J. Electrochem. Sci. **8**(10), 11661–11679 (2013)
201. Kaci, S., Keffous, A., Hakoum, S., Mansri, A.: Hydrogen sensitivity of the sensors based on nanostructured lead sulfide thin films deposited on a-SiC: H and p-Si(100) substrates. Vacuum **116**, 27–30 (2015)
202. Kullick, T., Quack, R., Röhrkasten, C., Pekeler, T., Scheper, T., Schügerl, K.: PbS-field-effect-transistor for heavy-metal concentration monotoring. Chem. Eng. Technol. **18**(4), 225–228 (1995)
203. Markov, V.F., Maskaeva, L.N., Zurabin, I.V., Zamaraeva, N.V.: Application of thin films of lead sulfide doped with halogens, to monitor the content of lead ions in aqueous media. Water: Chem. Ecolog. **6**, 80–85 (2012) (in Russian)
204. Xie, Y., Qiao, Z., Chen, M., Liu, X., Qian, Y.: Irradiation route to semiconductor/polymer nanocable fabrication. Adv. Mater. **11**(18), 1512–1515 (1999)
205. Garcia, O.P., de Albuquerque, M.C.C., da Silva Aquino, K.A., de Araujo, P.L.B., de Araujo, E.S.: Use of lead(II) sulfide nanoparticles as stabilizer for PMMA exposed to gamma irradiation. Mater. Res. **18**(2), 365–372 (2015)
206. Kirpichnikov, M.P., Kochetkov, S.N.: Chemistry and biomedicine: diversity and unity of goals. Russ. Chem. Rev. **84**(1), 1 (2015)
207. Povolotskaya, A.V., Povolotskiy, A.V., Manshina, A.A.: Hybrid nanostructures: synthesis, morphology and functional properties. Russ. Chem. Rev. **84**(6), 579–600 (2015)
208. Andreakou, P., Brossard, M., Bernechea, M., Konstantatos, G., Lagoudakis, P. Resonance energy transfer from PbS colloidal quantum dots to bulk silicon: the road to hybrid photovoltaics. In: Proceedings of SPIE "Physics, Simulation, and Photonic Engineering of Photovoltaic Devices", vol. 8256, pp. 82561L-1–82561L-6 (2012)
209. Narayanan, S., Sathy, B.N., Mony, U., Koyakutty, M., Nair, S.V., Menon, D.: Biocompatible magnetite/gold nanohybrid contrast agents via green chemistry for MRI and CT bioimaging. ACS Appl. Mater. Interfaces. **4**(1), 251–260 (2012)
210. Genuino, H., Huang, H., Njagi, E., Stafford, L., Suib, S.L.: A review of green synthesis of nanophase inorganic materials for green chemistry applications. In: Perosa, A., Selvav, M.

(eds.) Handbook of Green Chemistry, vol. 8, pp. 217–244. Green Nanoscience. Wiley-VCH, Weinheim (2012)
211. Shen, A., Chen, L., Xie, W., Hu, J., Zeng, A., Richards, R., Hu, J.: Triplex Au–Ag–C core–shell nanoparticles as a novel Raman label. Adv. Funct. Mater. **20**(6), 969–975 (2010)
212. Lu, Y.J., Wei, K.C., Ma, C.C., Yang, S.Y., Chen, J.P.: Dual targeted delivery of doxorubicin to cancer cells using folate-conjugated magnetic multi-walled carbon nanotubes. Colloids Surf. B. **89**, 1–9 (2012)
213. Argyo, C., Weiss, V., Braeuchle, C., Bein, T. Multifunctional mesoporous silica nanoparticles as a universal platform for drug delivery. Chem. Mater. **26**(1), 435–451 (2014)
214. Fernandes, A.M., Abdalhai, M.H., Ji, J., Xi, B.-W., Xie, J., Sun, J., Noeline, R., Lee, B.H., Sun, X.: Development of highly sensitive electrochemical genosensor based on multiwalled carbon nanotubes-chitosan-bismuth and lead sulfide nanoparticles for the detection of pathogenic Aeromonas. Biosens. Bioelectr. **63**, 399–406 (2015)
215. Li, Q., Hu, X., Bai, Y., Alattar, M., Ma, D., Cao, Y., Hao, Y., Wang, L., Jiang, C.: The oxidative damage and inflammatory response induced by lead sulfide nanoparticles in rat lung. Food Chem. Toxicol. **60**, 213–217 (2013)
216. Cao, Y., Liu, H., Li, Q., Wang, Q., Zhang, W., Chen, Y., Wang, D., Cai, Y.: Effect of lead sulfide nanoparticles exposure on calcium homeostasis in rat hippocampus neurons. J. Inorg. Biochem. **126**, 70–75 (2013)
217. Huang, N., Zhao, Q., Xiao, J., Qi, L.: Controllable self-assembly of PbS nanostars into ordered structures: Close-packed arrays and patterned arrays. ACS Nano. **4**(8), 4707–4716 (2010)
218. Sadovnikov, S.I., Gusev, A.I., Rempel, A.A.: Nonstoichiometry of nanocrystalline monoclinic silver sulfide. Phys. Chem. Chem. Phys. **17**(19), 12466–12471 (2015)
219. Gusev, A.I., Sadovnikov, S.I., Chukin, A.V., Rempel, A.A.: Thermal expansion of nanocrystalline and coarse-crystalline silver sulfide Ag_2S. Fiz. Tverd. Tela. **58**(2), 246–251 (2016) (in Russian). (Engl. Transl.: Phys. Solid State. **58**(2), 251–257 (2016))
220. Sadovnikov, S.I. Gusev, A.I., Chukin, A.V., Rempel, A.A.: High-temperature X-ray diffraction and thermal expansion of nanocrystalline and coarse-crystalline acanthite α-Ag_2S and argentite β-Ag_2S. Phys. Chem. Chem. Phys. **18**(6), 4617–4626 (2016)
221. Chen, X.F., He, G., Liu, M., Zhang, J.W., Deng, B., Wang, P.H., Zhang, M., Lv, J.G., Sun, Z.Q.: Modulation of optical and electrical properties of sputtering-derived amorphous InGaZnO thin films by oxygen partial pressure. J. Alloys Comp. **615**, 636–642 (2014)

http://www.springer.com/978-3-319-56386-2

Nanostructured Lead, Cadmium, and Silver Sulfides
Structure, Nonstoichiometry and Properties
SADOVNIKOV, S.; Rempel, A.A.; Gusev, A.I.
2018, XIV, 317 p. 167 illus., 97 illus. in color., Hardcover
ISBN: 978-3-319-56386-2